THE UNIVERSITY
OF BIRMINGHAM

SYNTHESIS, DESIGN AND FABRICATION OF MICROWAVE FILTERS AND MULTIPLEXERS

By

ABOLFAZL MOSTAANI

A thesis submitted to the University of Birmingham for the degree of DOCTOR OF PHILOSOPHY

School of Electronic, Electrical and Systems Engineering

College of Engineering and Physical Sciences

The University of Birmingham

July 2024

ABSTRACT

This thesis presents new synthesis processes for filters and multiplexers. It also demonstrates novel implementation of microwave filters using Selective Laser Melting (SLM) and Micro-Laser-Sintering (MLS) based 3-D printing technologies. The thesis contains six projects.

The first project proposes a synthesis and design approach for filters with multiple transmission zeros generated using dual/multiple dangling nodes. It starts with the synthesis of the general characteristic polynomials. An analytical method is proposed to derive the coupling matrix from the polynomials. Two third-order-two-zero bandpass filters (BPFs) are used to demonstrate the synthesis and design procedure. Two third-order-four-zero BPFs are then designed and prototyped using two pairs of mixed E/H-plane dual dangling nodes. The fabrication is enabled by 3D printing technology. Excellent agreement between the measurement and the design substantially verifies the synthesis and design approach and demonstrates the capability of the additive manufacture technology.

The second project presents an iterative method to achieve a strong initial coupling matrix for triggering the subsequent matrix optimization of diplexers/multiplexers with all-resonator topologies. The method is based on the synthesis of a single channel filter in consideration of the estimated loading effect of other channels. The synthesis starts with the characteristic polynomials of each channel filter, obtaining corresponding input admittance, and extracting the equivalent circuit model. Seven examples are used to demonstrate the synthesis process and validate the proposed technique. For most topologies, the iterative method converges after less than 20 iterations. The proposed method provides good initial values of the coupling matrix which can substantially reduce the optimization time to seconds, even for complicated topologies.

The third project demonstrates a narrowband third-order filter at 9 GHz with two transmission zeros generated using the non-resonating node (NRN) method. The filter is fabricated out of aluminium-copper alloy (A20X) using selective laser melting (SLM) technology. Without tuning, the measurements show promising results, but with a resonator detuning. Micro X-Ray CT imaging is performed to investigate the imperfection in the

manufacture. Dimension measurement of the structure show the level of dimension offset and some evidence of excessive shrinkage from the small iris structures.

The fourth project presents a fifth-order BPF for communication satellite feed systems, fabricated using 3D-printing with Titanium alloy Ti-6Al-4V or Ti64. Taking advantage of the alloy's high strength-to-weight ratio, the filter is printed with a wall thickness of only 1 mm and a weight of 40 g. Ti64 also has a much lower coefficient of thermal expansion (CTE) than aluminium. The filter was designed with modified rectangular cavity resonators with rounded corners, enabling monolithic printing of the structure in a lying-down position without any internal supports. The coupling irises are moved to one side of the filter to facilitate polishing and silver coating. The measured response of the as-printed filter showed a minimum insertion loss of 2.7 dB and a frequency shift of about 140 MHz. After silver plating, the insertion loss was significantly reduced to a minimum of 0.55 dB. The challenge with plating on the Ti64 filter is discussed.

The fifth project presents an irregular-hexagonal resonator geometry for additively manufactured microwave filters. This geometry allows closely packed resonators to form very compact filters of various topologies fulfilling transfer functions with transmission zeros. It also minimizes the overhangs and allows vertical printing along the direction of the input/output ports, without any internal support structure and with a much-reduced profile. The characteristics of the resonator and the trade-off between compactness and quality factor is analysed. Three BPFs are demonstrated. Two of them are designed with NRN topologies with fractional bandwidths of 5% and 1%, respectively, using the step-tuning technique. All three filters are fabricated using SLM technique. The performance of the fabricated filters is compared with the EM simulation. Very good agreement is achieved for all three filters. The effectiveness of tuning is also demonstrated. The resonator structure offers high printability and high level of modularity and flexibility in the design.

Finally, in the sixth project, an E-band bandpass (81 – 86 GHz) filter has been demonstrated to show the effectiveness of surface treatments and a new electrochemical polishing technique, in particular, on the metal 3D-printed millimeter-wave waveguide device. The third-order filter is designed using a modified hexagonal resonator, a compact and self-supportive structure, and two samples have been printed monolithically using a high-precision micro-laser-sintering (MLS) technology out of stainless-steel. The effects of polishing and gold coating have been

investigated. The coating improves the insertion loss by ~1 dB whereas the polishing step further reduces the loss by ~0.3 dB. This results in a very low insertion loss of only 0.14 dB for one of the two samples. This correlates with the 50% reduction in the surface roughness after polishing. The demonstrated end-to-end manufacture and surface treatment process shows great promise in addressing the surface quality issues with metal 3D printing for millimeter-wave devices.

ACKNOWLEDGEMENTS

I would like to start by thanking my supervisors Prof. Yi Wang and Prof. Michael J. Lancaster, for their continuous support and guidance during my Ph.D. study in the Emerging Device Technology (EDT) Research Group at the University of Birmingham. It is an honour to finish my Ph.D. under their supervision. I learnt a great deal from you.

My appreciations go to all my colleagues in the Emerging Device Technology Research Group at the University of Birmingham for their support over these four years. In particular, I would like to thank Dr. Talal Skaik and Lu Qian. Thank you both for your assistance on reviewing papers and helping measure devices during my Ph.D. study. I would also like to thank Dr Frederick Huang for sharing his constructive advice and comments on one of my projects.

I appreciate the support from Dr. Abd El-Moez A. Mohamed, Prof. Moataz M. Attallah and Dr. Rafael Martinez. Thank you all for your constructive contribution to most of my works and fabricating my designs within my Ph.D. study.

My appreciation to Paul F. Wilson and Prof. Mark A. Williams for their support for performing the X-Ray imaging of one of my designs, and a special thanks to Prof. Peter Huggard and Dr. Peter Hunyor for performing the gold plating, and Dr. Xiaobang Shang for helping with measurements. I would also like to thank Dr. Paul Booth, and Dr. Cesar Miquel-Espana for sharing their technical advice and comments on one of my works.

Last but not least, a huge thank you must go to my family, especially my mother and my sister, Elaheh, and the love of my life, my wife, and my best mate George for their valuable support and encouragement.

LIST OF PUBLICATIONS

Published and accepted

1. **A. Mostaani**, T. Skaik, Y. Wang, "Synthesis of All-Resonator Multiplexers," *2024 IEEE MTT-S International Microwave Filter Workshop (IMFW)*, California, USA, Feb 2024.

2. **A. Mostaani**, Y. Wang, L. Qian, A. E. -M. A. Mohamed, M. M. Attallah and T. Skaik, "Compact Self-Supportive Filters Suitable for Additive Manufacturing," *IEEE Transactions on Components, Packaging and Manufacturing Technology*, vol. 13, no. 12, pp. 1966-1972, Dec. 2023.

3. **A. Mostaani**, T. Skaik, A. E. -M. A. Mohamed, M. M. Attallah, P. Booth, C. M. -Espana and Y. Wang, "A 3D-Printed Monolithic Inline Filter Fabricated With Titanium Alloy," *2023 SBMO/IEEE MTT-S International Microwave and Optoelectronics Conference (IMOC)*, Castelldefels, Spain, 2023, pp. 58-60.

4. **A. Mostaani**, L. Qian, R. Martinez, P. F. Wilson, M. M. Attallah, Y. Wang, M. A. Williams, "Investigation of a 3D-Printed Narrowband Filter with Non-Resonating Nodes," *2021 IEEE MTT-S International Microwave Filter Workshop (IMFW)*, Perugia, Italy, 2021, pp. 316-318.

Submitted under review or revision

1. **A. Mostaani**, Y. Wang, F. Huang, L. Qian, A. E. -M. A. Mohamed, M. M. Attallah, "Synthesis, Design, and Fabrication of Filters with Dual/Multiple Dangling Nodes," *IEEE Journal of Microwave* (under review)

2. **A. Mostaani**, Y. Wang, T. Skaik, "Synthesis of All-Resonator Diplexers and Multiplexers," *IEEE Journal of Microwave* (extended full paper based on the IMFW 2024 conference paper)

3. **A. Mostaani**, T. Skaik, L. Qian, P. Huggard, P. Hunyor, X. Shang, Y. Wang, "A Monolithic Metal 3D-Printed E-band Cavity Filter: Manufacture and Surface Treatment," *IEEE Wireless Communications Letters* (under review)

TABLE OF CONTENTS

CHAPTER 1

INTRODUCTION

1.1 Thesis motivation

Microwave filters and multiplexers are widely used in telecommunication systems. They provide frequency selectivity by selecting or rejecting one or more parts of the frequency spectrum. They are also used as building blocks for multi-channel communication and sensing systems to combine or separate multiple frequency bands. One of the key industry areas that deploy such components is the satellite communication (Satcom). In recent years, the satellite industry has enjoyed rapid growth and demands more advanced microwave components. As the usual Satcom frequency channels get crowded, the need for high performance filters and multiplexers with high selectivity increases rapidly. This challenge requires the adoption of novel technologies in the synthesis and design process of such components. The research on synthesis methods of microwave filters and multiplexers has a long history. Some of the early fundamental works on the synthesis methods are presented in [1]-[6]. At Emerging Device Technologies (EDT) Lab at University of Birmingham, the research on advanced synthesis and design methods of filters and multiplexers began two decades ago. One of the resource books for synthesis and design of microwave components is co-authored by the founder of the EDT lab, Prof. Michael J. Lancaster [7]. Other popular works on the filters and multiplexers synthesis methods include those from [8]-[10].

Transmission Zeros (TZs) are often used to improve the selectivity of filters and multiplexers. In case of cavity-based filters, to the best knowledge of the author, all the direct synthesis methods in the literature limit the maximum number of TZs to the filter order. In case of multiplexers, there is no synthesis method in the literature for the all-resonator multiplexers, where TZs can be generated due to their topology without the need for adding specific TZ-generating elements, such as dangling Non-Resonating Nodes (NRNs) and cross-couplings. The available synthesis methods for such multiplexers are based on optimisation, which are very time and memory consuming. This thesis presents two synthesis methods for filters and multiplexers. The new filter synthesis method allows the treatment of more transmission zeros than the in-band poles of the filter. The multiplexer synthesis method reduces the synthesis time for the coupling matrix of all-resonator multiplexer types to seconds.

For Satcom applications, considering the launch cost, engineers are intensely interested in light weight and compact components, which highlights the need for advanced manufacturing and material engineering techniques. The emerge of additive manufacturing or 3-D printing

technologies was revolutionary for the microwave engineering industry, particularly to address the needs of Satcom [11], [12]. Examples of some of these components are reported in [11]-[17]. Using 3-D printing technology for fabrication of passive microwave components has been investigated at the University of Birmingham over last few years. Many microwave filters operating over a frequency range from 0.5 GHz to 300 GHz are demonstrated [18]-[22]. Figure 1.1 shows some of these devices. Figure 1.1(a) is a 3-D printed narrowband bandpass filter based on spherical dual-mode resonators operating at 11.5 GHz. The filter is fabricated using Selective Laser Melting (SLM) technology with Invar alloys of low thermal expansion coefficient [19]. Figure 1.1(b) shows a monolithic 3D printed twisted waveguide bandpass filter working at 60 GHz using Micro Laser Sintering (MLS) – a high-precision metal 3D printing method [21]. Figure 1.1(c) presents a D-band (110-170 GHz) diplexer fabricated using MLS technology using stainless steel [20].

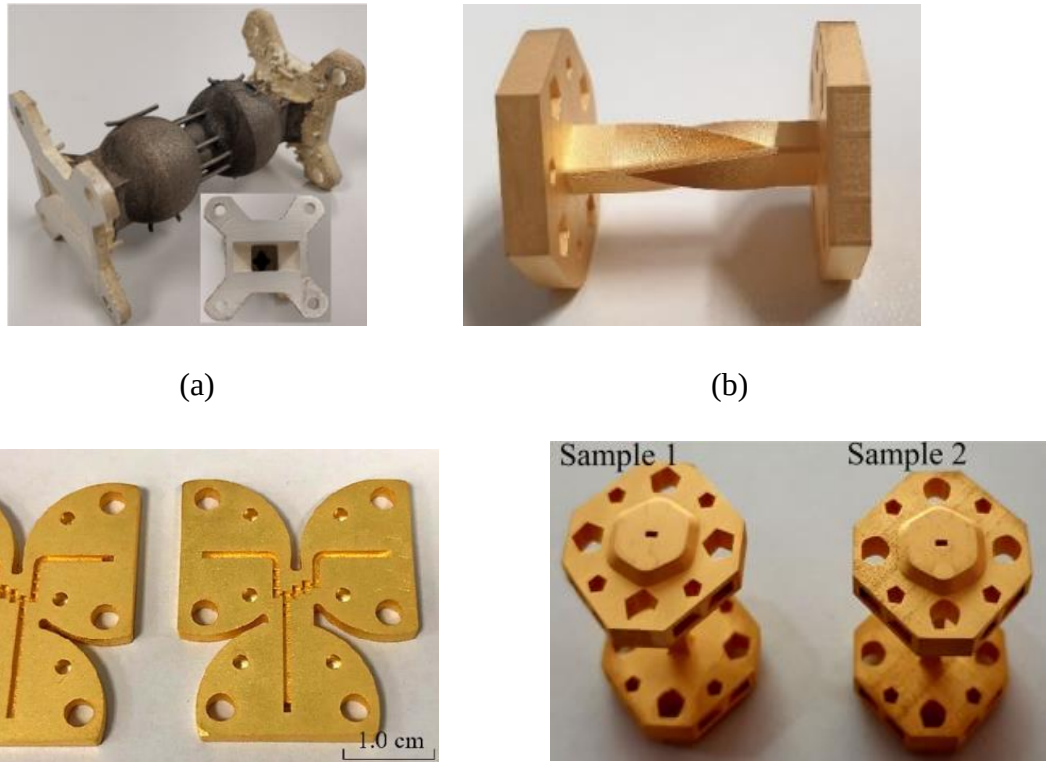

(a) (b)

(c) (d)

Figure 1.1 Photographs of some 3-D printed microwave filters designed at the University of Birmingham. (a) A narrowband bandpass filter based on spherical resonator in Invar [19]. (b) A monolithic 3D printed twisted waveguide bandpass filter [21]. (c) A D-band (110-170 GHz) diplexer [20]. (d) A 180-GHz bandpass filters [18].

Figure 1.1(d) shows two 180 GHz bandpass filters fabricated using MLS technology [18]. More detailed review of the relevant works will be provided in the later chapters. The work in this thesis will demonstrate the design and implementation of compact filter structures enabled by additive manufacturing. The work will also investigate the use of different alloys for fabricating the microwave filters. Most of the filters designed in this work are within the X-band frequency range, whereas one filter operates at E-band.

1.2 Main contribution and novelty claim

The novelty and main contributions in the field of synthesis, design and fabrication of microwave filters are summarised as follows.

- A synthesis and design approach for filters with dual/multiple dangling nodes is proposed. The dual/multiple dangling nodes generate more transmission zeros than the order of the filter.
- A mixed E/H-plane structure is demonstrated that improves the out-of-band rejection of filters with dual-dangling nodes.
- A method for synthesis of all-resonator multiplexers is proposed to reduce the coupling matrix optimisation time to seconds.
- Two modified-resonator geometries are proposed, leveraging the free-forming capability of 3D printing techniques, to compactify the filter structure.
- The capability of additive manufacturing is demonstrated by fabricating six bandpass filters with complex structures impossible or hard to be fabricated using conventional machining.
- The use of different materials, i.e., titanium alloy, stainless steel, and aluminium alloy, in 3D printing process of filters is investigated.
- The effect of gold/silver coating and polishing on the filter's performance is investigated in the SLM and MLS fabrication processes.
- A new polishing technique is tested on an E-band filter. The polishing has improved the insertion loss to a record low level.

1.3 Thesis overview

The thesis will be presenter as a series of published and publishable papers following the University's Alternative Format Thesis guidelines. It is formed of nine chapters covering six projects. A literature review will be provided for each of the project from Chapter 3 to 8 all presented in IEEE paper format. To suit the paper-based thesis format, each chapter contains its own references. Chapter 1 and 2 provides an overview and the background of the thesis whereas Chapter 9 is the Conclusion. They are organised as follows.

• Chapter 1 presents the motivation of the work presented in this thesis. This chapter also provides an overview of the structure of this thesis.

• Chapter 2 provides the theoretical background in terms of fundamental synthesis methods of filter networks, which will be used in this thesis. This chapter begins by describing the concepts of the microwave filter and filter transfer functions. It discusses the coupling matrix synthesis of filter networks for both $N \times N$ and N+2 coupling matrices, as well as the technique for the coupling matrix rotation for achieving different filter topologies. This chapter demonstrates the synthesis method of microwave filters using the equivalent lump circuit model. The method is used to synthesis the third-order filter with two transmission zeros discussed in Chapter 5. The chapter presents another advanced synthesis method of filters - the "non-resonating node" technique. This method inspired two of the works discussed in Chapter 3 and Chapter 4. The step-tuning design technique for designing microwave filters and multiplexers is explained. This technique is used in all filters in this work.

• Chapter 3 presents a new method for synthesis and design of waveguide-based filters with multiple dangling nodes that generate more transmission zeros than the order of the filter. It is used to synthesise a third-order X-band filter with four transmission zeros, which is impossible using the conventional synthesis methods. The filter is designed using rectangular resonators and has a very complex structure impossible to be fabricated in a monolithic part except by using the 3D printing technology.

• Chapter 4 presents another novel synthesis technique for multi-port all-resonator based multiplexers with compact but complicated topologies. The main advantage of this method is that the loading effect of other filter channels are considered during the synthesis of each channel of a multiplexer and an iterative process is applied. This leads to a much faster and

more efficient synthesis of the coupling matrix than the conventional methods based entirely or largely on optimisation. The method is validated by synthesising several multiplexers and diplexers with different topology and complexity.

• Chapter 5 presents the design and fabrication process of a third-order 10 GHz bandpass filter with two transmission zeros. The filter is synthesised using the non-resonating node technique and designed using the step-tuning method. The filter is fabricated using SLM technology using A20X material, and it is analysed using the X-ray imaging technology. The detailed results and analyses are demonstrated in this chapter.

• Chapter 6 presents the design and fabrication of a fifth-order filter with one transmission zero operating at 11.7 GHz. The filter is synthesised using the non-resonating method. A modified rectangular resonator with rounded sides is used to accommodate the printing. The modified resonator offers wider iris opening and allows the structure to be printed without any tilt to the sides and without any internal supports. Titanium alloy Ti64 material is used to print the filter using the SLM technology. The pros and cons of using Ti64 is discussed in this chapter. A dimensional tolerance analysis is performed and the effect of fabrication errors on the performance is investigated.

• Chapter 7 presents a new irregular-hexagonal resonator that compactified filters structure and allows them to be printed vertically without any internal support. This saves space on the printer platform allowing more structures to be printed in one go. The proposed resonator is compared with the conventional rectangular resonator. The modified resonator is used to design three filters with different topologies. All three filters operate at 10 GHz and are printed using SLM technology using A20X material.

• Chapter 8 presents an E-band third-order filter operating at 83.5 GHz. The filter is designed using modified hexagonal resonators offering a more compact-low profile structure compared with rectangular resonators. The geometry allows closely packed resonators to be laid out in a low profile without requiring any internal support structures and without the need of tilting the build as in many rectangular cavity-based filters. Two samples of the filter are fabricated using the MLS technology using stainless steel. The first sample is gold coated as printed. The second sample is electrochemically polished using Hirtisation technique and then gold coated. The polishing technique significantly reduced insertion loss of the filter to a record low level.

• Chapter 9 provides the conclusion of the thesis. Suggestions for future work are also discussed in this chapter.

References

[1] R. J. Cameron, H. Gregg, C. J. Radcliffe and J. D. Rhodes, "Extracted-Pole Filter Manifold Multiplexing," *IEEE Transactions on Microwave Theory and Techniques*, vol. 30, no. 7, pp. 1041-1050, Jul. 1982.

[2] R. J. Cameron, "General coupling matrix synthesis methods for Chebyshev filtering functions," *IEEE Transactions on Microwave Theory and Techniques*, vol. 47, no. 4, pp. 433-442, April 1999.

[3] R. J. Cameron, "Advanced coupling matrix synthesis techniques for microwave filters," *IEEE Transactions on Microwave Theory and Techniques*, vol. 51, no. 1, pp. 1-10, Jan. 2003.

[4] J. D. Rhodes and R. J. Cameron, "General Extracted Pole Synthesis Technique with Applications to Low-Loss TE/sub011/ Mode Filters," *IEEE Transactions on Microwave Theory and Techniques*, vol. 28, no. 9, pp. 1018-1028, Sep. 1980.

[5] R. J. Cameron, A. R. Harish and C. J. Radcliffe, "Synthesis of advanced microwave filters without diagonal cross-couplings," *IEEE Transactions on Microwave Theory and Techniques*, vol. 50, no. 12, pp. 2862-2872, Dec. 2002.

[6] S. Amari, "Direct synthesis of folded symmetric resonator filters with source-load coupling," *IEEE Microwave and Wireless Components Letters*, vol. 11, no. 6, pp. 264-266, June 2001.

[7] J. S. Hong and M. J. Lancaster, *Microstrip Filters for RF/Microwave Applications*. New York, NY, USA: Wiley, 2004.

[8] Y. Yu, B. Liu, Y. Wang, M. J. Lancaster and Q. S. Cheng, "A General Coupling Matrix Synthesis Method for All-Resonator Diplexers and Multiplexers," *IEEE Transactions on Microwave Theory and Techniques*, vol. 68, no. 3, pp. 987-999, March 2020.

[9] Y. Yu, Y. Wang, C. Guo, Q. S. Cheng and M. Yu, "Resonant Manifold Multiplexers," *IEEE Transactions on Microwave Theory and Techniques*, vol. 70, no. 2, pp. 1059-1071, Feb. 2022.

[10] Y. Yu, Z. Zhang, Q. S. Cheng, B. Liu, Y. Wang, C. Guo, and T. T. Ye, "State-of-the-Art: AI-Assisted Surrogate Modeling and Optimization for Microwave Filters," *IEEE Transactions on Microwave Theory and Techniques*, vol. 70, no. 11, pp. 4635-4651, Nov. 2022.

[11] P. Booth and E. V. Lluch, "Enhancing the Performance of Waveguide Filters Using Additive Manufacturing," *Proceedings of the IEEE*, vol. 105, no. 4, pp. 613-619, April 2017.

[12] P. Booth and E. V. Lluch, "Realising advanced waveguide bandpass filters using additive manufacturing." *IET Microwaves, Antennas & Propagation* 11, no. 14 (2017): 1943-1948.

[13] P. Booth, "Additive Manufactured Bandpass Filters at Ka-band," *2019 IEEE MTT-S International Microwave Workshop Series on Advanced Materials and Processes for RF and THz Applications (IMWS-AMP)*, Bochum, Germany, 2019, pp. 7-9.

[14] P. Martin-Iglesias, M. van der Vorst, J. Gumpinger and T. Ghidini, "ESA's recent developments in the field of 3D-printed RF/microwave hardware," *2017 11th European Conference on Antennas and Propagation (EUCAP)*, Paris, France, 2017, pp. 553-557.

[15] X. Wen, Y. Yu, C. Tian, C. Guo, W. Wu, F. Li, Y. Li, and A. Zhang, "An Invar Alloy SLM Printed Diplexer With High Thermal Stability," *IEEE Transactions on Circuits and Systems II: Express Briefs*, vol. 69, no. 3, pp. 1019-1023, March 2022.

[16] F. Zhang, S. Gao, J. Li, Y. Yu, C. Guo, S. Li, M. Attallah, X. Shang, Y. Wang, M. J. Lancaster, And J. Xu, "3-D Printed Slotted Spherical Resonator Bandpass Filters With Spurious Suppression," *IEEE Access*, vol. 7, pp. 128026-128034, 2019.

[17] Y. Zhang, X. Shang, F. Zhang and J. Xu, "A 3-D Printed Ku-Band Waveguide Filter Based on Novel Rotary Coupling Structure," *IEEE Microwave and Wireless Technology Letters*, vol. 33, no. 1, pp. 35-38, Jan. 2023.

[18] T. Skaik, M. Salek, P. Hunyor, H. Wang , P. G. Huggard, P. F. Wilson, M. A. Williams, and Y. Wang, "Evaluation of 3-D Printed Monolithic G-Band Waveguide Components,"

IEEE Transactions on Components, Packaging and Manufacturing Technology, vol. 13, no. 2, pp. 240-248, Feb. 2023.

[19] L. Qian, Y. Wang, S. Li, A. E.-M. A. Mohamed, M. M. Attallah, T. Skaik, P. Booth, L. Pambaguian, C. M. España, and P. M.-Iglesias, "A Narrowband 3-D Printed Invar Spherical Dual-Mode Filter With High Thermal Stability for OMUXs." *IEEE Transactions on Microwave Theory and Techniques*,70, no. 4 (2022): 2165-2173.

[20] T. Skaik, Y. Yu, Y. Wang, P. G. Huggard, P. Hunyor and H. Wang, "3D Printed Microwave Components for Frequencies above 100 GHz," *2021 IEEE MTT-S International Microwave Filter Workshop (IMFW)*, Perugia, Italy, 2021, pp. 246-248.

[21] T. Skaik, D. Wang, P. Hunyor, H. Wang, P. G. Huggard, T. Starke, Q. Zhang, Y. Wang, "A 3D Printed V-Band Twisted Monolithic Waveguide Bandpass Filter," 2023 *53rd European Microwave Conference (EuMC)*, Berlin, Germany, 2023, pp. 231-234.

[22] L. Qian, Y. Baskaran, M. Krödel, C. M. España, L. Pambaguian, T. Skaik, And Y.Wang, "Lightweight, High-Q and High Temperature Stability Microwave Cavity Resonators Using Carbon-Fiber Reinforced Silicon-Carbide Ceramic Composite," *IEEE Journal of Microwaves*, vol. 3, no. 4, pp. 1230-1236, Oct. 2023.

CHAPTER 2

2-PORT COUPLED RESONATOR CIRCUITS

2.1 Introduction

The significance of coupled resonator circuits lies in their pivotal role in the design of RF/microwave filters, particularly bandpass filters essential in various applications. Employing a coupling matrix approach enhances their versatility, allowing representation of a wide array of coupled-resonator filter configurations regardless of resonator type. This chapter elucidates the formulation of the coupling matrix, essential for analysing and synthesizing coupled-resonator filter circuits, focusing on coupling coefficients and external quality factors. By expressing the circuit in matrix format, it becomes notably advantageous, facilitating matrix operations like inversion, similarity transformation, and partitioning. These operations streamline the synthesis, topology adjustment, and performance simulation of complex circuits. Moreover, the coupling matrix encapsulates information for each component of the practical filter, enabling unique identification of each matrix element with an element in the final microwave device.

2.2 Characteristic polynomials

For any two-port lossless *N*th-order filter networks with inter-coupled resonators, the transfer and reflection functions can be defined as a ratio of two polynomials [1],[2].

$$S_{11}(\omega) = \frac{F(\omega)}{\varepsilon_R E(\omega)} \quad S_{21}(\omega) = \frac{P(\omega)}{\varepsilon E(\omega)} \tag{2.1}$$

where ω is the frequency variable, related to the complex frequency variable s by $s = j\omega$. The parameters ε and ε_R are constants, normalizing S_{11} and S_{21} to the equiripple level. The polynomials F, P and E are the characteristic polynomials of the filters. P is created from the Transmission Zeros (TZs) of the filter and can be written as:

$$P(\omega) = \prod_{nz=1}^{Ntz}(\omega - \omega_{nz}) \tag{2.2}$$

where ω_{nz} is the TZ frequency and N_{tz} is the number of TZs. Similarly, the polynomial F is created from the Reflection Zeros (RZs) of the filter and can be written as:

$$F(\omega) = \prod_{n=1}^{N}(\omega - \omega_n) \tag{2.3}$$

where ω_n is the RZ frequency. For an equiripple filters, the location of RZs (roots of F) can be obtained using the well-known method in [1].

$$\text{roots}\big(F(\omega)\big) = \text{roots}(U_N(\omega)) \tag{2.4}$$

where U_N can be obtained through an iterative process from (2.5).

$$U_N(\omega) + V_N(\omega) = \prod_{n=1}^{N}\left[\left(1 - \frac{\omega}{\omega_n}\right) + \omega'\left(1 - \frac{\omega}{\omega_n^2}\right)^{1/2}\right] \tag{2.5}$$

where ω_n refers to the prescribed TZs. U_N and V_N can be defined as:

$$U_N(\omega) = u_0 + u_1\omega + u_2\omega^2 + \cdots + u_N\omega^N \tag{2.6}$$

and

$$V_N(\omega) = \omega'(v_0 + v_1\omega + v_2\omega^2 + \cdots + v_N\omega^N) \tag{2.7}$$

where $\omega'=(\omega^2\text{-}1)^{1/2}$. The iteration starts with the first prescribed TZ (including those at $\omega_n = \infty$), i.e., by putting $n = 1$ in (2.5). Knowing P and F, ε and ε_R can be written as:

$$\varepsilon = \frac{1}{\sqrt{10^{-RL/10}-1}}.\frac{P(\omega)}{F(\omega)}\bigg|_{\omega=1} \tag{2.8}$$

$$\varepsilon_R = \begin{cases} 1 & , \quad N_{tz} < N \\ \frac{\varepsilon}{\sqrt{\varepsilon^2-1}} & , \quad N_{tz} = N \end{cases} \tag{2.9}$$

in which RL is the prescribed return loss in decibels, and it is assumed that the polynomials P and F are normalized to their respective highest degree coefficients. Assuming a lossless network, we can write the unitary condition of the scattering matrix as:

$$E(s)\cdot E^*(-s) = \frac{1}{\varepsilon^2}P(s)\cdot P^*(-s) + \frac{1}{{\varepsilon_R}^2}F(s)\cdot F^*(-s) \tag{2.10}$$

Applying the spectral factorization technique [2], polynomial E can be obtained from its roots from (2.10).

2.3 Deriving coupling matrix for a 2-port network

The derivation of the $N \times N$ coupling matrix is based on Kirchoff's voltage and current laws, explaining the magnetic and electric couplings in the lumped element model of coupled

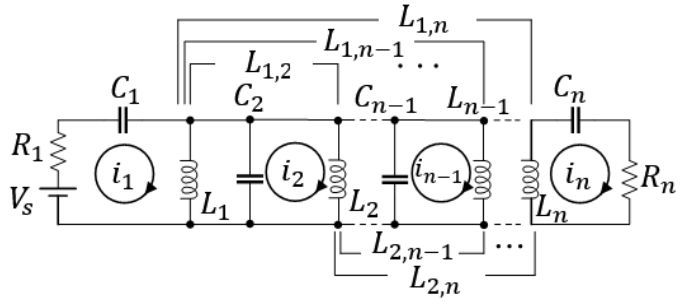

(a)

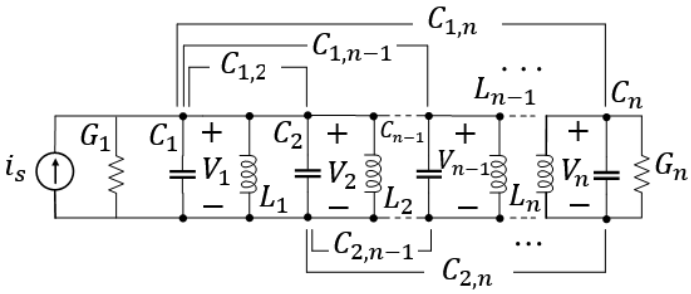

(b)

Figure 2.1 (a) Lumped-element circuit model of magnetically n-coupled resonators. (b) Lumped-element circuit model of electrically n-coupled resonators.

resonators, which is shown in Figure 2.1. Generally, a normalised matrix *A*, which refers to the normalised admittance or impedance matrix of the network, can be obtained through the Kirchoff's voltage and current relations. The elements of *A* contain real parts, imaginary parts, and frequency variant parts. It is possible to separate these three parts of each element of *A* and put them into three matrices called [q] for real parts, [I] for frequency variant parts, and [m] for imaginary parts. [m] and [q] are referred as coupling matrix and external quality factor matrix, respectively. Hence, matrix *A* can be written as

$$A = \underbrace{\begin{bmatrix} \frac{1}{q_{e1}} & 0 & \cdots & 0 \\ 0 & 0 & \cdots & 0 \\ \vdots & \vdots & \ddots & \vdots \\ 0 & 0 & \cdots & \frac{1}{q_{en}} \end{bmatrix}}_{[q]} + P \underbrace{\begin{bmatrix} 1 & 0 & \cdots & 0 \\ 0 & 1 & \cdots & 0 \\ \vdots & \vdots & \ddots & \vdots \\ 0 & 0 & \cdots & 1 \end{bmatrix}}_{[I]} - j \underbrace{\begin{bmatrix} m_{11} & m_{12} & \cdots & m_{1n} \\ m_{21} & m_{22} & \cdots & m_{2n} \\ \vdots & \vdots & \ddots & \vdots \\ m_{n1} & m_{n2} & \cdots & m_{nn} \end{bmatrix}}_{[m]} \tag{2.11}$$

where q_{e1} and q_{en} are normalised external quality factors ($q_e = Q_e \times$ FBW) of the filter, P is the complex lowpass frequency variable, m_{ij} is the normalised coupling coefficient ($m_{ij} = M_{ij}$ / FBW), FBW is the fractional bandwidth (FBW = ($\omega_2 - \omega_1$) / ω_0), and the diagonal elements

(m_{ii}) are the self-coupling of resonators. The value of $[q]$ and $[m]$ matrices can be obtained using the parameters so called g-values representing the circuit elements, i.e., the inductance, capacitance, resistance, and conductance, of the lowpass prototype filter.

$$M_{i,i+1} = \frac{FBW}{\sqrt{g_i g_{i+1}}}, \text{ for } i = 1, \dots, N-1 \tag{2.12}$$

$$Q_{e1} = \frac{g_0 g_1}{FBW}, \qquad Q_{eN} = \frac{g_N g_{N+1}}{FBW} \tag{2.13}$$

For a Chebyshev function, g-values can be obtained by

$$g_0 = 1, \; g_1 = \frac{2a_1}{\gamma}, \; g_k = \frac{4a_{k-1}a_k}{b_{k-1}g_{k-1}}, \; k = 2,3,4, \dots, N \tag{2.14}$$

$$g_{n+1} = \begin{cases} \coth^2(\frac{\beta}{4}), & \text{for } N \text{ even} \\ 1, & \text{for } N \text{ odd} \end{cases} \tag{2.15}$$

$$\beta = \ln\left(\coth\left(\frac{L_{Ar}}{17.37}\right)\right), \; \gamma = \sinh\left(\frac{\beta}{2N}\right), \; L_{Ar} = -10\log(1 - 10^{\frac{-RL}{10}}), \tag{2.16}$$

$$a_k = \sin\left(\frac{(2k-1)\pi}{2N}\right), \; b_k = \gamma^2 + \sin^2\left(\frac{(2k-1)\pi}{2N}\right), \qquad k = 1,2,3, \dots, N \tag{2.17}$$

where *RL* is the return loss in the passband in decibels. The transmission and reflection scattering parameters are expressed in terms of the coupling matrix and the external quality factors as follows [1],

$$S_{21} = \frac{2}{\sqrt{q_{e1}q_{en}}}[A]^{-1}_{n1}, \tag{2.18}$$

$$S_{11} = \pm(1 - \frac{2}{q_{e1}}[A]^{-1}_{11}), \tag{2.19}$$

As an example, the method is used to design a third-order Chebyshev filter with a centre frequency of 9 GHz, bandwidth of 0.5 GHz and return loss of 20 dB in the passband. The obtained coupling matrix of the filter is presented in (2.10). The g-values are calculated using (2.4) to (2.7): $g_0 = 1$, $g_1 = 0.8516$, $g_2 = 1.1032$, $g_3 = 0.8516$, $g_4 = 1$. The filter response is shown in Figure 2.2.

$$M = \begin{bmatrix} 0 & 1.0317 & 0 \\ 1.0317 & 0 & 1.0317 \\ 0 & 1.0317 & 0 \end{bmatrix} \tag{2.20}$$

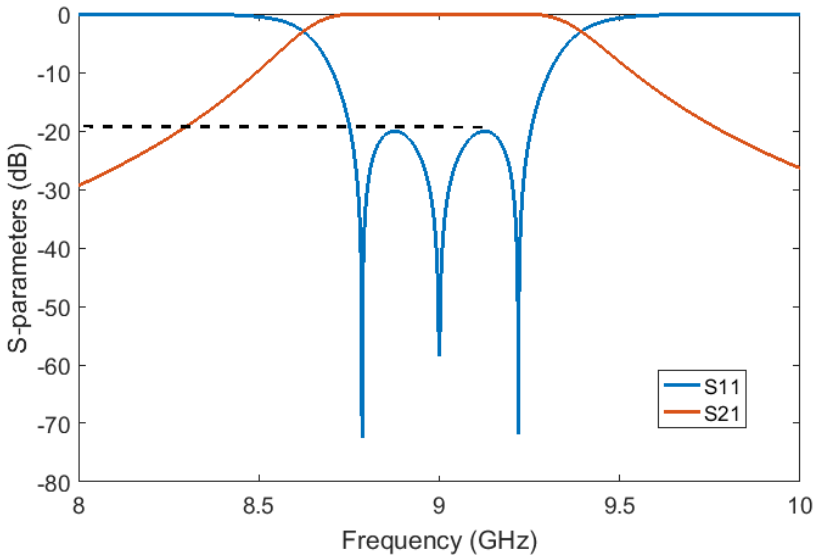

Figure 2.2 S parameters of a third-order Chebyshev bandpass filter.

2.4 Deriving N+2 by N+2 coupling matrix for a 2-port network

The $N + 2$ coupling matrix is the extended form of the $N \times N$ coupling matrix and addresses the coupling between the filter resonators and both the source and load. A $N + 2$ coupling matrix is shown in (2.21) [3].

$$M = \begin{bmatrix} m_{SS} & m_{S1} & \cdots & m_{SN} & m_{SL} \\ m_{1S} & m_{11} & \cdots & m_{1N} & m_{1L} \\ \vdots & \vdots & \ddots & \vdots & \vdots \\ m_{NS} & m_{N1} & \cdots & m_{NN} & m_{NL} \\ m_{LS} & m_{L1} & \cdots & m_{LN} & m_{LL} \end{bmatrix}_{(N+2)\times(N+2)} \tag{2.21}$$

The indexes S and L refer to the source and load. $m_{S,i}$ and $m_{i,S}$ are the coupling between the source and resonator i, $m_{L,i}$ and $m_{i,L}$ are the coupling between the load and resonator i and $m_{S,S}$ and $m_{L,L}$ are the self-coupling of the source and the load, respectively. The $N + 2$ coupling matrix is derived from the filter transformation and reflection functions. For a two-port lossless filter made from N coupled resonators, this is defined as [3]

$$S_{11}(\omega) = \frac{F_N(\omega)}{E_N(\omega)},\ S_{21}(\omega) = \frac{P_N(\omega)}{\varepsilon E_N(\omega)} \tag{2.22}$$

where F_N, P_N and E_N are the characteristic polynomials of the filter explained in Section 2.2 together with ε, which corresponds to the equiripple level of the passband. Having the

expression of polynomials E_N, P_N and F_N, the elements of $N + 2$ coupling matrix can be obtained by the following equations

$$M_{kk} = -\lambda_k,\ M_{Lk} = \sqrt{r_{22k}},\ M_{Sk} = \frac{r_{21k}}{\sqrt{r_{22k}}},\ M_{SL} = K_0 \tag{2.23}$$

where K_0 is 0 unless for the fully canonical filters, in which

$$K_0 = \frac{\varepsilon_R}{\varepsilon(1+\varepsilon_R)} \tag{2.24}$$

λ_k is the eigenvalue of the coupling matrix. r_{22k} and r_{21k} can be obtained by the following equations [1].

If N is even,

$$r_{22k} = \text{residue}(n_1(\text{s})/m_1(\text{s})) \tag{2.25}$$

$$r_{21k} = \text{residue}(P_N(\text{s})/\varepsilon m_1(\text{s})) \tag{2.26}$$

$$\lambda_k = \text{roots}(m_1(\text{s})) \tag{2.27}$$

If N is odd,

$$r_{22k} = \text{residue}(m_1(\text{s})/n_1(\text{s})) \tag{2.28}$$

$$r_{21k} = \text{residue}(P_N(\text{s})/\varepsilon n_1(\text{s})) \tag{2.29}$$

$$\lambda_k = \text{roots}(n_1(\text{s})) \tag{2.30}$$

in which

$$m_1(\text{s}) = \text{Re}(e_0 + f_0) + j\text{Im}(e_1 + f_1)s + \text{Re}(e_2 + f_2)s^2 + \cdots \tag{2.31}$$

$$n_1(\text{s}) = j\text{Im}(e_0 + f_0) + \text{Re}(e_1 + f_1)s + j\text{Im}(e_2 + f_2)s^2 + \cdots \tag{2.32}$$

where, e_k and f_k are coefficients of polynomials E_N and F_N, respectively. It must be noted that, in the fully canonical case, it is necessary to multiply $P(s)$ by j to satisfy the unitary conditions for the scattering matrix. The value of residues given in (2.25), (2.26), (2.28) and (2.29) can be easily obtained using the partial fraction technique. Similar to the $N \times N$ coupling matrix method, the matrix A is given as follows

$$A = \begin{bmatrix} 1 & 0 & \cdots & 0 & 0 \\ 0 & 0 & \cdots & 0 & 0 \\ \vdots & \vdots & \ddots & \vdots & \vdots \\ 0 & 0 & \cdots & 0 & 0 \\ 0 & 0 & \cdots & 0 & 1 \end{bmatrix} + j\omega \begin{bmatrix} 0 & 0 & \cdots & 0 & 0 \\ 0 & 1 & \cdots & 0 & 0 \\ \vdots & \vdots & \ddots & \vdots & \vdots \\ 0 & 0 & \cdots & 1 & 0 \\ 0 & 0 & \cdots & 0 & 0 \end{bmatrix} + j \begin{bmatrix} m_{SS} & m_{S1} & \cdots & m_{Sn} & m_{SL} \\ m_{1S} & m_{11} & \cdots & m_{1n} & m_{1L} \\ \vdots & \vdots & \ddots & \vdots & \vdots \\ m_{nS} & m_{n1} & \cdots & m_{nn} & m_{nL} \\ m_{LS} & m_{L1} & \cdots & m_{Ln} & m_{LL} \end{bmatrix} \tag{2.33}$$

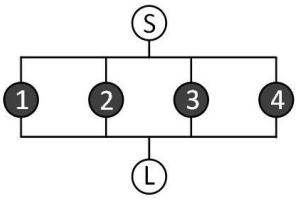

(a)

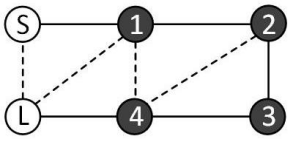

(c)

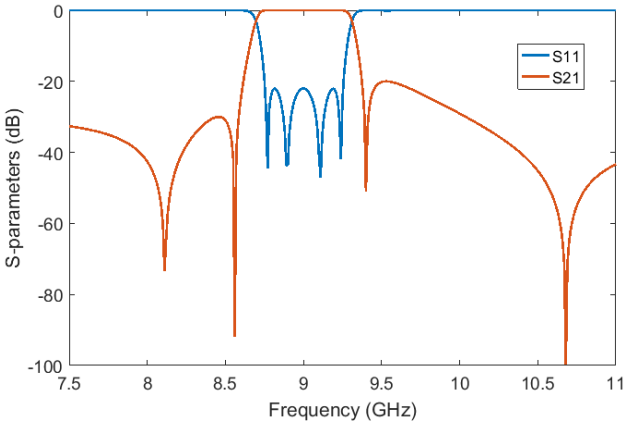

(b)

Figure 2.3 A fully canonical fourth-order Chebyshev bandpass filter (a) The filter topology (b) S parameter of the filter. (c) The filter topology altered to the transversal topology using matrix rotation technique without any change in the S parameters.

The scattering parameters are expressed as [3]

$$S_{21} = 2A_{LS}^{-1} \tag{2.34}$$

$$S_{11} = 1 - 2A_{SS}^{-1} \tag{2.35}$$

Figure 2.3(a) shows the topology of a fourth-order transversal filter, whose $N + 2$ degree coupling matrix, obtained using the method, is presented in (2.36). The filter is considered fully canonical with four transmission zeros at -j3.7431, -j1.8051, j1.5699 and j6.1910 with a return loss of 22 dB in the passband. The S parameters of the filter can be seen in Figure 2.3(b).

$$M = \begin{bmatrix} 0 & 0.3644 & -0.3437 & 0.6678 & -0.6537 & 0.0151 \\ 0.3644 & 1.3142 & 0 & 0 & 0 & 0.3640 \\ -0.3437 & 0 & -1.2968 & 0 & 0 & 0.3431 \\ 0.6678 & 0 & 0 & -0.8042 & 0 & 0.6678 \\ -0.6537 & 0 & 0 & 0 & 0.7831 & 0.6537 \\ 0.0151 & 0.3640 & 0.3431 & 0.6678 & 0.6537 & 0 \end{bmatrix} \tag{2.36}$$

2.5 Matrix rotation

Generally, all the elements of a coupling matrix M can have a non-zero value, which means coupling may exist between any pair of resonators. In most cases, such a coupling matrix will

be impractical. So, it is required to annihilate couplings between some resonators to make a feasible coupling matrix without affecting the transfer and reflection characteristics of the coupling matrix. The matrix rotation technique can fulfil such a requirement. Using the rotation technique, the coupling matrix of a 2-port filter can be converted to different topologies through certain rotation sequences. Rotation of a coupling matrix M is derived from multiplying M by a rotation matrix R and its transpose R_t as follows [3]

$$M_r = R_r . M_{r-1} . R_r^t, \quad r = 1,2, \dots, r_n \tag{2.37}$$

where r_n is the total number of rotations and M_0 and M_r are respectively the original matrix and the matrix after r rotations. The rotation matrix R is defined as a $N + 2$ degree matrix including a pivot of $[i, j]$ $(i \neq j)$, which means elements $R_{ii} = R_{jj} = \cos \theta_r$, $R_{ji} = -R_{ij} = \sin \theta_r$, $(i, j \neq 1, N)$, and θ_r is the angle of the rotation. All other elements of matrix R are zero except for the rest of principal diagonal elements, which are one. As an example, a 7th degree rotation matrix with a pivot of [3, 5] is presented in (2.38).

$$R = \begin{bmatrix} 1 & 0 & 0 & 0 & 0 & 0 & 0 \\ 0 & 1 & 0 & 0 & 0 & 0 & 0 \\ 0 & 0 & C_r & 0 & -S_r & 0 & 0 \\ 0 & 0 & 0 & 1 & 0 & 0 & 0 \\ 0 & 0 & S_r & 0 & C_r & 0 & 0 \\ 0 & 0 & 0 & 0 & 0 & 1 & 0 \\ 0 & 0 & 0 & 0 & 0 & 0 & 1 \end{bmatrix} \tag{2.38}$$

in which, C_r and S_r are defined as $\cos \theta_r$ and $\sin \theta_r$. θ_r is the rotation angle and can be obtained using the following equations

$$\theta_r = \arctan \frac{M_{ik}}{M_{jk}}, \quad \text{for an element in row } i \tag{2.39}$$

$$\theta_r = -\arctan \frac{M_{jk}}{M_{ik}}, \quad \text{for an element in row } j \tag{2.40}$$

$$\theta_r = \arctan \frac{M_{ki}}{M_{kj}}, \quad \text{for an element in column } i \tag{2.41}$$

$$\theta_r = -\arctan \frac{M_{kj}}{M_{ki}}, \quad \text{for an element in column } j \tag{2.42}$$

in which, k $(\neq i, j) = 1, 2, 3, \dots, N$, $C_r = \cos \theta_r$, $S_r = \sin \theta_r$. The rotation technique is applied to the coupling matrix in (2.36) in order to alter the filter topology without changing

Table 2.1 Rotation sequences for annihilating the elements. "*r*" refers to rotation numbers, "*P*" is the pivot and "*E*" is the element to be annihilated. $\theta_r = \arctan(cM_{kl}/M_{mn})$.

r	***P*[*i*,*j*]**	***E***	***k***	***l***	***m***	***n***	***c***
1	[3,4]	M_{S4} in row S	S	4	S	3	-1
2	[2,3]	M_{S3} in row S	S	3	S	2	-1
3	[1,2]	M_{S2} in row S	S	2	S	1	-1
4	[2,3]	M_{2L} in column L	2	L	3	L	1
5	[3,4]	M_{3L} in column L	3	L	4	L	1
6	[2,3]	M_{13} in row 1	1	3	1	2	-1

the filter response. The sequence of annihilating the elements of the transversal matrix is presented in the Table 2.1 and the rotated coupling matrix is presented as (2.43). The resultant filter topology is shown in Figure 2.3(c).

$$M = \begin{bmatrix} 0 & 1.0603 & 0 & 0 & 0 & 0.0151 \\ 1.0603 & -0.0024 & 0.8742 & 0 & -0.3258 & 0.0315 \\ 0 & 0.8742 & 0.0483 & -0.8358 & 0.0341 & 0 \\ 0 & 0 & -0.8358 & -0.0667 & -0.8722 & 0 \\ 0 & -0.3258 & 0.0341 & -0.8722 & 0.0171 & 1.0595 \\ 0.0151 & 0.0315 & 0 & 0 & 1.0595 & 0 \end{bmatrix} \quad (2.43)$$

2.6 Extracted pole synthesis methodology

Extracted pole filters [4],[5] are well known to generate the transmission zeros (TZ) by frequency-invariant elements rather than cross couplings. Benefiting from this feature, filter design with extracted pole techniques can have a more flexible layout. It is useful for many applications, especially when filter topologies cannot be realized because of the restricted mechanical configuration.

Although coupling matrices rotation, discussed in Section 2.5, can treat a wide variety of useful filter configurations, there are certain topologies that are difficult or impossible to synthesize by coupling matrix operations alone. The topologies include any frequency-invariant elements are in this category. In this section, we use the circuit-based method for synthesizing the "extracted pole" section and its direct application in bandpass and bandstop filter design. The extracted pole network can be analysed by using the classical cascaded [*ABCD*] matrix

method. The overall admittance matrix [Y] is built up by the superimposition of the individual $[y]_{2\times2}$ submatrices. These submatrices themselves may make up more than one element and are formed by building the [*ABCD*] matrix of the element and then converting it to [y] parameters.

2.6.1 Synthesis of extracted pole filters using [*ABCD*] matrix

The [*ABCD*] matrices are helpful in constructing the filter equivalent circuit models. The [*ABCD*] matrix of any two-port filter circuit network can be created using the filter's characteristic polynomials ($F(s)$, $P(s)$, $E(s)$) using the following expressions.

$$[ABCD] = \frac{\varepsilon}{P(s)}\begin{bmatrix} A_n(s) & B_n(s) \\ C_n(s) & D_n(s) \end{bmatrix} \tag{2.44}$$

where

$$A_n(s) = \frac{E(s)+\frac{F(s)}{\varepsilon_R}-(-1)^N\left(E(s)+\frac{F(s)}{\varepsilon_R}\right)^*}{2} \tag{2.45}$$

$$B_n(s) = \frac{E(s)+\frac{F(s)}{\varepsilon_R}+(-1)^N\left(E(s)+\frac{F(s)}{\varepsilon_R}\right)^*}{2} \tag{2.46}$$

$$C_n(s) = \frac{E(s)-\frac{F(s)}{\varepsilon_R}+(-1)^N\left(E(s)-\frac{F(s)}{\varepsilon_R}\right)^*}{2} \tag{2.47}$$

$$A_n(s) = \frac{E(s)-\frac{F(s)}{\varepsilon_R}-(-1)^N\left(E(s)-\frac{F(s)}{\varepsilon_R}\right)^*}{2} \tag{2.48}$$

The parameters ε and ε_R are constants, normalizing S_{11} and S_{21} to the equiripple level. The operator (*) refers to the complex conjugate term and the characteristic polynomials are obtained using the method explained in Chapter 2. In this section, it will be shown how to extract the filter circuit elements from the [*ABCD*] matrix. Figure 2.4 shows the prototype circuit model for a resonator section, a TZ producing section and a phase shifter element together with a circuit model of a Chebyshev filter with one TZ section. The resonator section includes a capacitor shunt connected to a reactance. The TZ producing section consists of a frequency-invariant reactance connected in series to an inductor. Series of these three sections (resonators, TZ producing sections and phase shifters), which are shunt connected to each other, creates a network functioning as a filter.

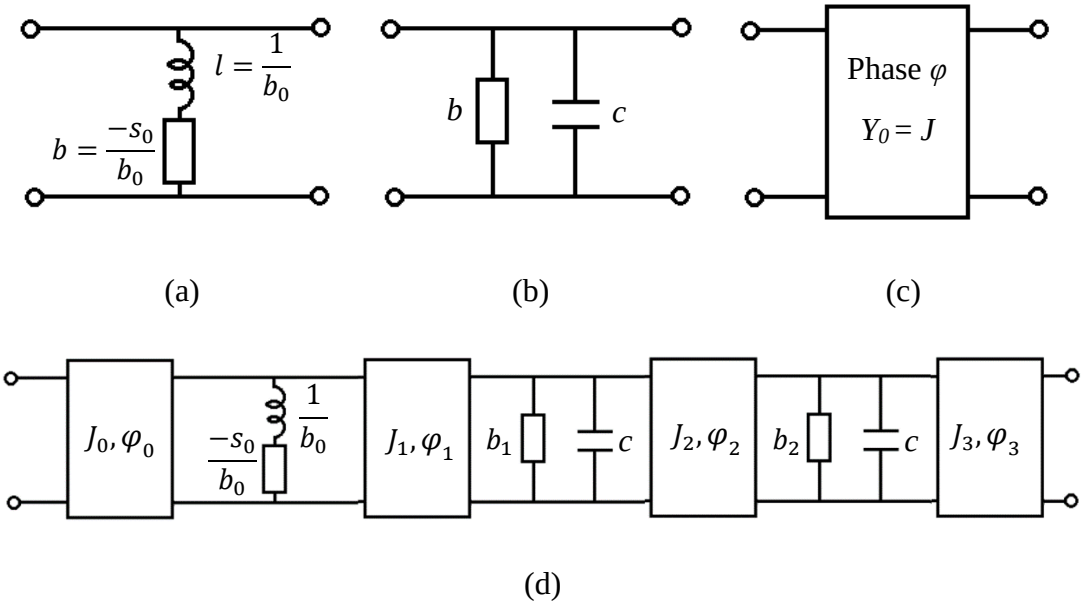

Figure 2.4 (a) A TZ producing section. The TZ is located at $s=s_0$. (b) A resonator section. (c) A phase shifter. (d) The circuit model of a third-order filter with one TZ.

The circuit model of a third-order filter with one TZ is displayed in Figure 2.4(d). Having the [*ABCD*] matrix of a filter circuit model, the circuit element value can be obtained within a process called extracting. The procedure for extracting the elements is the reverse of building up the [ABCD] matrix from the individual elements of the circuit model. In order to extract a TZ producing section, following process can be adopted. First, a phase shifter is extracted using (2.49) and (2.50) and the matrix of the rest of the network is named [*A'B'C'D'*]. Second, the TZ producing element is extracted from [*A'B'C'D'*] using (2.51) and the resultant matrix is named [*A"B"C"D"*] obtained using (2.52). Third, a further phase shifter is extracted from [*A"B"C"D"*] using (2.49) and (2.50) and the resultant matrix is renamed similar to previous two stages. This is only to avoid confusion since this process may be adopted several times in a single synthesis process.

$$\frac{\varepsilon}{P}\begin{bmatrix} A' & B' \\ C' & D' \end{bmatrix} = \frac{\varepsilon}{P}\begin{bmatrix} A\cos\varphi - jC\sin\varphi\,/J & B\cos\varphi - jD\sin\varphi\,/J \\ C\cos\varphi - jAJ\sin\varphi & D\cos\varphi - jBJ\sin\varphi \end{bmatrix} \tag{2.49}$$

in which $A \equiv A(s)$, $B \equiv B(s)$, etc. The value of J is set to 1. Then, φ is obtained using (2.49).

$$\varphi = \tan^{-1}\frac{A}{jC}\Big|_{s=s_0} \tag{2.50}$$

$$b_0 = \frac{(s-s_0)D'}{B'}\Big|_{s=s_0} \tag{2.51}$$

$$\frac{\varepsilon}{P}\begin{bmatrix} A'' & B'' \\ C'' & D'' \end{bmatrix} = \frac{\varepsilon}{P}\begin{bmatrix} A' & B' \\ C' - A'b_0/(s-s_0) & D' - B'b_0/(s-s_0) \end{bmatrix} \tag{2.52}$$

The capacitor, which is denoted using a small-case *c* (the capital-case *C* belongs to the [ABCD] matrix), of the resonator section can be extracted using the following equations.

$$c = \frac{D}{sB}\Big|_{s=j\infty} \tag{2.53}$$

$$A_{\text{rem}} = A \tag{2.54}$$

$$B_{\text{rem}} = B \tag{2.55}$$

$$C_{\text{rem}} = C - scA \tag{2.56}$$

$$D_{\text{rem}} = D - scB \tag{2.57}$$

$$P_{\text{rem}} = P \tag{2.58}$$

The reactance of the resonator section can be obtained using the following equations.

$$b = \frac{D}{B}\Big|_{s=j\infty} \tag{2.59}$$

$$A_{\text{rem}} = A \tag{2.60}$$

$$B_{\text{rem}} = B \tag{2.61}$$

$$C_{\text{rem}} = C - bA \tag{2.62}$$

$$D_{\text{rem}} = D - bB \tag{2.63}$$

$$P_{\text{rem}} = P \tag{2.64}$$

In case of having any cross-couplings with the value of M_{ij} in the network, they can be obtained using the following relations.

$$M_{ij} = -\frac{P}{B}\Big|_{s=j\infty} \tag{2.65}$$

$$A_{\text{rem}} = A \tag{2.66}$$

$$B_{\text{rem}} = B \tag{2.67}$$

$$C_{\text{rem}} = C - \frac{2M_{ij}P}{\varepsilon} + M_{ij}^2 B \tag{2.68}$$

$$D_{\text{rem}} = D \tag{2.69}$$

$$\frac{P_{\text{rem}}}{\varepsilon} = \frac{P}{\varepsilon} + M_{ij}B \tag{2.70}$$

Having the elements extracted, the admittance matrix [*Y*] and subsequently matrix [*A*] of the filter can be created. Where [*A*] = [*Q*] + [*Y*]. [*Q*] is a zero matrix with the same size as [*Y*] and $q_{11} = q_{NN} = 1$. These two elements refer to the loads that are attached to both sides of the network with admittance matrix of [*Y*] and are normalised to 1. Then the S parameters of the filter can be obtained using (2.34) and (2.35). In order to design the filter, the step-tuning method can be adopted. This method is explained in the next chapter. Then, the values of the capacitors (*c*) are scaled to 1. Consequently, the elements values change by the following relations.

$$m_{ij} = \frac{M_{ij}}{\sqrt{c_i c_j}} \tag{2.71}$$

where, m_{ij} refers to the normalised self-couplings ($i = j$) or normalised cross-couplings ($i \neq j$). As an example, a fourth-order filter with two transmission zeros (a 4-2 filter) is synthesised using the described method. The filter topology together with the equivalent circuit model are shown in Figure 2.5. The two TZs are located at 1.6*j* and -1.6*j* with and the central frequency is 11.483 GHz and the bandwidth is 54 MHz with maximum return loss of 20 dB within the passband. The characteristic polynomials of the filter are obtained using the method discussed in Section 2.2.

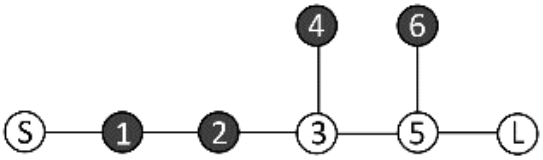

(a)

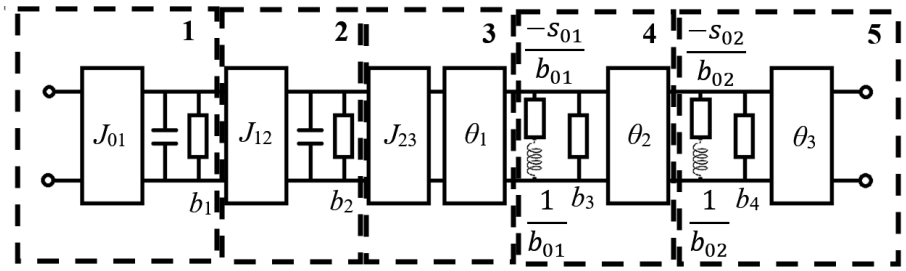

(b)

Figure 2.5 (a) The topology of a 4-2 filter. (b)The lumped element circuit model of the filter. The value of capacitors is normalised to 1.

The [*ABCD*] matrix is created based on the polynomials using (2.43) to (2.47). The coefficients of the characteristic and *ABCD* polynomials of the filter are obtained as listed in Table 2.2. The circuit elements of the network are extracted using the extraction methods discussed early in this section. The element values are listed in Table 2.3. As can be seen in Figure 2.5(b), the lumped circuit model of the filter is divided into five subsections, which are marked out using dash lines. It is noteworthy that the value of capacitors is 1. The admittance matrix of each subsection is obtained using the circuit element values.

Table 2.2 The coefficients of the filter with ε = 1.6315.

s^n	$P(s)$	$F(s)$	$E(s)$	$A(s)$	$B(s)$	$C(s)$	$D(s)$
0	2.56j	0.1577	1.5770	0	1.7347	1.4193	0
1	0	0	2.7994	2.7994	0	0	2.7994
2	1j	1.0616	3.2007	0	4.2623	2.1391	0
3	0	0	2.0684	2.0684	0	0	2.0684
4	0	1	1	0	2	0	0

Table 2.3 The circuit element values.

J_{01}	1.0170	J_{23}	1.0170	φ_3	-44.5°
φ_{01}	90°	φ_{23}	90°	b_{02}	1.2582
b_1	0	J_1	1.1727	J_2	1
J_{12}	0.8819	φ_1	-14.3°	φ_2	48.8°
φ_{12}	90°	b_{01}	2.6262	b_3	-1.7784
b_2	0	J_3	1	b_4	1.2521

Having the circuit elements, the admittance matrix [Y] of the network can be written as in (2.72).

$$Y = \begin{bmatrix} \overbrace{\begin{matrix} -jJ_{01}\cot\theta_{01} & jJ_{01}\csc\theta_{01} \\ jJ_{01}\csc\theta_{01} & sC + jb_1 - jJ_{01}\cot\theta_{01} - jJ_{12}\cot\theta_{12} \end{matrix}}^{Y_1} & \overbrace{jJ_{12}\csc\theta_{12}}^{Y_2} & & \\ \overbrace{jJ_{12}\csc\theta_{12}}^{Y_2} & \overbrace{\begin{matrix} sC + jb_2 - jJ_{12}\cot\theta_{12} + jJ_{23}^2\tan\theta_1 & jJ_{23}\sec\theta_1 \\ jJ_{23}\sec\theta_1 & j\tan\theta_1 + \frac{b_{01}}{s-s_{01}} + jb_3 - j\cot\theta_2 \end{matrix}}^{Y_3} & \overbrace{j\csc\theta_2}^{Y_4} & \\ & \overbrace{j\csc\theta_2}^{Y_4} & \overbrace{\begin{matrix} -j\cot\theta_2 & j\csc\theta_3 \\ j\csc\theta_3 & -j\cot\theta_3 \end{matrix}}^{Y_5} \end{bmatrix} \quad (2.72)$$

$$A = Q + j\omega * I + j * M \quad (2.73)$$

$$A = Y + Q \quad (2.74)$$

Comparing (2.73) with (2.74), the coupling matrix [M] can be extracted by separating the frequency-invariant elements from (2.72). The resulting coupling matrix includes all non-resonating elements together with any phase shifters within the structure. The S parameters of the filter is obtained by putting (2.73) in (2.34) and (2.35). The S parameters are displayed in Figure 2.6.

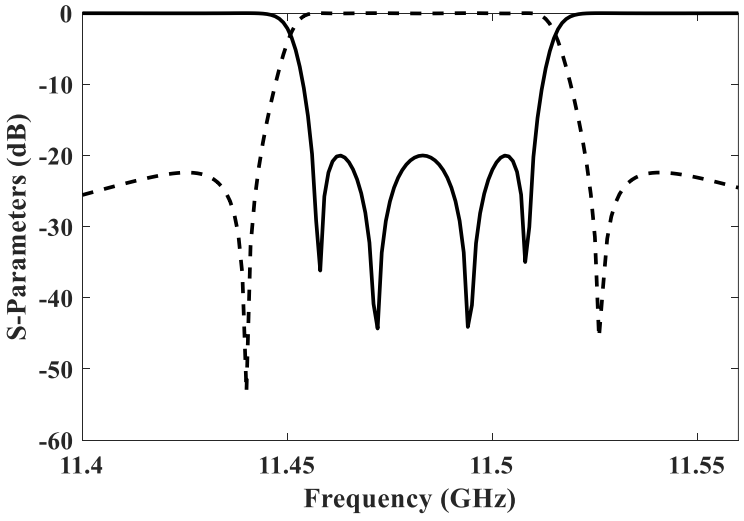

Figure 2.6 The S parameters of the filter obtained using the admittance matrix [Y].

2.6.2 Unified extracted pole technique

The objective of the Unified Extracted Pole technique outlined in [6] is to advance synthesis methods and augment the adaptability of the extracted pole network. With this heightened flexibility, it becomes feasible to assign arbitrary values to parameters defining the TZ structure. The unified extracted Pole method extends the extracted pole approach, which may encounter challenges due to minimal coupling values between elements. To address this issue, the Unified extracted pole method permits the selection of arbitrary values for certain elements, thus mitigating the impact of small couplings. This technique is explained next using an example to synthesis the filter described in Section 2.6.1. It is assumed that all capacitor values are normalised to 1. According to Figure 2.5(b), the first element to be extracted from the *ABCD* matrix is J_{01}, which can be obtained using the following formula [6]

$$J_{01} = \lim_{s\to\infty} \frac{D\cdot s}{B} = 1.0342 \tag{2.75}$$

According to [4], the reactance b_1 and b_2 can have any desired values without affecting the final result of the filter. In this case, b_1 is assumed as 0 in order to ease the EM design process. After extracting the element J_{01}, the rest of the *ABCD* matrix ($ABCD_{\text{new}}$) can be obtained through the following process.

$$ABCD_{\text{new}} = \begin{bmatrix} 0 & j/J_{01} \\ jJ_{01} & 0 \end{bmatrix}^{-1} \begin{bmatrix} A & B \\ C & D \end{bmatrix} = \begin{bmatrix} A' & B' \\ C' & D' \end{bmatrix} \tag{2.76}$$

Next step is derived from extracting J_{12} together with b_2, which is also assumed to be 0 to simplify the filter's lumped element circuit model. The value of J_{12} is obtained using (2.77).

$$J_{12} = \lim_{s\to\infty} \frac{D'\cdot s}{B'} = 0.7220 \tag{2.77}$$

After extracting the elements J_{12}, the rest of $ABCD_{\text{new}}$ matrix can be computed similarly using (2.76). Then, J_{23} is extracted to prepare the network for extracting the first TZ. Another advantage of the unified extracted pole technique is the freedom of choice for the value of J_{23}, which is assumed to be equal to J_{01} to create a symmetric subsection. $ABCD_{\text{new}}$ is obtained again. In this stage, the first TZ should be extracted. First, the phase shifter θ_1 can be obtained using the following formula [4].

$$\theta_1 = \tan^{-1}\left(\frac{B_{\text{new}}(s_{01})}{jD_{\text{new}}(s_{01})}\right) = -18.1591^{\circ} \tag{2.78}$$

After extracting the phase shifter and computing the rest of $ABCD_{new}$ matrix, b_{01} can be obtained using.

$$b_{01} = \frac{A_{\text{new}}(s_{01})}{C_x(s_{01})} = 2.1240 \tag{2.79}$$

where, $C_x = C(s)/(s\text{-}s_{01})$. In order to extract the second TZ, the network need to be turned, meaning to simply replace the element of $A_{\text{new}}(s)$ with $D_{\text{new}}(s)$. Then the phase shifter θ_3 is extracted. The value of θ_3 is obtained using (2.80).

$$\theta_3 = \tan^{-1}\left(\frac{B_{new}(2)}{jD_{new}(s_{02})}\right) = -44.5458^{\circ} \tag{2.80}$$

After obtaining the rest of $ABCD_{new}$ matrix, b_{02} can be obtained using (2.81).

$$b_{02} = \frac{A_{new}(s_{02})}{C_{x_{new}}(s_{02})} = 1.2582 \tag{2.81}$$

Finally, the remaining $ABCD_{new}$ matrix is a constant matrix, which is realised through the following process to get the values of remaining elements of θ_2, b_3 and b_4.

$$\theta_2 = \sin^{-1}(-jB_{new}) = 56.81^{\circ} \tag{2.82}$$

$$b_3 = \frac{D_{new} - \cos\theta_2}{\sin\theta_2} = -01.0313 \tag{2.83}$$

$$b_4 = \frac{\cos\theta_2 - A_{new}}{\sin\theta_2} = 0.9120 \tag{2.84}$$

The values obtained using the unified extracted pole are compared with the normal extracted pole technique is Table 2.4.

2.7 Non-resonating node circuits

The foundational concept of synthesized pole extraction theory was initially formulated in [4], with further refinements suggested in [5]. Non-resonating node (NRN) synthesis techniques were developed in references [2], [7]-[14]. The equivalence between extracted pole and NRN synthesis methods is indicated in [16]. Recently, [15] introduced a methodology for creating cross-coupled networks incorporating both resonator nodes and NRN nodes. NRN synthesis serves as a sophisticated expansion of extracted pole and coupling matrix theories by introducing a new node element, particularly beneficial in comb-line filter design [16].

Table 2.4 The circuit element values obtained from unified and normal extracted pole techniques.

Unified extracted pole				**Extracted pole**			
J_{01}	1.0342	b_{01}	2.6262	J_{01}	1.0170	b_{01}	2.6262
φ_{01}	90º	J_3	1	φ_{01}	90º	J_3	1
b_1	0	φ_3	-44.5º	b_1	0	φ_3	-44.5º
J_{12}	0.7220	b_{02}	1.2582	J_{12}	0.8819	b_{02}	1.2582
φ_{12}	90º	J_2	1	φ_{12}	90º	J_2	1
b_2	0	φ_2	56.8º	b_2	0	φ_2	48.8º
J_{23}	1.0342	b_3	-1.0313	J_{23}	1.0170	b_3	-1.7784
φ_{23}	90º	b_4	0.9120	φ_{23}	90º	b_4	1.2521
J_1	1			J_1	1.1727		
φ_1	-18.2º			φ_1	-14.3º		

An NRN essentially constitutes a node connected to ground via a frequency-invariant reactance. The quantity of NRNs within a given filter is flexible as it doesn't influence the filter's order. Integrating NRNs into cross-coupled configurations allows for highly modular filter design. This approach facilitates the creation of filters with maximal finite transmission zeros without direct source-to-load coupling. A crucial aspect in effectively designing these filters is extracting the circuit model's components. Previous works [17]-[19] presented prototypes featuring NRNs with one or two attenuation poles, extracted either at the input or output. While [17] and [18] employ a series of circuit transformations, the method in [19] is analytical and directly provides circuit elements.

2.7.1 NRN in coupling matrix

Figure 2.7 shows a general lumped element model of a dangling node, which consists of a NRN and a resonator corresponding to a TZ. Let's assume that the dangling node is located at the K^{th} node of a N^{th}-order filter. The equivalent inductance seen from the dangling node is given in

$$y_{in} = \frac{J_K^2}{jB_K + \frac{J_{K+1}^2}{s+jB_{K+1}} + \frac{J_{K+2}^2}{y'_{in}}} \tag{2.85}$$

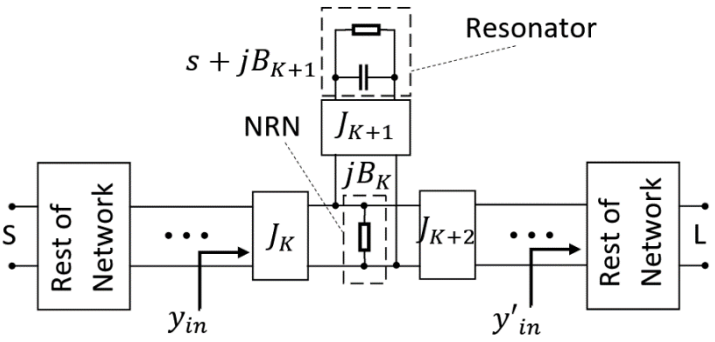

Figure 2.7 General lumped element model of a dangling node.

The corresponding coupling matrix of the dangling node can be written as (2.86).

$$[M_N] = \begin{bmatrix} 0 & \dots & \dots & \dots & \dots & \dots \\ \dots & \dots & J_K & 0 & 0 & \dots \\ \dots & J_K & B_K & J_{K+1} & J_{K+2} & \dots \\ \dots & 0 & J_{K+1} & B_{K+1} & 0 & \dots \\ \dots & 0 & J_{K+2} & 0 & \dots & \dots \\ \dots & \dots & \dots & \dots & \dots & 0 \end{bmatrix} \tag{2.86}$$

Essentially, the value of inductances *B* corresponds to the self-coupling of each node and the value of *J* inverters correspond to the value of cross-couplings between different nodes. It is possible to multiplying the numerator and the denominator of (2.85) with an arbitrary number *A* without changing the input admittance of the dangling node. Consequently, the corresponding elements of the coupling matrix, in (2.86), can be changed as the following equations show.

$$y_{in} = \frac{A^2}{A^2}\left(\frac{J_K^2}{jB_K + \frac{J_{K+1}^2}{s+jB_{K+1}} + \frac{J_{K+2}^2}{y'_{in}}}\right) = \frac{J_K^2/A^2}{jB_K/A^2 + \frac{J_{K+1}^2/A^2}{s+jB_{K+1}} + \frac{J_{K+2}^2/A^2}{y'_{in}}} \tag{2.87}$$

$$[M_N] = \begin{bmatrix} 0 & \dots & \dots & \dots & \dots & \dots \\ \dots & \dots & J_K/A & 0 & 0 & \dots \\ \dots & J_K/A & B_K/A^2 & J_{K+1}/A & J_{K+2}/A & \dots \\ \dots & 0 & J_{K+1}/A & B_{K+1} & 0 & \dots \\ \dots & 0 & J_{K+2}/A & 0 & \dots & \dots \\ \dots & \dots & \dots & \dots & \dots & 0 \end{bmatrix} \tag{2.88}$$

The process of extracting the dangling node circuit elements from its input admittance in (2.87) is discussed in Section 2.7.2.

2.7.2 NRN synthesis technique

NRN synthesis technique is based on extracting filters lumped element circuit elements from its input or output admittance. These elements include resonators, admittance inverters (*J* inverters), and Non-resonating Nodes (NRNs). The resonators are represented by unit capacitors in parallel with frequency-independent reactance *jb*, which accounts for the frequency shifts in their resonant frequencies [2]. The admittance inverters J_i are the coupling coefficients between the nodes. The NRNs represent internal nodes connected to ground by frequency-independent reactance jB_i without any parallel capacitance. The input (source) and the output (load) conductance are also considered $G_S = G_L = 1$. A resonator that is responsible for an attenuation pole at a normalized frequency of $s_i = j\omega_i$ is shown by a unit capacitor in parallel with a constant reactance $jb_i = -j\omega_i$. Such a resonator is only connected to an NRN and called a dangling resonator. For a *N*-order filter with N_Z attenuation poles at finite real frequencies, there are N_Z dangling resonators and $N - N_Z$ resonators along the path between the input and the output. Figure 2.8(a) to Figure 2.8(c) show a fourth-order bandpass filter with two attenuation poles (transmission zeros), which are arranged in three possible topologies. The synthesis approach derived from the reflection coefficient expression, which is written

$$S_{11}(s) = e^{j\phi_{11}} \frac{F_N(s)}{E_N(s)} \tag{2.89}$$

where, $e^{j\varphi_{11}}$ is a real-value phase correction term that has no effect on the return and insertion losses of the filter. Since the source and load conductance are assumed normalized to unity, the input admittance can be written as.

$$y_{in}(s) = \frac{1-S_{11}(s)}{1+S_{11}(s)} \tag{2.90}$$

If the first node from the input side of the network is a resonator, e.g., Figure 2.8(a), the input admittance is asymptotically equivalent to the unit capacitance of the resonator at the resonant frequency. In other words, when $s \to \infty$, $y_{in}(s) \to 0$. Under these conditions, we have

$$e^{j\phi_{11}} = \left.\frac{F_N(s)}{E_N(s)}\right|_{s=\infty} = 1 \tag{2.91}$$

otherwise

$$e^{j\phi_{11}} = \left.\frac{F_N(s)}{E_N(s)}\right|_{s=j\omega_n} \tag{2.92}$$

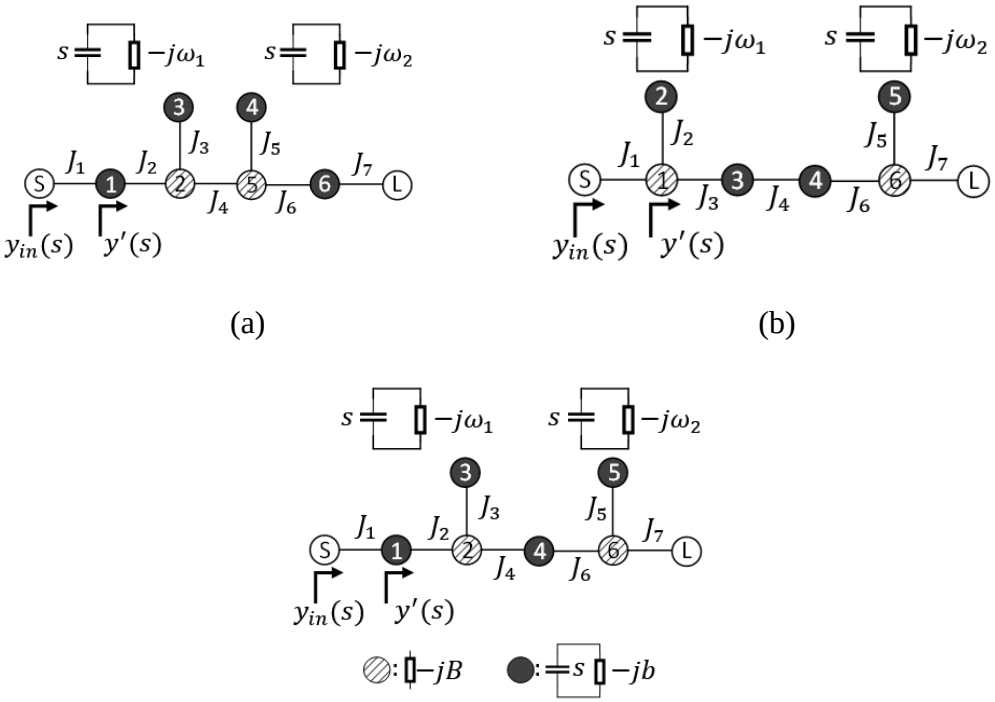

Figure 2.8 A fourth-order band-pass filter with two transmission zeros of ω_n, n = 1, 2. (a)-(c) are three possible arrangements of dangling nodes along the source and load. The black circles represent the resonators, and the hatched circles are the NRNs.

in which ω_n refers to the frequency of the TZ. With the reflection coefficient fully specified, the input admittance can be obtained, and the element extraction process begins. Assuming the first element to be extracted is a resonator (Figure 2.8(a)), the element can be extracted using the following approach.

$$J_1^2 = sy_{in}(s)|_{s=\infty} \;\rightarrow\; y_{\text{rem}}(s) = \frac{J_1^2}{y_{in}(s)} - s = jb + y'(s) \tag{2.93}$$

where

$$b = \text{Im}(y'(s)|_{s=\infty}), \quad \text{if the first node in } y'(s) \text{ is a resonator} \tag{2.94}$$

$$b = \text{Im}\big(y'(s)|_{s=j\omega_n}\big), \quad \text{if the first node in } y'(s) \text{ is a NRN} \tag{2.95}$$

$$y_{\text{rem}}(s) = y_{\text{rem}}(s) - jb \tag{2.96}$$

Here, the extraction cycle of a resonator is completed and y_{rem} is the new input admittance of the remaining of the network. Let's call y_{rem} the new y_{in}. If the first element to be extracted from y_{in} is a NRN (Figure 2.8(b)), the following process is adopted.

$$\frac{J_1^2}{y_{in}(s)} = \frac{J_2^2}{s-j\omega_n} + jB + y'(s) \tag{2.97}$$

Let's assumed $J_1 = 1$ for simplicity. Consequently, (2.97) gives the value of J_2.

$$J_2^2 = J_1^2[\text{residue}\left(\frac{1}{y_{in}(s)}\right)\Big|_{s=j\omega_n}] \tag{2.98}$$

$$y_{\text{rem}}(s) = \frac{J_1^2}{y_{in}(s)} - \frac{1}{s-j\omega_n} = jB + y'(s) \tag{2.99}$$

where

$$B = \text{Im}(y'(s)|_{s=\infty}), \quad \text{if the first node in } y'(s) \text{ is a resonator} \tag{2.100}$$

$$B = \text{Im}\left(y'(s)|_{s=j\omega_n}\right), \quad \text{if the first node in } y'(s) \text{ is a NRN} \tag{2.101}$$

$$y_{\text{rem}}(s) = y_{\text{rem}}(s) - jB \tag{2.102}$$

This completes the extraction cycle, leaving an input admittance $y_{\text{rem}}(s)$. Extracting the resonators and NRN will continue based on the discussed process until the last node. If the last node is a resonator (Figure 2.8(a)), (2.103) to (2.106) must be used.

$$y_{\text{in}}(s) = \frac{J_6^2}{s+jb+J_7^2} \tag{2.103}$$

where J_7 is the inverter connecting the last node to the load $G_{\text{L}} = 1$.

$$J_6^2 = sy_{\text{in}}(s)|_{s=\infty} \tag{2.104}$$

$$y'(s) = \frac{J_6^2}{y_{in}(s)} - s = jb + J_7^2 \tag{2.105}$$

$$b = \text{Im}\left(y'(s)\right) \quad \text{and} \quad J_7^2 = \text{Re}\left(y'(s)\right) \tag{2.106}$$

Otherwise, if the last node is a NRN (Figure 2.8(b)), use (2.107) to (2.109).

$$y_{\text{in}}(s) = \frac{J_5^2}{jB + \frac{J_6^2}{s+j\omega_n} + J_7^2} \tag{2.107}$$

Then

$$J_5^2 = 1 \qquad \text{and} \qquad J_6^2 = \text{residue}\left(\frac{1}{y_{in}(s)}\right)\Big|_{s=j\omega_n} \tag{2.108}$$

$$B = \text{Im}\left(\frac{1}{y_{in}(\infty)}\right) \quad \text{and} \quad J_7^2 = \text{Re}\left(\frac{1}{y_{in}(\infty)}\right) \tag{2.109}$$

by extracting all the resonators and NRNs from the input admittance, the elements of the filter are obtained. As an example, the method is used to synthesise a 3-2 passband filter with a bandwidth of 100 MHz and a central frequency of 9 GHz and return loss of 20 dB with two TZs, which are located at normalised frequencies of $\pm 3j$. The topology of the filter together with its coupling matrix are shown in Figure 2.9. Using the circuit element extraction process discussed early in this section, the elements of the filter topology are obtained as follows: J_1 = 1, J_2 = 2.5285, J_3 = 0.97, J_4 = 1, J_5 = 2.6069, J_6 = 1.031, B_1 = 2.329, b_2 = 3, b_3 = 0, B_4 = -2.475, b_5 = -3. Using these values, the coupling matrix of the filter can be written using the matrix mentioned in Figure 2.9(b). The S parameters of the filter is obtained using its coupling matrix and presented in Figure 2.10.

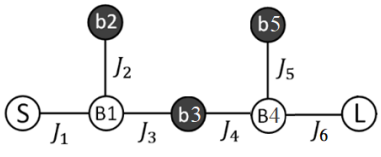

$$\begin{bmatrix} 0.0 & J_1 & 0.0 & 0.0 & 0.0 & 0.0 & 0.0 \\ J_1 & B_1 & J_2 & J_3 & 0.0 & 0.0 & 0.0 \\ 0.0 & J_2 & b_2 & 0.0 & 0.0 & 0.0 & 0.0 \\ 0.0 & J_3 & 0.0 & b_3 & J_4 & 0.0 & 0.0 \\ 0.0 & 0.0 & 0.0 & J_4 & B_4 & J_5 & J_6 \\ 0.0 & 0.0 & 0.0 & 0.0 & J_5 & b_5 & 0.0 \\ 0.0 & 0.0 & 0.0 & 0.0 & J_6 & 0.0 & 0.0 \end{bmatrix}$$

(a) (b)

Figure 2.9 (a) The topology of a third-order filter with two TZs. (b) The corresponding coupling matrix.

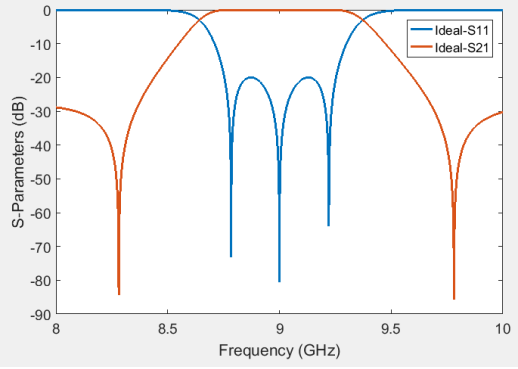

Figure 2.10 The S parameters of the filter.

Having the coupling matrix of a filter, the electromagnetic CAD design process of the filter can be started. There are different techniques to find the physical dimensioning of a filter. One technique is based on comparing the internal and external couplings obtained from the coupling matrix elements with the couplings, obtained from the EM simulations. In other words, the physical dimensioning is performed by changing the dimensions of the filter, so that the external and internal coupling values match with the ones calculated [20]. Another technique is called step-tuning technique [21], in which the physical dimensioning is conducted by comparing the S parameters from the coupling matrix with the ones obtained from the EM simulation. For the filters with NRN topologies, which added more dimensional parameters (each NRN adds an extra resonator and iris) and complexity to the design process compared with the cross-coupling topologies (each cross coupling adds an extra iris only), the step-tuning method is found to have less hassle compared to other method. The step-tuning design technique is adopted in this work to design the filters. This technique is explained in detail in the next section.

2.8 Step-tuning design technique

The step-tuning technique starts with dividing the filter topology into different sections, each of which contain one resonator (with/without ports) or one dangling node (with/without ports). The step-tuning process is explained using an example, in which the filter synthesised in Section 2.7.2 is designed. Figure 2.11 shows the topology of the filter, which is divided into three subsections.

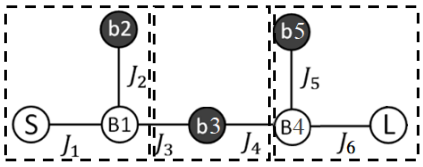

(a)

$$m_7 = \begin{bmatrix} 0.0000 & 1.0000 & 0.0000 & 0.0000 & 0.0000 & 0.0000 & 0.0000 \\ 1.0000 & 2.3290 & 2.5285 & 0.9700 & 0.0000 & 0.0000 & 0.0000 \\ 0.0000 & 2.5285 & 3.0000 & 0.0000 & 0.0000 & 0.0000 & 0.0000 \\ 0.0000 & 0.9700 & 0.0000 & 0.0000 & 1.0000 & 0.0000 & 0.0000 \\ 0.0000 & 0.0000 & 0.0000 & 1.0000 & -2.475 & 2.6069 & 1.0310 \\ 0.0000 & 0.0000 & 0.0000 & 0.0000 & 2.6069 & -3.000 & 0.0000 \\ 0.0000 & 0.0000 & 0.0000 & 0.0000 & 1.0310 & 0.0000 & 0.0000 \end{bmatrix}$$

(b)

Figure 2.11 (a) The topology of the filter divided into three subsections outlined with dashed lines. (b) The corresponding coupling matrix divided to three sub-matrices.

Correspondingly, the coupling matrix is also divided into three sub-matrices, shown in Figure 2.11(b). It is noteworthy that each section may have one or two internal couplings that are converted to external couplings. For example, in Figure 2.12(b), J_3 and J_4 in Figure 2.11 (a) are transformed into J_3' and J_4' using (2.110).

$$J_i' = J_i \times \sqrt{FBW \frac{\pi}{2}\left(\frac{\lambda_g}{\lambda}\right)^2} \tag{2.110}$$

where J_i' represents the external coupling of the submatrix, J_i is the internal coupling in the original coupling matrix, λ and λ_g are the free-space and guided wavelength, respectively. According to (2.110), the transformed coupling coefficient is proportional to λ and λ_g, which can be determined using the following equations [22].

$$\lambda = \frac{c}{f_c} \tag{2.111}$$

$$\lambda_g = \frac{c}{f}\frac{1}{\sqrt{1-\left(\frac{c}{2af_c}\right)^2}} \tag{2.112}$$

where, c, f_c and a are the light velocity, centre frequency of the filter and width of the resonator, respectively. The diagonal elements of the submatrix, which represent the self-coupling of either the resonators or ports, are also adjusted.

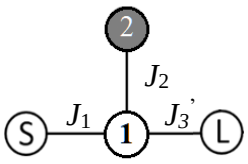

	S	1	2	L
S	0	1	0	0
1	1	2.3290	2.5285	0.2080
2	0	2.5285	3.0000	0
L	0	0.2080	0	0

(a)

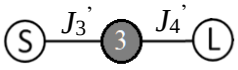

	S	3	L
S	0	0. 2080	0
3	0. 2080	0	0.2145
L	0	0.2145	0

(b)

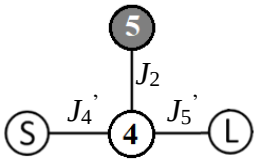

	S	4	5	L
S	0	0.2145	0	0
4	0.2145	-2.475	2.6069	1.0310
5	0	2.6069	-3.000	0
L	0	1.0310	0	0

(c)

Figure 2.12 The three subsections of the filter. (a) First subsection, comprising the NRN-1 and resonator-2. (b) and (c) represent the rest of the subsections.

For instance, in the case of Figure 2.12(b), the diagonal elements corresponding to *S* and *L* are set to zero. This same process is applied to the other subsections. The design of each subsection is carried out utilizing CST Microwave Studio whereby the physical dimensions are optimized such that the S parameters match those obtained from the corresponding coupling submatrix. The response of the coupling submatrices is compared with the EM simulations. The comparison together with the CAD models are shown in Figure 2.13.

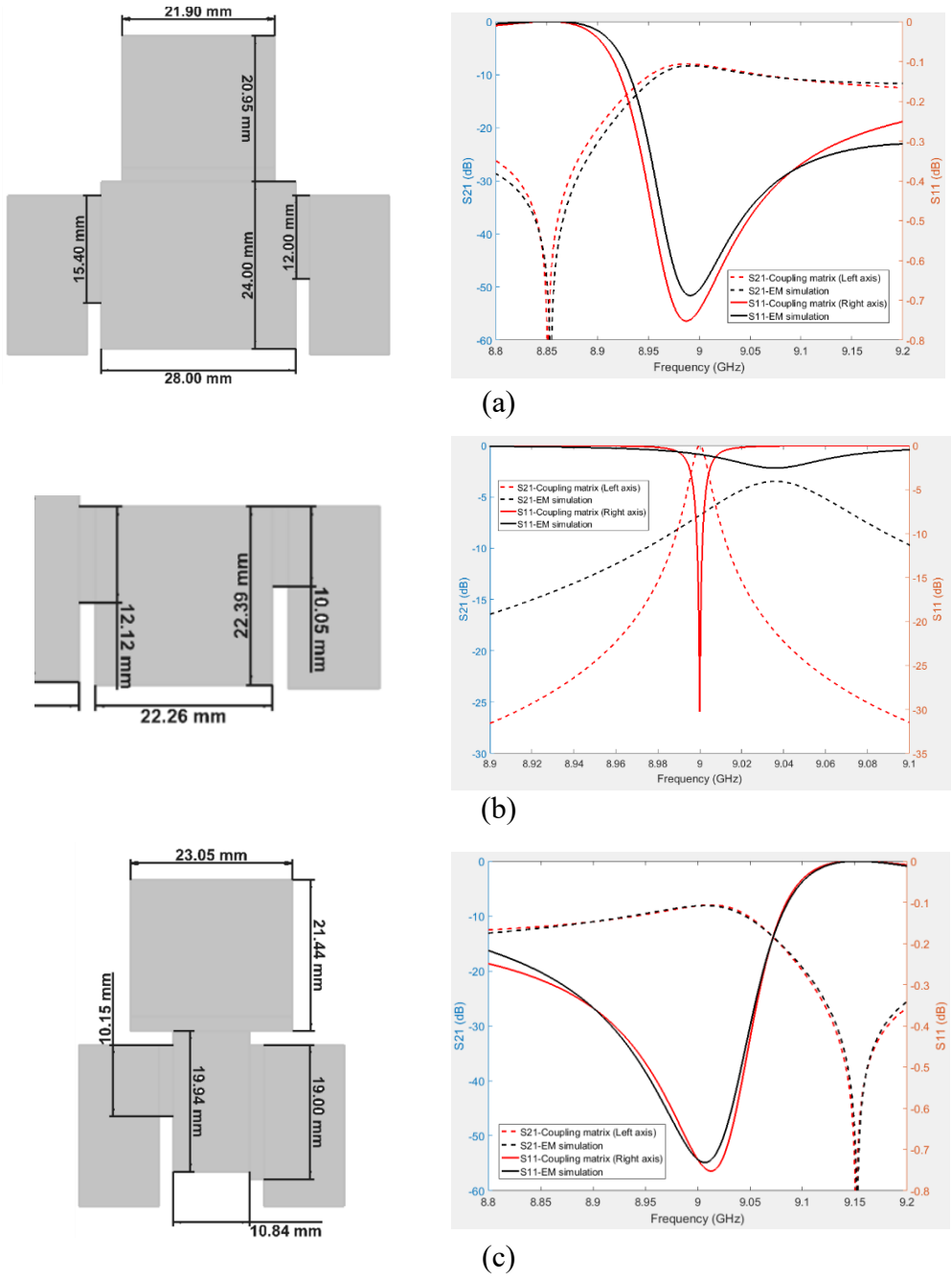

Figure 2.13 The three subsections of the filter designed in CST.

Finally, the five subsections are joined together, and a further optimization is carried out. The S parameter results of the designed filter and its comparison with the coupling matrix are shown in Figure 2.14. The optimized dimensions of the filter are: L_1=29.3 mm, L_2=16.4 mm, L_3=14.9 mm, L_4=15.9 mm, L_5=15.7 mm, L_6=13.9 mm, W_1=14 mm, W_2=12.2 mm, W_3=10.6 mm, W_4=8.5 mm, W_5=8.5 mm, W_6=9 mm, W_7=11.6 mm. Iris thickness is set to 2 mm. As can be seen in Figure 2.13(b), the S parameters obtained from the coupling submatrix of the second subsection deviates significantly from the EM simulation. The reason is that the coupling between the resonator and the dangling node is not unique. In other words, the values of coupling submatrix in Figure 2.12(b) is not unique.

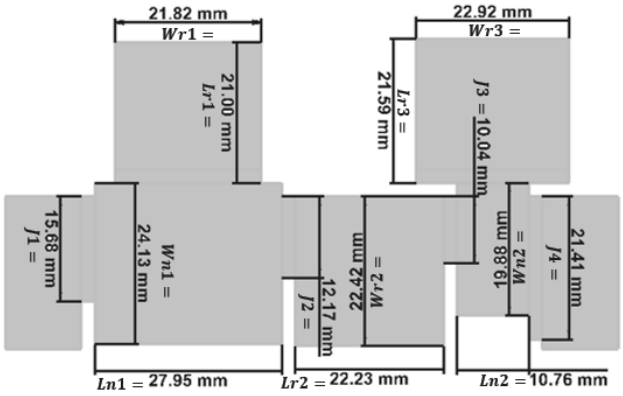

(a)

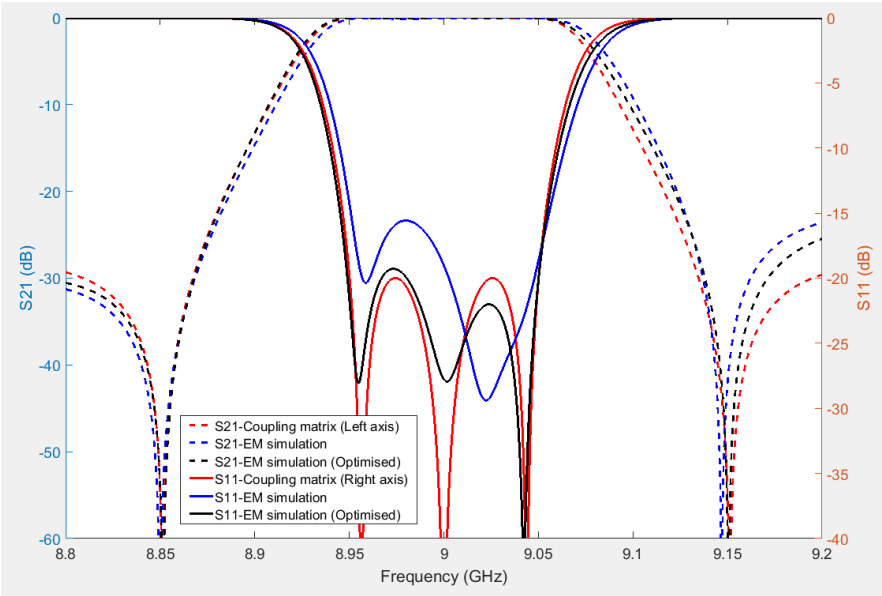

(b)

Figure 2.14 (a) The designed structure. (b) Scattering parameters of the 3-2 filter.

The filter has two dangling nodes, each of which can be multiplied by a different number as explained in Section 2.7.2. (2.113) shows the filter coupling matrix, in which the elements corresponding to the first and second dangling nodes are multiplied with a factor A or B, respectively.

$$m_7 = \begin{bmatrix} 0.0000 & 1.00/A & 0.0000 & 0.0000 & 0.0000 & 0.0000 & 0.0000 \\ 1.00/A & 2.32/A^2 & 2.52/A & 0.97/A & 0.0000 & 0.0000 & 0.0000 \\ 0.0000 & 2.52/A & 3.0000 & 0.0000 & 0.0000 & 0.0000 & 0.0000 \\ 0.0000 & 0.97/A & 0.0000 & 0.0000 & 1.00/B & 0.0000 & 0.0000 \\ 0.0000 & 0.0000 & 0.0000 & 1.00/B & -2.4/B^2 & 2.60/B & 1.03/B \\ 0.0000 & 0.0000 & 0.0000 & 0.0000 & 2.60/B & -3.000 & 0.0000 \\ 0.0000 & 0.0000 & 0.0000 & 0.0000 & 1.03/B & 0.0000 & 0.0000 \end{bmatrix} \quad (2.113)$$

By choosing a suitable value for the factors, i.e., A=0.3030 and B=0.8333, the submatrix of the resonator can be modified to be closer to the EM simulation. The S parameters are compared in Figure 2.15. As can be seen, the responses are now almost identical.

$$m_3 = \begin{bmatrix} 0.0000 & 0.20/A & 0.0000 \\ 0.20/A & 0.0000 & 0.21/B \\ 0.0000 & 0.21/B & 3.0000 \end{bmatrix} \quad (2.114)$$

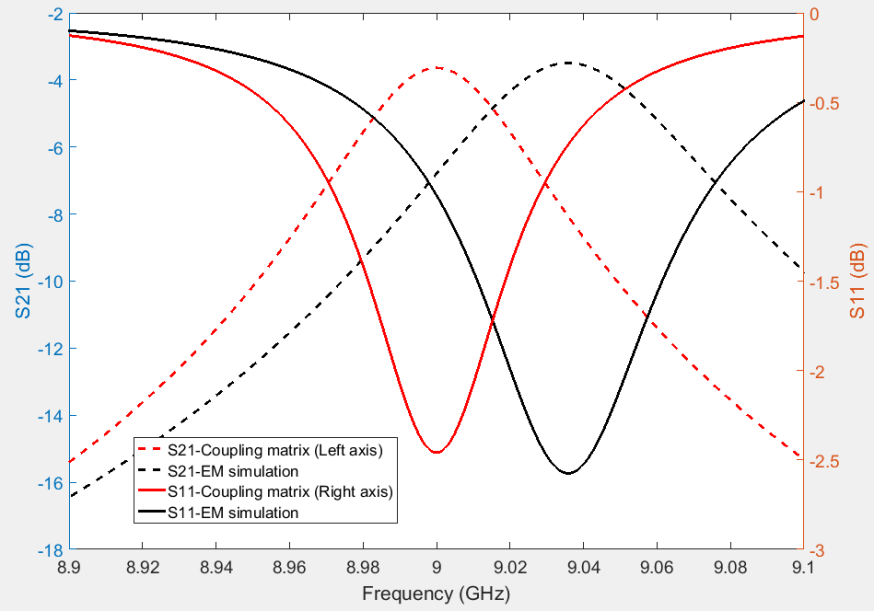

Figure 2.15 Comparison of the S parameters obtained from (2.114) versus EM simulation of central resonator of the 3-2 filter.

2.9. Summary

This chapter discusses different methods for synthesising and generating the coupling matrix of a Chebyshev filter. The covered methods are the synthesis of a filter using the *g*-values, the (N+2) × (N+2) coupling matrix method, extracted pole and unified extracted pole techniques and the NRN synthesis method. A matrix rotation technique is also described in order to alter a (N+2) × (N+2) coupling matrix from a specific topology to its other equivalent ones. Some examples are demonstrated to verify the methods. In addition, the step-tuning design technique for EM modelling of the synthesised filters is briefly explained in this chapter using an example. This technique is adopted to the design of all filters in this work.

References

[1] R. J. Cameron, "General coupling matrix synthesis methods for Chebyshev filtering functions," *IEEE Transactions on Microwave Theory and Techniques*, vol. 47, no. 4, pp. 433-442, April 1999.

[2] S. Amari and G. Macchiarella, "Synthesis of inline filters with arbitrarily placed attenuation poles by using nonresonating nodes," *IEEE Transactions on Microwave Theory and Techniques*, vol. 53, no. 10, pp. 3075-3081, Oct. 2005.

[3] R. J. Cameron, "Advanced coupling matrix synthesis techniques for microwave filters," *IEEE Transactions on Microwave Theory and Techniques*, vol. 51, no. 1, pp. 1-10, Jan. 2003.

[4] J. D. Rhodes and R. J. Cameron, "General Extracted Pole Synthesis Technique with Applications to Low-Loss TE/sub011/ Mode Filters," *IEEE Transactions on Microwave Theory and Techniques*, vol. 28, no. 9, pp. 1018-1028, Sep. 1980.

[5] J. R. M.-Garai, J. A. R.-Cruz, J. M. Rebollar, M. J. P.-Cruz, A. O.-Navarro and I. H.-Carpintero, "Synthesis and design of in-line N-order filters with N real transmission zeros by means of extracted poles implemented in low-cost rectangular H-plane waveguide," *IEEE Transactions on Microwave Theory and Techniques*, vol. 53, no. 5, pp. 1636-1642, May 2005.

[6] Y. Yang, M. Yu, Q. Wu, X. Yin and J. Yang, "A Fully Integrated Multiplexer Using Unified Extracted Pole Technique," *IEEE Transactions on Microwave Theory and Techniques*, vol. 68, no. 8, pp. 3439-3447, Aug. 2020.

[7] S. Amari and U. Rosenberg, "New in-line dual- and triple-mode cavity filters with nonresonating nodes," *IEEE Transactions on Microwave Theory and Techniques,* vol. 53, no. 4, pp. 1272–1279, Apr. 2005.

[8] G. Macchiarella, "Generalized coupling coefficient for filters with non-resonant nodes," *IEEE Microwave and Wireless Components Letters,* vol. 18, no. 12, pp. 773–775, Dec. 2008.

[9] G. Macchiarella and M. Politi, "Use of generalized coupling coefficients in the design of extracted-poles waveguide filters with non-resonating nodes," *IEEE MTT-S International Microwave Symposium Digest,* Jun. 2009, pp. 1341–1344.

[10] S. Cogollos, R. J. Cameron, R. R. Mansour, M. Yu, and V. E. Boria, "Synthesis and design procedure for high performance waveguide filters based on nonresonating nodes," *IEEE MTT-S International Microwave Symposium Digest,* Jun. 2007, pp. 1297–1300.

[11] A. E. Atia and A. E. Williams, "General TE011-mode waveguide bandpass filters," *IEEE Transactions on Microwave Theory and Techniques,* vol. MTT-24, no. 10, pp. 640–648, Oct. 1976.

[12] S. Amari, U. Rosenberg, and J. Bornemann, "Singlets, cascaded singlets, and the nonresonating node model for advanced modular design of elliptic filters," *IEEE Microwave and Wireless Components Letters,* vol. 14, no. 5, pp. 237–239, May 2004.

[13] S. Amari and U. Rosenberg, "New building blocks for modular design of elliptic and self-equalized filters," *IEEE Transactions on Microwave Theory and Techniques,* vol. 52, no. 2, pp. 721–736, Feb. 2004.

[14] S. Amari, J. Bornemann, W. Menzel, and F. Alessandri, "Diplexer design using pre-synthesized waveguide filters with strongly dispersive inverters," *IEEE MTT-S International Microwave Symposium Digest,* May 2001, pp. 1627–1630.

[15] S. Tamiazzo and G. Macchiarella, “Synthesis of cross-coupled prototype filters including resonant and non-resonant nodes,” *IEEE Transactions on Microwave Theory and Techniques*, vol. 63, no. 10, pp. 3408–3415, Oct. 2015.

[16] R. J. Cameron, C. M. Kudsia, and R. R. Mansour, *Microwave Filters for Communication Systems*. New York, NY, USA: Wiley, 2018.

[17] G. Macchiarella, “Synthesis of an in-line prototype with two transmission zeros without cross-coupling,” *IEEE Microwave and Wireless Components Letters*, vol. 14, no. 1, pp. 19–21, Jan. 2004.

[18] G. Macchiarella and M. Fumagalli, “In-line combline filter with one or two transmission zeros,” *IEEE MTT-S International Microwave Symposium Digest*, Jun. 2004, pp. 1085–1088.

[19] S. Amari and U. Rosenberg, “Synthesis and design of novel in-line cavity filters with one or two real transmission zeros,” *IEEE Transactions on Microwave Theory and Techniques*, vol. 52, no. 5, pp. 1464–1478, May 2004.

[20] J. S. Hong and M. J. Lancaster, *Microstrip Filters for RF/Microwave Applications*. New York, NY, USA: Wiley, 2004.

[21] X. Shang, W. Xia, and M. J. Lancaster, “The design of waveguide filters based on cross-coupled resonators,” *Microwave and Optical Technology Letters*, vol. 56, no. 1, pp. 3–8, 2014.

[22] D. M. Pozar, *Microwave engineering*. John wiley & sons, 2009.

CHAPTER 3

SYNTHESIS, DESIGN, AND FABRICATION OF FILTERS WITH DUAL/MULTIPLE DANGLING NODES

Paper in submission

Abolfazl Mostaani*, Yi Wang*, Frederick Huang*, Lu Qian*, Abd El-Moez A. Mohamed**, Moataz M. Attallah**

IEEE Journal of Microwave

A. Mostaani proposed the method and designed the filters and wrote the manuscript in collaboration with Y. Wang. F. Huang shared technical advice on the method. L. Qian assisted in the measurements. A. E.-M. A. Mohamed and M. M. Attallah fabricated the designed filters.

* School of Engineering University of Birmingham, Birmingham, U.K

** School of Metallurgy and Materials, University of Birmingham, Birmingham, U.K.

3.1 Introduction

Microwave filters are widely used in terrestrial and satellite communication systems. Chebyshev filters with in-band equiripple feature, accompanied with high selectivity due to the sharp roll-off at the edges of the passband, offers a fair trade-off between the signal degradation and noise rejection. Introducing cross-couplings and non-resonating nodes (NRNs) provides the ability of creating transmission zeros (TZs) to increase the near-band rejection slope and therefore increase the frequency selectivity. This is highly desired in many applications because the frequency spectrum has become increasingly crowded. Moreover, the TZs can help reduce the required filter order and, therefore, minimizing insertion loss, mass and size as compared with higher order filters, achieving the same amount of passband roll-off. A key advantage of using NRNs over cross-couplings is that the NRN offers a high level of modularity in the design of filters [1]-[5]. It is known for a typical Chebyshev filter to have a maximum number of TZs equal to the order of the filter [1],[2]. In [6]-[15], filters with multiple extra TZs are presented. However, these filters are all planar structures, not suitable for the demanding high-performance application due to their high level of loss compared to cavity-based filters.

Moreover, neither an analytical method for creating the coupling matrix with such extra TZs nor a design process are given in the literature. In [16], a technique for generating additional TZs in cavity-based filters is presented. The technique is based on cross-couplings, which reduces the design flexibility due to the multiple cross-couplings between the resonators and between the source and load.

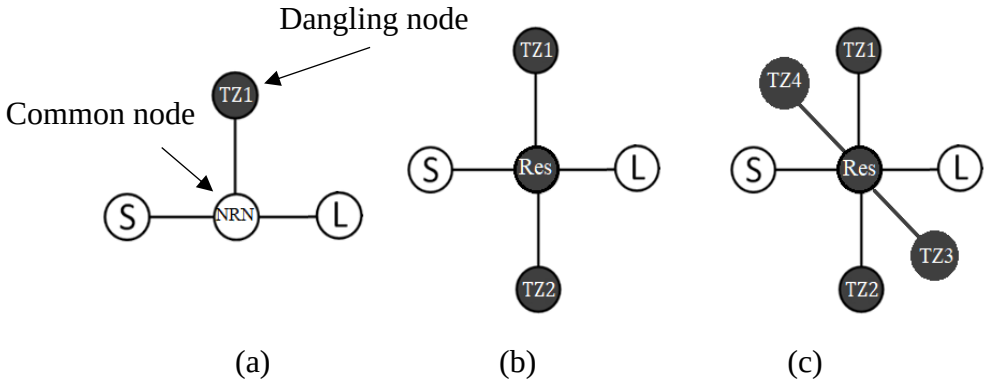

Figure 3.1 (a) A conventional NRN with a dangling node. (b) Proposed dual dangling node. All the nodes are considered as resonators. (c) A quad dangling node.

This paper presents a synthesis and design approach to generate a higher number of TZs than the filter order in cavity-based filters. The term "filter order" in this paper refers to the number of in-band reflection zeros (RZs). The method is inspired by the NRN technique. In the conventional NRN approach (Figure 3.1(a)), each dangling node attaches to a single NRN and creates one in-band RZ and one TZ [1],[2]. In a dual dangling node, on the other hand, all the nodes are considered as resonators. The common resonator (common node) creates an in-band RZ, and the two dangling nodes generate two TZs and two out-band RZs (Figure 3.1(b)) [17],[18]. In [11], a technique with similar dual dangling node, where two dangling resonators are attached to an NRN, is proposed. The technique is limited to two dangling nodes and only demonstrated for planar or lumped-element structures. Another technique for cavity-based filters with multiple-dangling nodes is presented in [19], based on the concept of bandstop resonator sections. The technique assumed the common node, to which the dangling nodes are attached, as a NRN without considering the real part of the RZs, which are generated by the multiple-dangling nodes. The proposed method in our work takes a very different approach. It is more general. It can be extended to the case of multiple dangling resonators (e.g., Figure 3.1(c)), where conventional synthesis method becomes ineffective. The dual/multiple dangling node structure also leads to complexity of the filter structure and consequently fabrication difficulty. This paper will demonstrate that 3D-printing technology can remove the fabrication barrier of such structures. The first part of this paper describes a technique for generating the transfer and reflection polynomials. This is followed by a method to generate the coupling matrix of the filters with dual/multiple dangling nodes. Two third-order filters with two TZs, created by a single dual dangling resonator, are used to exemplify the synthesis and design process. Finally, two third-order filters with four TZs are prototyped. One of the prototyped filters is fabricated to verify the method.

3.2 Polynomial synthesis

For any two-port lossless *N*th-order filter networks with inter-coupled resonators, the transfer and reflection functions can be defined as a ratio of two polynomials [1],[2].

$$S_{11}(\omega) = \frac{F(\omega)}{\varepsilon_R E(\omega)} \quad S_{21}(\omega) = \frac{P(\omega)}{\varepsilon E(\omega)} \tag{3.1}$$

where ω is the frequency variable, related to the complex frequency variable s by $s = j\omega$. The parameters ε and ε_R are constants, normalizing S_{11} and S_{21} to the equiripple level. The

polynomials *F*, *P* and *E* are the characteristic polynomials of the filters. *P* is created from the TZs of the filter and can be written as:

$$P(\omega) = \prod_{nz=1}^{Ntz}(\omega - \omega_{nz}) \tag{3.2}$$

where ω_{nz} is the TZ frequency and *Ntz* is the number of TZs. Similarly, the polynomial *F* is created from the in-band and out-band RZs of the filter and can be written as:

$$F(\omega) = \prod_{np=1}^{Np}(\omega - \omega_{np}) \tag{3.3}$$

where ω_{np} is the RZ frequency and *Np* is the number of RZs. For conventional equiripple filters, the location of in-band RZs can be obtained using the well-known method in [1]. However, when two or more dangling resonators are attached to a single resonator, the out-band RZs appear in the filter S parameters and the value of such RZs cannot be found using the same method, because the out-band RZs have real parts. In this paper, the polynomial synthesis process is triggered by the value of in-band RZs and the approximated value of out-band RZs. The in-band RZs are found using the method in [1]. The out-band RZs are not unique and approximated to be close to the TZs. This is discussed in Section 3.3.1. Knowing *P* and *F*, the ε and ε_R can be written as:

$$\varepsilon = \frac{1}{\sqrt{10^{-RL/10}-1}} \cdot \left.\frac{P(\omega)}{F(\omega)}\right|_{\omega=\omega_i} \tag{3.4}$$

$$\varepsilon_R = \begin{cases} 1 & , \quad N_{tz} < N \\ \frac{\varepsilon}{\sqrt{\varepsilon^2-1}} & , \quad N_{tz} = N \end{cases} \tag{3.5}$$

in which *RL* is the prescribed return loss in decibels, and it is assumed that the polynomials *P* and *F* are normalized to their respective highest degree coefficients. ω_i refers to the frequency, at which the return loss is required to be equal to the prescribed *RL*. For instance, for equiripple filters, ω_i is equal to ±1. Assuming a lossless network, we can write the unitary condition of the scattering matrix as:

$$E(s) \cdot E^*(-s) = \frac{1}{\varepsilon^2} P(s) \cdot P^*(-s) + \frac{1}{{\varepsilon_R}^2} F(s) \cdot F^*(-s) \tag{3.6}$$

Applying the spectral factorization technique, polynomial *E* can be obtained from its roots from (3.6). It is also possible to adapt the iterative method, proposed in [17], for obtaining the characteristic polynomials of filters with dual/multiple dangling nodes. To do so, once *F* and

in-band RZs (roots of *F*) are obtained, the approximated out-band RZs are added to the roots of *F*. The number of out-band RZs depends on the number of dual/multiple dangling nodes added to the filter topology. Each dangling node corresponds to one extra out-band RZ. It is noteworthy that these extra out-band RZs have real parts. Then *F* is regenerated from the in-band and out-band RZs and *E* is obtained using (3.6). The iteration starts with the initial value of the out-band RZs and continues by updating the out-band RZs until the constrains are satisfied at the location of TZs as explained in [17]. As an example, the characteristic polynomials of a third-order filter (3 in-band RZs) with four TZs and four out-band RZs are obtained using the same process and presented in Table 3.1. The RZs are located at 0.866*j*, 0, -0.866*j*, in-band, and 0.22-3.5*j*, 0.22+3.5*j*, 0.42-4.5*j* and 0.22+4.5*j* outside the passband. The RL is set to 20 dB and the location of TZs are ±3*j*, ±4*j*. The S parameters derived from the polynomials are shown in Figure 3.2. As can be seen from Figure 3.2, the out of band rejection deteriorates due to the out-band RZs that lead to the peaks adjacent to the TZs. The deterioration worsens by increasing the number of dangling nodes attached to a common node. Such adverse effects can be partially mitigated by electromagnetic design and will be discussed later in Section 3.4. The level of the out-band peaks is largely defined by the real part of the out-of-band RZs. Since the real part can have different values, the polynomials giving similar in-band behaviour are not unique. However, in practice, not all these different polynomials can be implemented as filters with dual/multiple dangling node topologies. It is not possible to adjust the real part while the imaginary part is fixed. The location of the out-band RZs can be optimized in order to maximize the out-band rejection. Some examples will be presented in Section 3.3.2 to demonstrate this.

Table 3.1 Coefficients of characteristic polynomials

n	***P*(*ω*)**	***F*(*ω*)**	***E*(*ω*)**
0	144	0	27.78-654.41*j*
1	0	-187.62+8.3*j*	-916.97-38.93*j*
2	-25	-0.3-12.62*j*	-29.26+729.22*j*
3	0	274.87-11.74*j*	407.35+14.98*j*
4	1	0.4+17.63*j*	2.48-100.22*j*
5	0	-33.67+0.9*j*	-38.95-0.89*j*
6	0	-1.08*j*	3.42*j*
7	0	1	1
$\varepsilon_R = 1$		$\varepsilon = 0.2198$	

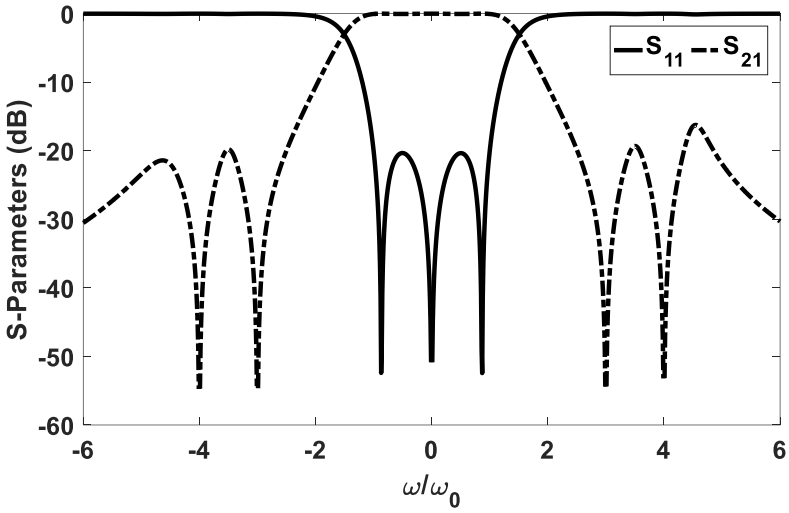

Figure 3.2 S parameters obtained from the characteristic polynomials in Table 3.1.

3.3 Coupling matrix for multiple dangling nodes

In this section, a method is presented in order to create the coupling matrix of filters with extra TZs using the characteristic polynomials.

3.3.1 Coupling matrix synthesis of a multiple dangling node

First, an analytical method for the synthesis of a multiple dangling nodes is presented using an example of a dual dangling node, displayed in Figure 3.3(a) together with its equivalent circuit model in Figure 3.3(b). Note that the common node is treated as a resonator rather than an NRN. The validity of this assumption is explained in the Appendix. The input admittance of a dual/multiple-dangling node can be written as

$$Y_{in} = \frac{1-S_{11}}{1+S_{11}} = \frac{\varepsilon_r E(s)-F(s)}{\varepsilon_r E(s)+F(s)} \tag{3.7}$$

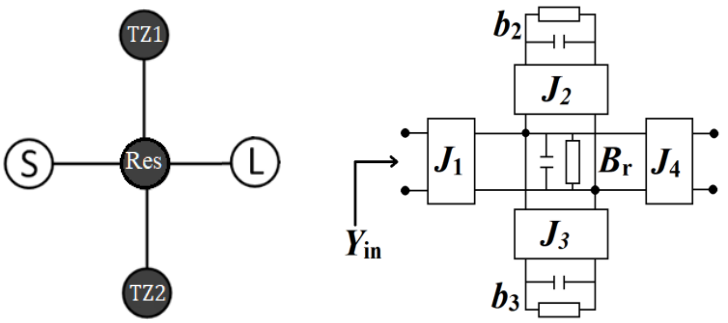

(a) (b)

Figure 3.3 (a) Topology of a dual dangling node. (b) Equivalent circuit model.

in which, the value of circuit elements in Figure 3.3(b), i.e., b_2, b_3, B_R, J_1, J_2, J_3, J_4, can be directly extracted from (3.7) using the following expressions [2]

$$J_1 = \sqrt{\lim_{s\to\infty} sY_{in}} \tag{3.8}$$

$$Y'_{in} = \frac{J_1^2}{Y_{in}} - s \tag{3.9}$$

$$B_r = \mathrm{Im}\left(\lim_{s\to\infty} Y'_{in}\right) \tag{3.10}$$

$$J_4 = \sqrt{\mathrm{Re}\left(\lim_{s\to\infty} Y'_{in}\right)} \tag{3.11}$$

$$J_n = \sqrt{\lim_{s\to jb_n} ((s+jb_n).Y'_{in})} \text{ for } n=1,2,\ldots \tag{3.12}$$

where n refers to the index of the dangling nodes and J_n represents the value of the inverter (coupling) between the common node and the dangling nodes. For a dual dangling node, n=1, 2. b_n is the susceptance of the dangling nodes corresponding to the location of TZs. These circuit element values can be used to create the coupling matrix of the filter as follows:

$$M = \begin{bmatrix} 0 & J_1 & 0 & 0 & 0 \\ J_1 & B_R & J_2 & J_3 & J_4 \\ 0 & J_2 & b_2 & 0 & 0 \\ 0 & J_3 & 0 & b_3 & 0 \\ 0 & J_4 & 0 & 0 & 0 \end{bmatrix} \tag{3.13}$$

The synthesis process described in this section can be used to analyse any multi-dangling nodes through the following steps:

1) Pre-estimate the location of TZs to satisfy the out-band rejection and obtain the in-band RZs using the Chebyshev equations [1].
2) For each dangling resonator, one TZ and one out-of-band RZ are considered. The location of the out-of-band RZ should be set next to the TZ, away from the central frequency. This gives a good estimation of the out-of-band behaviour of the polynomials. If two or more TZs are next to each other, one out-of-band RZ is assumed between each pair of TZs. This is further discussed and verified in Appendix section. It must be noted that the out-of-band RZs have a real part, so the exact frequency of the

out-of-band RZs cannot be found, unless by means of weak input and output couplings. From experience with simulation, a good initial estimation of the out-of-band RZ location is $\omega = \omega_{TZ} \pm 0.5$, where ω and ω_{TZ} are the normalized frequencies of the out-of-band RZ and TZs, respectively. If the estimation ends up with deteriorated out-of-band signal rejection, the location of out-of-band RZs can be optimized. Generally, the out-of-band rejection can be improved when the out-of-band RZs are farther from the adjacent TZs.

3) Once the polynomials of the dual/multiple dangling node are acquired, the input admittance is derived from the polynomials using (3.7).
4) The circuit elements can be directly extracted form Step 3 using (3.8) to (3.12). Finally, the coupling matrix can be constructed.

3.3.2 Coupling matrix synthesis of the filters

As explained Section 3.3.1, a multiple-dangling node generates out-band RZs in addition to in-band RZs and TZs. The out-band RZs have real parts, whose value are correlated with the value of imaginary parts, i.e., it's not possible to change the value of the real parts while the imaginary part is fixed. The frequency of these out-of-band RZs is not unique. Hence, there is no unique synthesisable frequency response for a filter with dual/multiple dangling nodes. Therefore, a direct synthesis method is not feasible to synthesise such filters and one needs to assume an initial frequency for the out-band RZs and obtain the corresponding real part using either iterative method [17] or step-tunning method [20],[21]. Assuming, the dangling node analytically characterised as discussed in Section 3.3.1, we have adopted the step-tuning method to obtain the coupling matrix of filters. This is not a direct synthesis method but a practical one with good usability. In this method, the filter topology is divided into several subsections. For each subsection, an initial coupling submatrix is estimated. In our cases, the subsections are either dual/multiple dangling nodes or single resonators. To start with, an auxiliary filter, of the same order (number of in-band RZs) and return loss but without any TZs, is first defined. Its coupling matrix can be obtained using the method in [1]. The auxiliary filter, together with its coupling matrix, is also divided into several subsections and submatrices. For the main filter, the coupling submatrix of the dual/multiple dangling nodes is obtained using the method explained earlier in Section 3.3.1. It must be noted that the level of *RL* and ω_i defined in a way that the in-band S parameter of the subsection matches the corresponding coupling

matrix of the auxiliary subsection. The coupling submatrix of the single resonators can be obtained in the same manner. The polynomials can be obtained like the dangling nodes. The only difference is that the number of dangling nodes is considered zero during the synthesis. Then, (3.8) to (3.11) can be used to extract the coupling submatrix elements. Finally, the submatrices are stitched together to create the coupling matrix of the filter. The resultant coupling matrix response has a similar in-band behaviour as the auxiliary matrix response. Figure 3.4(a) shows a third-order filter with two dangling nodes attached to the resonator 1. The TZs are at 9.9 GHz and 10.1 GHz. The central frequency is 10 GHz with a bandwidth of 100 MHz. As discussed before, the dual dangling resonator is expected to have a pair of out-band RZs, one at a frequency close to but lower than the TZ at 9.875 GHz. Assume this RZ at 9.4 GHz. The other out-band RZ is at a frequency close to but higher than 10.125 GHz. Assume it at 10.6 GHz. In Figure 3.4(a), the three red boxes indicate the three subsections in step tuning. Figure 3.4(b) presents the auxiliary third-order filter, also divided to three subsections. Figure 3.4(c) - Figure 3.4(e) show the step-tuning process conducted on each subsection of the main filter. Figure 3.4(d) shows the obtained coupling submatrix for the second subsection is different from the corresponding auxiliary submatrix. The reason is that J_4 in Figure 3.4(a) is fixed to the value obtained after acquiring the coupling submatrix of the first subsection, whilst J_5 is also fixed after obtaining the submatrix of the third subsection. Therefore, there is no freedom in changing the external couplings of the second submatrix, hence the difference in the response shown in Figure 3.4(d). However, this does not affect the response of the filter coupling matrix after attaching all coupling submatrices together. Figure 3.4(f) shows the response of the main filter after attaching all subsections together. The initial response shows 3 dB return loss deviation from the specified value. This can be fixed by a quick optimization. It is worth reiterating that the response of the filter, especially outside the passband, is not unique and can be adjusted by changing the location of the out-of-band RZs. Figure 3.4(g) shows the variation with different out-band RZs. The rejection level deteriorates if the out-band RZs are brought nearer to the TZs. The case with the highest out-of-band rejection is chosen for the design, whose coupling matrix is given in (3.14). Figure 3.4(h) compares the out-of-band rejection of two similar filters, in one of which the two TZs are generated using a dual-dangling node, whilst in the second filter, the TZs are generated using NRN method. It is shown that a dual-dangling node topology can achieve an improved level of out-of-band rejection compared

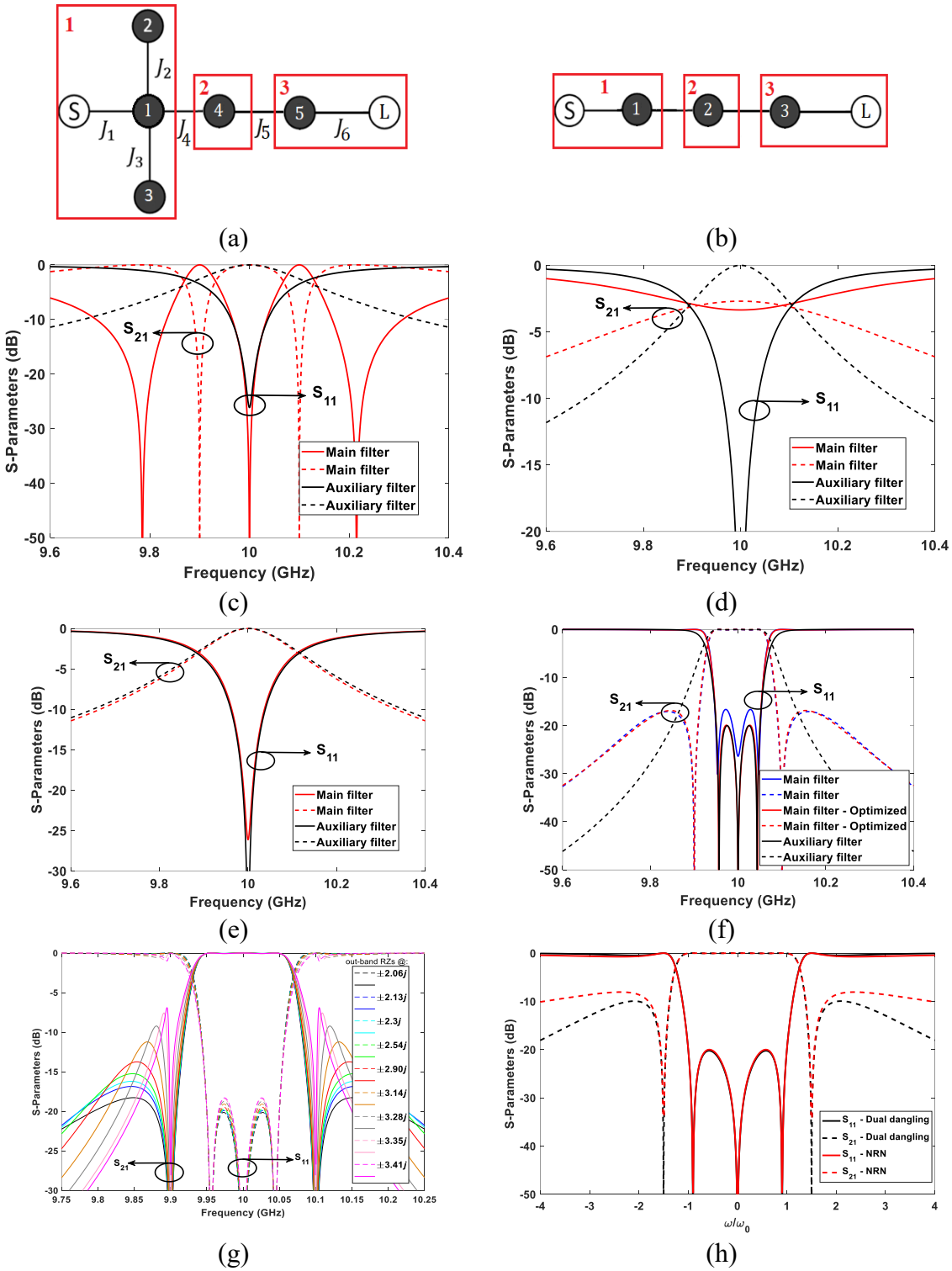

Figure 3.4 Step-tuning method for coupling matrix synthesis. (a) Topology of the main filter with a dual dangling node; (b) An auxiliary filter without any TZs; (c) – (e) Step-tuning method applied to the first, second and third subsection; (f) The result obtained from attaching all submatrices together; (g) Parameter sweep over the location of out-band RZs. (h) Similar filter with TZs closer to the passband compared with NRN method.

with the NRN method. The rejection improvement is more pronounced when the TZs are closer to the passband.

$$\begin{bmatrix} 0 & 2.4717 & 0 & 0 & 0 & 0 & 0 \\ 2.4717 & 0 & 2.6921 & 2.6921 & 2.4717 & 0 & 0 \\ 0 & 2.6921 & 2 & 0 & 0 & 0 & 0 \\ 0 & 2.6921 & 0 & -2 & 0 & 0 & 0 \\ 0 & 2.4717 & 0 & 0 & 0 & 1.0037 & 0 \\ 0 & 0 & 0 & 0 & 1.0037 & 0 & 1.0531 \\ 0 & 0 & 0 & 0 & 0 & 1.0531 & 0 \end{bmatrix} \quad (3.14)$$

3.4 EM design examples

The third-order filter with two TZs (the 3-2 filter in Section 3.3.2) is first designed. A step-tuning method is used again in the dimensioning of the filter. It starts with dividing the filter's topology to several subsections, whose corresponding coupling matrices are extracted from (3.14) in Section 3.3.2 as shown in Figure 3.5. For the EM model, each subsection is optimized until its S parameters fit to those from the corresponding coupling submatrix. It must be noted that, in each subsection, one or two internal couplings are converted to external couplings. For example, in the case of Figure 3.5(b), the internal couplings J_4 and J_5 in Figure 3.4(a) are converted to the external coupling J_4' and J_5' using (3.15):

$$J_i' = J_i \times \sqrt{FBW \frac{\pi}{2} \left(\frac{\lambda_g}{\lambda}\right)^2} \quad (3.15)$$

where J_i' represents the external coupling of the submatrix, J_i is the internal coupling of the coupling matrix, λ and λ_g are the free-space and guided wavelength, respectively. The diagonal elements of submatrix, representing the self-coupling of either the resonators or ports are also adjusted. For example, in the case of Figure 3.5(b), the diagonal elements corresponding to source and load are set to zero. Similar process is applied to other subsections. Once each subsection has been designed, they are joined together and optimized. Figure 3.6(a) shows the filter with 1% FBW in an H-plane configuration, using WR90 waveguide (width: 22.86 mm, height: 10.16 mm). The dominant mode is TE101. Figure 3.6(b) shows the simulated response after optimization. It agrees with the response from the coupling matrix very well. When the out-of-band RZs are located closer to the TZs, which are generated by multiple dual/multiple dangling nodes in the filter topology, more pronounced out-of-band spikes will appear, which deteriorates the rejection.

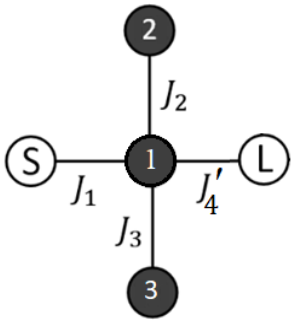

	S	1	2	3	L
S	0	2.4717	0	0	0
1	2.47	0	2.6921	2.6921	0.3912
2	0	2.6921	2	0	0
3	0	2.6921	0	-2	0
L	0	0.3912	0	0	0

(a)

	S	4	L
S	0	0.3912	0
4	0.3912	0	0.1711
L	0	0.1711	0

(b)

	S	5	L
S	0	0. 1711	0
5	0. 1711	0	1.0825
L	0	1. 0825	0

(c)

Figure 3.5 Coupling sub-matrix for: (a) the first subsection including a dual dangling node. J_4 is changed to J_4' using (3.15). (b) the second subsection. (c) the last subsection.

This is demonstrated in Figure 3.7(a) and Figure 3.7(b) using an example of a 5% FBW filter with two out-of-band RZs close to the two TZs. One solution to improve the lower band rejection deterioration level is using a mixed E/H-plane design, with one of the dangling resonators attached on the E-plane as shown in Figure 3.7(c).

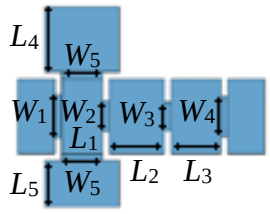

W_1=15.70 L_1=W_5
W_2=8 L_2=18.35
W_3=5.41 L_3=17.77
W_4=9.45 L_4=17.62
W_5=11.70 L_5=16.88

(a)

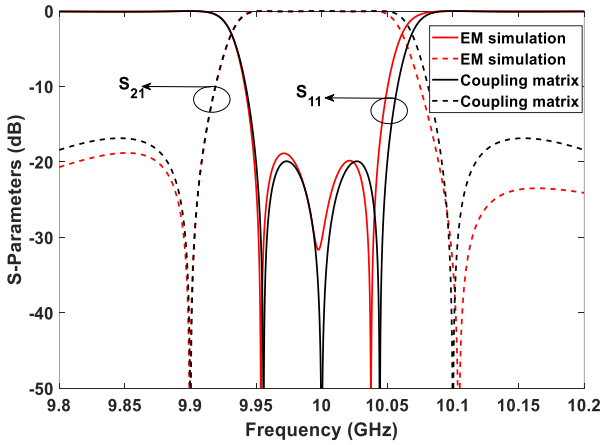

(b)

Figure 3.6 A 3-2 filter with H-plane dual dangling node. (a) Air model. All dimensions are in mm. (b) The EM simulation results compared those from the coupling matrix.

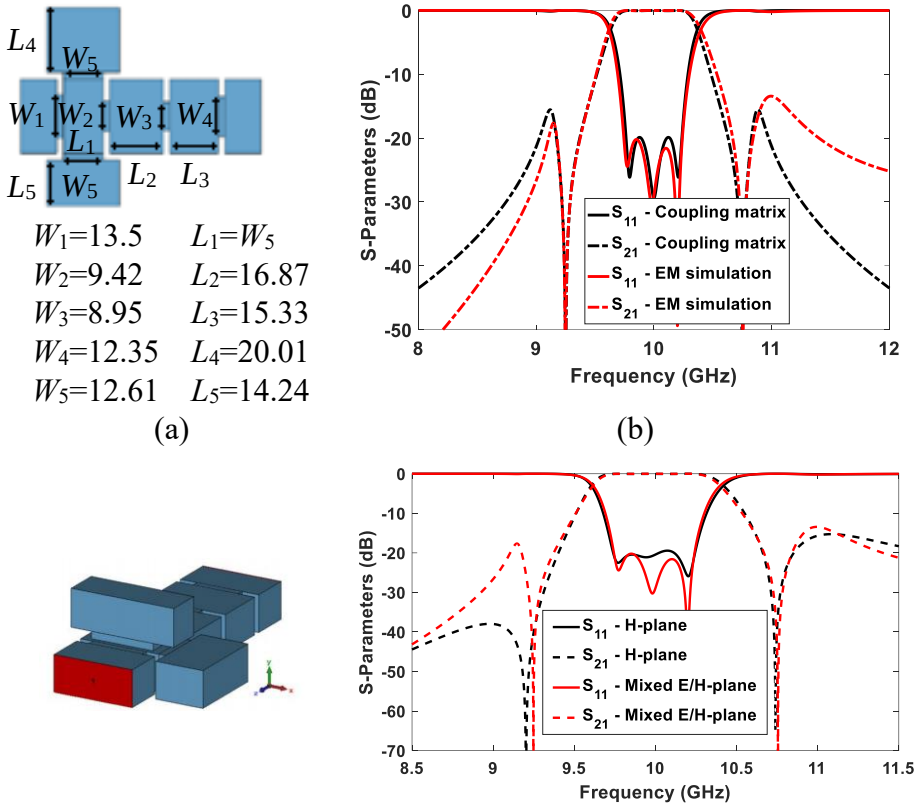

Figure 3.7 (a) An H-plane 3-2 filter with the out-band RZs near TZs. (b) H-plane filter response. (c) 3-2 filter with mixed H/E plane dangling resonators. (d) Comparison of EM simulation results between this modified filter and (a).

One solution to improve the lower band rejection deterioration level is using a mixed E/H-plane design, with one of the dangling resonators attached on the E-plane as shown in Figure 3.7(c). In Figure 3.7(d), the response of this modified filter is compared with the corresponding H-plane structure (Figure 3.7(a)). The improvement of the lower-band rejection is evident, as a result of the enhanced isolation between the two dangling nodes because of their different polarizations.

3.5 Results and discussions

In this section, a third-order filter with four TZs (the 3-4 filter) is synthesized, designed, and prototyped using the proposed method. The specification of the filter is as follows:

- f_c = 10 GHz with a 5% FBW
- Return loss, RL = 20 dB
- TZs @ 9.0 GHz, 9.25 GHz, 10.75 GHz and 11 GHz.

Figure 3.8(a) shows the topology of the filter. Its coupling matrix is given in (3.16) and is divided to three subsections, as shown in Figure 3.8(b). The corresponding submatrices are obtained using the step-tuning method, as presented in Figure 3.8(c).

$$\begin{bmatrix} 0 & 1.25 & 0 & 0 & 0 & 0 & 0 & 0 & 0 \\ 1.25 & 0 & 1.27 & 1.27 & 1.15 & 0 & 0 & 0 & 0 \\ 0 & 1.27 & 3 & 0 & 0 & 0 & 0 & 0 & 0 \\ 0 & 1.27 & 0 & -3 & 0 & 0 & 0 & 0 & 0 \\ 0 & 1.15 & 0 & 0 & 0 & 1.13 & 0 & 0 & 0 \\ 0 & 0 & 0 & 0 & 1.13 & 0 & 1.46 & 1.46 & 1.19 \\ 0 & 0 & 0 & 0 & 0 & 1.46 & 4 & 0 & 0 \\ 0 & 0 & 0 & 0 & 0 & 1.46 & 0 & -4 & 0 \\ 0 & 0 & 0 & 0 & 0 & 1.19 & 0 & 0 & 0 \end{bmatrix} \tag{3.16}$$

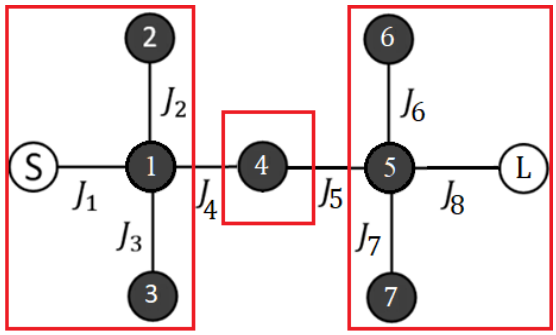

(a)

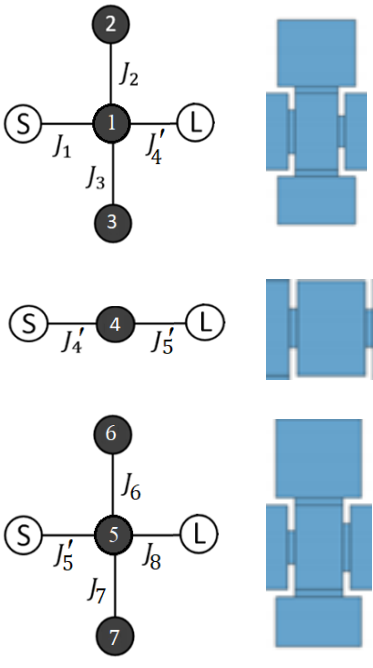

(b)

	S	1	2	3	L
S	0	1.25	0	0	0
1	1.25	0	1.27	1.27	0.43
2	0	1.27	-3	0	0
3	0	1.27	0	3	0
L	0	0.43	0	0	0

	S	4	L
S	0	0.43	0
4	0.43	0	0.42
L	0	0.42	0

	S	5	6	7	L
S	0	0.42	0	0	0
5	0.42	0	1.46	1.46	1.19
6	0	1.46	-4	0	0
7	0	1.46	0	4	0
L	0	1.19	0	0	0

(c)

Figure 3.8 (a) Topology of the 3-4 filter. (b) Topology and air model of the subsections. (c) Coupling sub-matrices.

We have found it is desirable to dedicate each dual dangling resonator to two TZs from either side of the passband. For instance, if resonator 2 in Figure 3.8(a) corresponds to a lower-band TZ, the resonator 3 should be assigned to a higher-band TZ. Otherwise, some sharp out-of-band spikes will appear. Figure 3.9(a) compares the two scenarios when each dual dangling node is assigned to produce two TZs either at the same side or at both sides of the passband. In Scenario 1, there is always one out-of-band RZ trapped in between each pair of TZs on one side of the passband. This leads to sharp out-of-band spikes. Figure 3.9(b) shows the variation of the out-of-band responses with the changing location of the out-of-band RZs. This filter can be also realized using a single quad-dangling node as displayed in Figure 3.10(a).

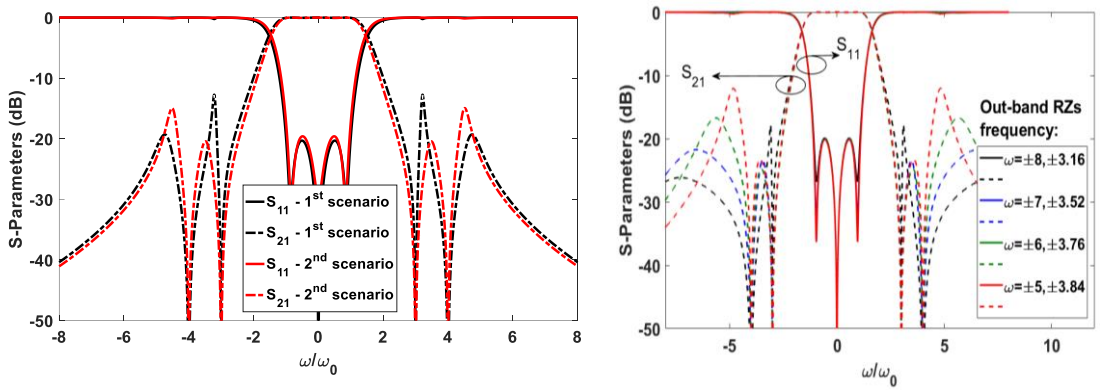

(a) (b)

Figure 3.9 (a) Comparison of coupling matrix responses of two 3-4 filters with different TZs formation scenario. 1st scenario: Each dual dangling node produces a pair of TZs on one side of the passband; 2nd scenario: Each dual dangling node produces two TZs on either side of the passband. (b) Variation of out-and responses with different out-band RZs locations.

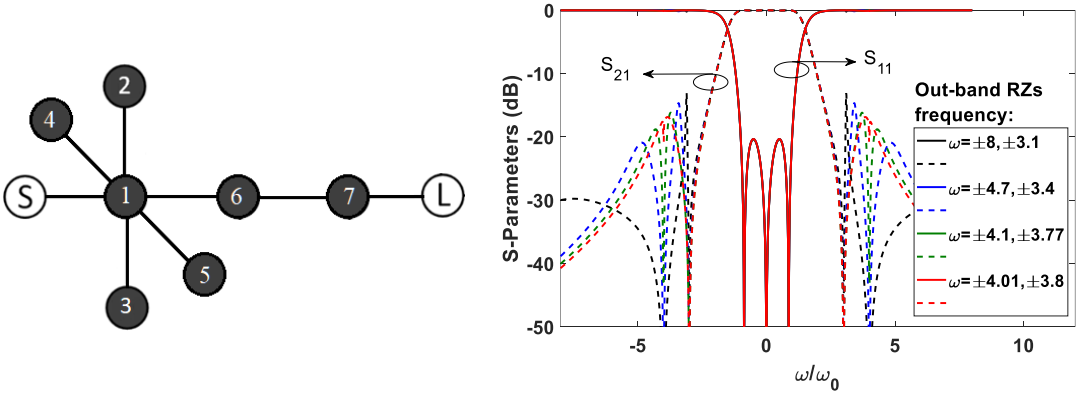

(a) (b)

Figure 3.10 (a) Topology of the 3-4 filter with a quad dangling node. (b) Variation of the out-band responses with changing locations of the RZs.

It is synthesized using the same method. Figure 3.10(b) shows the variation of the out-of-band with the locations of the out-of-band RZs. The rejection next to the passband edges when a quad-dangling node is used in Figure 10(b) is worsen compared with Figure 3.9(b), in which two dual-dangling nodes are used to generate the TZs. Hence, we have chosen the dual dangling node for experimental verification. For the EM dimensioning, each subsection is designed separately. Once all subsections are attached to each other, a final optimization is performed. The designed H-plane filter is presented in Figure 3.11(a). The optimized S parameters and those from the coupling matrix are compared in Figure 3.11(b). The small discrepancy is mainly due to the estimation of the out-of-band RZs location and the cut-off frequency of the waveguide.

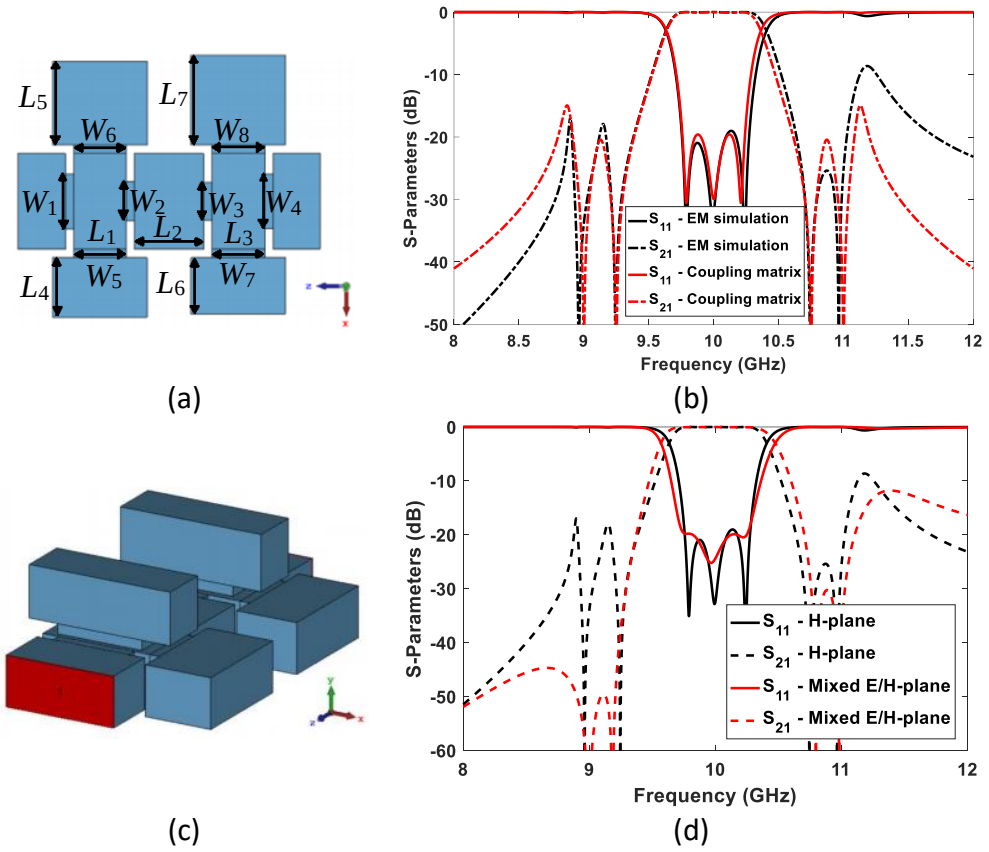

Figure 3.11 Realization of the 3-4 filters (BW = 500 MHz). (a) Filter with H-plane dual dangling nodes. The dimensions of the filter are in mm: W_1=13.21, W_2=9.35, W_3=9.12, W_4=12.92, W_5=W_6=12.66, W_7= W_8=12.82, L_1=W_5, L_2=12.77, L_3= W_7, L_4=12.24, L_5=20.00, L_6=13.50, L_7=21.50. (b) The EM simulation results for (a) compared with those from coupling matrix. (c) Filter with mixed H/E-plane dual dangling nodes. (d) The EM simulation results of Figure 3.10(c) compared with H-plane structure.

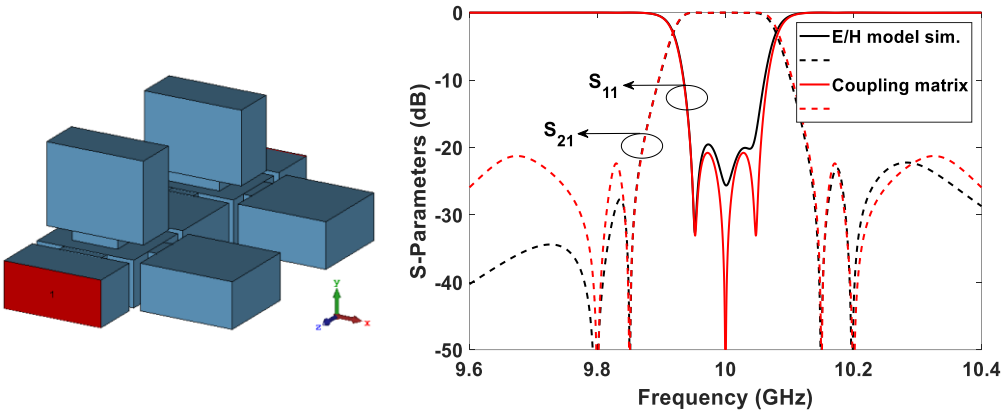

(a) (b)

Figure 3.12 (a) Filter with mixed E/H-plane configuration with similar specifications as the filter in Figure 3.12 but a BW of 100 MHz). The dimensions (in mm) of the filter, in accord with Figure 3.12(a), are: W_1=10.06, W_2=5.76, W_3=8.5, W_4=12.2, W_5=10.6, W_6=6.5, W_7=6.16, W_8=12.6, L_1=17.95, L_2=18.73, L_3= 16.47, L_4=17.88, L_5=21.69, L_6=16.14, L_7=20.7. (b) The EM simulation results compared with the coupling matrix.

Figure 3.11(b) shows some sharp out-of-band spikes, which are undesirable. Significant improvement on the low band rejection can be seen once a mixed H/E plane configuration for the dangling nodes are used, as shown in Figure 3.11(c) and Figure 3.11(d). As another example, a similar filter topology but a 1% FBW is designed using the mixed E/H plane configuration. Figure 3.12 shows the filter and its EM simulation result, compared with that from the coupling matrix. The mixed E/H plane configuration would complicate the fabrication using conventional machining technique and require more than one pair of split blocks. However, by using 3D printing technique, the filter can be formed out of a monolithic block. The first example filter in Figure 3.11(c) is printed using the selective laser melting (SLM) technique with an aluminium-copper alloy (A20X) powder. The thickness of the structure wall and the iris is set to 2 mm. It is important to optimize the printing direction to avoid the internal overhangs and minimize the requirement for external support. Figure 3.13(a) shows the printing direction of the device with a 45° tilt. After printing, the unsintered powder is cleared out. Polishing is a very important stage. Based on our experience, mechanical polishing using a vibratory grinding machine is suitable for the X-band designs in this work. An image of the printed structure after polishing is presented in Figure 3.13(b). The S parameter of the filter has been measured and compared with the simulation in Figure 3.13(c). Excellent agreement can be observed without any tuning. The measurements show that the frequency of the TZs is slightly shifted by 30-50 MHz towards the central frequency. The bandwidth is reduced by 40

MHz compared to the simulation. There is no notable frequency shift observed for the central frequency. All TZs are reproduced. The measured insertion loss is 0.18 dB, which is 0.052 dB higher than the simulation result. The measured typical surface roughness and nominal electrical conductivity of A20X are around 3.5 μm and 1.9×10^7 S/m, respectively. These factors are used to obtain the material's effective conductivity [22], which is around 5.6×10^6 S/m and used in the simulations. The results have verified the prototype design and the proposed synthesis and design method. It also demonstrated the capability of 3D printing in producing complex structures monolithically, which is difficult or even impossible for conventional fabrication technologies such as CNC machining.

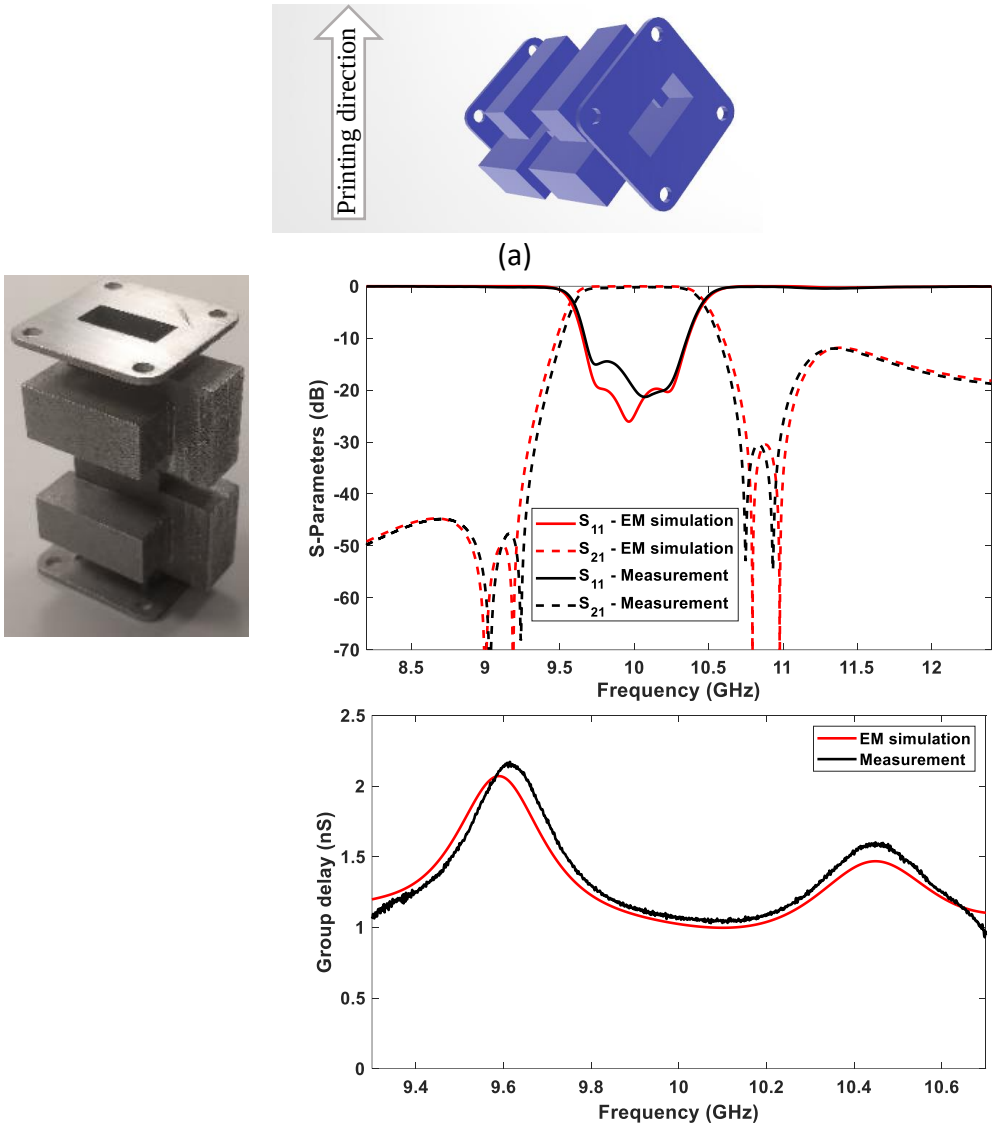

Figure 3.13 (a) Printing direction of the 3-4 filter. (b) Photo of the 3D printed 3-4 filter. (c) Measurement results in comparison with EM simulation.

3.6 Conclusion

In this paper, a method for the synthesis and design of filters with multiple TZs using dual/multiple dangling node topologies is proposed and verified experimentally. It addresses how a dual/multiple dangling resonator creates out-of-band RZs and how to synthesize the characteristic polynomials and the coupling matrix, dealing with RZs with a real part. The method is implemented and demonstrated on waveguide cavity resonator filters. The dual/multiple dangling node topologies shows out-of-band signal rejection deterioration due to the real part of the out-of-band RZs. This can be partly mitigated by optimizing the location of the RZs and partly by electromagnetic design using a mixed E/H plane dangling structure. Two third-order filters with four TZs are designed and prototyped. The dual dangling node structure presents the challenge in fabrication. This has been overcome by using 3D-printing technology. The work demonstrated this novel filter structure, which can be used to generate more TZs than conventional topology allows. It is also another example of applying additive manufacture technology to explore new possibility of filter topology and design flexibility.

3.7 Appendix

As mentioned in Section 3.3.1, the common node in a multiple-dangling node is treated as a resonator rather than an NRN. In this section, the EM simulation results are used to verifies the assumption as well as the synthesis process. Figure A1(a) shows a dual-dangling node discussed in Section 3.3.1 and its equivalent circuit model. Here, we use this topology to continue the assumption verification process. As explained in Section 3.3.1, the input admittance of the circuit model of the dual-dangling node can be written as follows:

$$Y_{in} = \frac{1 - S_{11}}{1 + S_{11}} = \frac{N(s)}{D(s)} = \frac{\varepsilon_R E(s) - F(s)}{\varepsilon_R E(s) + F(s)} =$$

$$\frac{J_1^2[s^2 + j(b_2 + b_3)s - b_2 b_3]}{s^3 + [J_4^2 + jB_R + jB_2 + jB_3]s^2 + [j(J_4^2 + jB_R)(b_2 + b_3) + J_2^2 + J_3^2 - b_2 b_3]s + C} \quad \text{(A1)}$$

where C is

$$C = (J_4^2 + jB_R)(-b_2 b_3) + jJ_2^2 b_3 + jJ_3^2 b_2 \quad \text{(A2)}$$

From (A1), $D(s)$ is a third-order polynomial. By writing the relation between S_{11} and Y_{in}, it can be found that the numerator of S_{11}, $N(s)+D(s)$, is also a third-order polynomial, with three roots

corresponding to the three RZs corresponding to the three resonators in Figure A1(a). Typically, the arrangement of these three RZs is as one RZ in-band and two out-of-band, as shown in Figure A1(b). The lower out-of-band RZ is located at a frequency lower than the left TZ and the upper out-of-band RZ is located higher than the right TZ. In order to prove this claim, the number of critical points, at which the derivative of S_{11} is zero or infinite, will be obtained. The derivative as a function of $N(s)$, $D(s)$, $N(s)'$ and $D(s)'$ can be written as:

$$S'_{11} = \left(\frac{1-y_{in}}{1+y_{in}}\right)' = \frac{(D'-N')(N+D)-(D-N)(N'+D')}{(N+D)^2} \tag{A3}$$

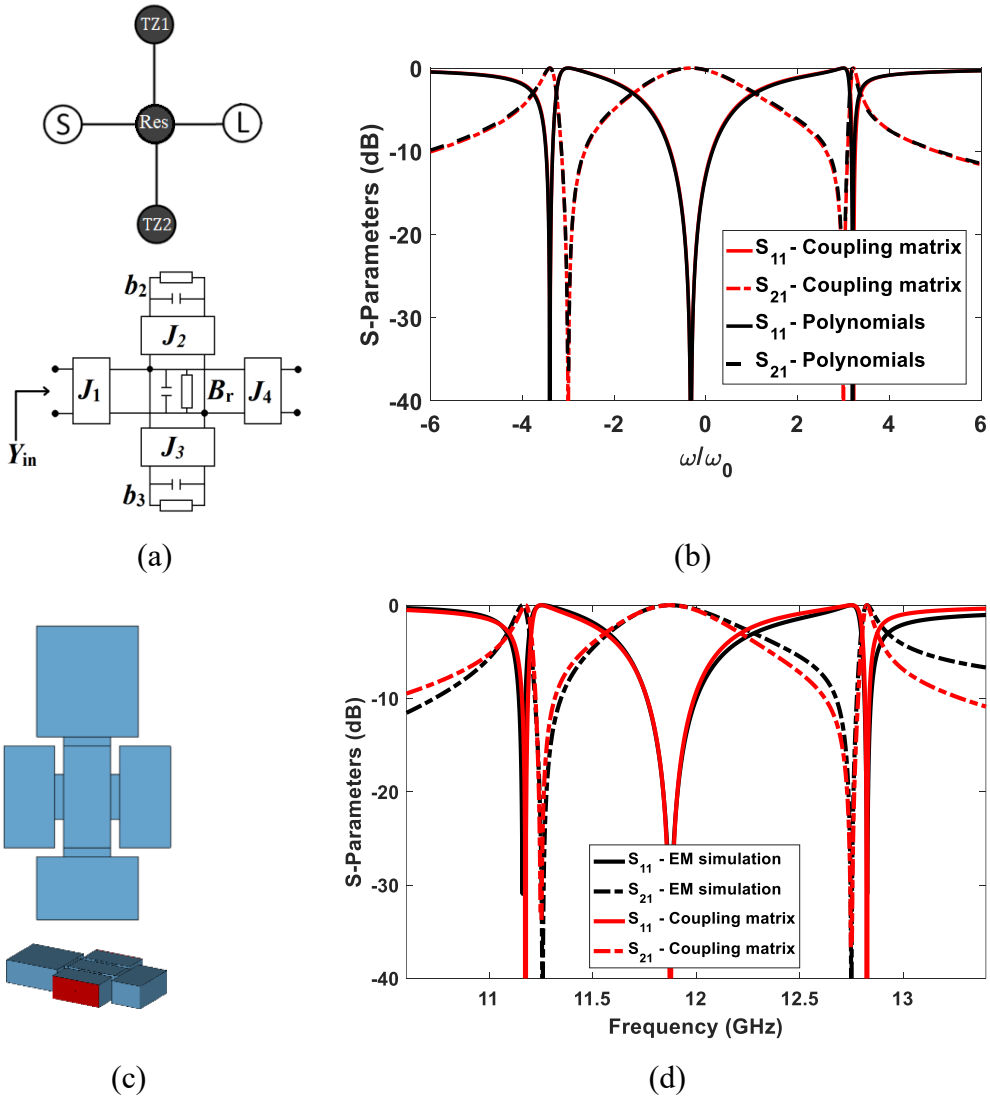

Figure A1 (a) Topology of a dual dangling node. (b) Equivalent circuit model. (c) Air model of a dual dangling node resonator in WR90 waveguide. (d) Simulated responses compared with those from the coupling matrix in (A4).

Table A1 Coefficients of characteristic polynomials for the topology in Figure A1.

n	P(ω)	F(ω)	E(ω)
0	9	3.5360j	15.3585+3.5360j
1	0	10.8150	10.8150
2	1	0.5250j	1.7065+0.5250j
3	0	1	1
$\varepsilon_R = 1$		$\varepsilon = 0.5860$	

where *N'* and *D'* represent the derivative of *N*(*s*) and *D*(*s*) with respect to *s*, respectively. As mentioned earlier, the term $N \pm D$ is a cubic polynomial. Consequently, the term $N' \pm D'$ is a second-order polynomial. As a result, the numerator of (A3) is a fifth-order polynomial, whilst the denominator is a sixth-order polynomial. Since the denominator is a linear polynomial, it cannot be infinite except for $s=\pm\infty$, where the derivative of S_{11} tend to be zero. Therefore, the only finite critical points of (A3) are derived from the zeros of its numerator. These are the five roots. From Figure A1(b), these five points correspond to the two TZs and the three RZs. The out-of-band RZs cannot be between the TZs. Otherwise, S_{11} would have had seven finite critical points. Let's assume the dual dangling node generates three RZs at ω=-3.4j, ω=3.2j and ω=-0.325j. The two dangling nodes, i.e., TZ_1 and TZ_2, provide two TZs at ω=3j and ω=-3j. It's worth mentioning that the number of dangling nodes (TZs) could be arbitrary in theory. Here, we consider two dangling nodes for clarity without losing generality. The characteristic polynomials of the dual dangling node are obtained using the method discussed in Section 3.3.1. The coefficients of the polynomials are given in Table A1. The corresponding S parameters are plotted in Figure A1(b) using the obtained characteristic polynomials. The input admittance can be expressed using the following equation.

$$Y_{in} = \frac{1 - S_{11}}{1 + S_{11}} = \frac{\varepsilon_R E(s) - F(s)}{\varepsilon_R E(s) + F(s)}$$

$$= \frac{14.33\times(s^2+16)}{s^3+(14.33-0.8j)s^2+25s+229.25-20j} \quad \text{(A4)}$$

By comparing (A4) and (A1), the value of b_2, b_3, B_R, J_1, J_2, J_3 and J_4 can be found. This leads to the expressions (11) to (15) in Section 3.3.1. These circuit elements create the coupling matrix of the dual-dangling node as follows:

$$M = \begin{bmatrix} 0 & J_1 & 0 & 0 & 0 \\ J_1 & B_R & J_2 & J_3 & J_4 \\ 0 & J_2 & b_2 & 0 & 0 \\ 0 & J_3 & 0 & b_3 & 0 \\ 0 & J_4 & 0 & 0 & 0 \end{bmatrix}$$

$$= \begin{bmatrix} 0 & 0.9129 & 0 & 0 & 0 \\ 0.9129 & -0.5 & 1.0499 & 0.8873 & 0.9129 \\ 0 & 1.0499 & 3 & 0 & 0 \\ 0 & 0.8873 & 0 & -3 & 0 \\ 0 & 0.9129 & 0 & 0 & 0 \end{bmatrix} \quad \text{(A4)}$$

The corresponding S parameters, derived from the coupling matrix in (A4), match those from the polynomials as shown in Figure A1(b). Physically, this dual dangling node can be implemented as shown in Figure A1(c) using rectangular waveguides. The structure is designed based on WR90 waveguide in CST and the EM simulation results are presented in Figure A1(d). The simulation result clearly depicts the three RZs and two TZs. The results from the simulation and the coupling matrix match excellently, especially in terms of the location of the poles and TZs. This verifies the assumption of the resonant common node. In other words, the two dangling nodes generate two out-of-band RZs, while the common node produces one in-band RZ.

References

[1] R. J. Cameron, C. Kudsia and E. Mansour, "*Microwave filters for communication systems*," 2nd ed., Hoboken, USA: J. Wiley., 2018, pp. 323–335.

[2] S. Amari and G. Macchiarella, "Synthesis of inline filters with arbitrarily placed attenuation poles by using nonresonating nodes," *IEEE Transactions on Microwave Theory and Techniques,* vol. 53, no. 10, pp. 3075-3081, Oct. 2005.

[3] Y. Yang, M. Yu and Q. Wu, "Advanced Synthesis Technique for Unified Extracted Pole Filters," *IEEE Transactions on Microwave Theory and Techniques*, vol. 64, no. 12, pp. 4463-4472, Dec. 2016.

[4] Y. Yang, M. Yu, Q. Wu, X. Yin and J. Yang, "A Fully Integrated Multiplexer Using Unified Extracted Pole Technique," *IEEE Transactions on Microwave Theory and Techniques,* vol. 68, no. 8, pp. 3439-3447, Aug. 2020.

[5] A. Mostaani, Y. Wang, L. Qian, A. E. -M. A. Mohamed, M. M. Attallah and T. Skaik, “Compact Self-Supportive Filters Suitable for Additive Manufacturing,” *IEEE Transactions on Components, Packaging and Manufacturing Technology*, vol. 13, no. 12, pp. 1966-1972, Dec. 2023.

[6] W. J. Feng, W. Q. Che, Y. M. Chang, S. Y. Shi and Q. Xue, “High Selectivity Fifth-Order Wideband Bandpass Filters With Multiple TZs Based on Transversal Signal-Interaction Concepts,” *IEEE Transactions on Microwave Theory and Techniques*, vol. 61, no. 1, pp. 89-97, Jan. 2013.

[7] W. J. Feng, X. Gao, and W. Che, “Bandpass filters with multiple transmission zeros using open/shorted stubs,” *IET Microwaves, Antennas & Propagation*, 9: 769-774. 2015.

[8] D. Psychogiou and R. G.-García, “Reflectionless Adaptive RF Filters: Bandpass, Bandstop, and Cascade Designs,” *IEEE Transactions on Microwave Theory and Techniques*, vol. 65, no. 11, pp. 4593-4605, Nov. 2017.

[9] D. -J. Kim and J. -H. Lee, “Partial H-Plane Filters With Multiple Transmission Zeros,” *IEEE Transactions on Microwave Theory and Techniques*, vol. 56, no. 7, pp. 1693-1698, July 2008.

[10] D. J. Simpson, R. .-García and D. Psychogiou, “Tunable Multiband Bandpass-to-Bandstop RF Filters,” *2018 IEEE/MTT-S International Microwave Symposium - IMS*, 2018, pp. 1363-1366.

[11] D. Psychogiou, R. G.-García and D. Peroulis, “Fully-Reconfigurable Bandpass/Bandstop Filters and Their Coupling-Matrix Representation,” *IEEE Microwave and Wireless Components Letters*, vol. 26, no. 1, pp. 22-24, Jan. 2016.

[12] D. J. Simpson, R. Gómez-García and D. Psychogiou, "Single-/Multi-Band Bandpass Filters and Duplexers With Fully Reconfigurable Transfer-Function Characteristics," *IEEE Transactions on Microwave Theory and Techniques*, vol. 67, no. 5, pp. 1854-1869, May 2019.

[13] R. G.-Garcia and J. I. Alonso, “Design of sharp-rejection and low-loss wide-band planar filters using signal-interference techniques,” *IEEE Microwave and Wireless Components Letters*, vol. 15, no. 8, pp. 530-532, Aug. 2005.

[14] Q. Xue and J. Y. Jin, “Bandpass Filters Designed by TZ Resonator Pairs With Proximity Coupling,” *IEEE Transactions on Microwave Theory and Techniques*, vol. 65, no. 11, pp. 4103-4110, Nov. 2017.

[15] K. D. Xu, F. Zhang, Y. Liu and Q. H. Liu, “Bandpass Filter Using Three Pairs of Coupled Lines With Multiple TZs,” *IEEE Microwave and Wireless Components Letters*, vol. 28, no. 7, pp. 576-578, July 2018.

[16] D. Miek, P. Boe, F. Kamrath and M. Höft, “Techniques for the generation of multiple additional transmission zeros in H-plane waveguide filters” *2020 International Journal of Microwave and Wireless Technologies*, 12(8), pp.723-732.

[17] S. Tamiazzo, G. Macchiarella and F. Seyfert, “Path Filters: A Class of True Inline Topologies With Transmission Zeros,” *IEEE Transactions on Microwave Theory and Techniques*, vol. 70, no. 1, pp. 850-863, Jan. 2022.

[18] Y. Zeng, Y. Yang, Y. Wu, M. Yu, J. Peng and D. Liang, “Exploiting Redundancy in Direct Synthesis for Inline Filters,” *IEEE Transactions on Microwave Theory and Techniques*, vol. 69, no. 10, pp. 4489-4498, Oct. 2021.

[19] J. -Y. Lin, S. -W. Wong, L. Qian, Y. Wang, Y. Yang and Q. -H. Liu, “Single and Multiple-Band Bandpass Filters Using Bandstop Resonator Sections,” *IEEE Journal of Microwaves*.

[20] A. Mostaani, L. Qian, R. Martinez, P. F. Wilson, M. Attallah, Y, Wang, M. A. Williams, “Investigation of a 3D-Printed Narrowband Filter with Non-Resonating Nodes,” *2021 IEEE MTT-S International Microwave Filter Workshop (IMFW)*, 2021, pp. 316-318.

[21] X. Shang, W. Xia, and M. J. Lancaster, “The design of waveguide filters based on cross-coupled resonators,” *Microwave and Optical Technology Letters*, vol. 56, no. 1, pp. 3–8, 2014.

[22] E. Hammerstad and O. Jensen, “Accurate Models for Microstrip Computer-Aided Design,” *1980 IEEE MTT-S International Microwave symposium Digest*, Washington, DC, USA, 1980, pp. 407-409.

CHAPTER 4

SYNTHESIS OF ALL-RESONATOR MULTIPLEXERS

Paper accepted

Abolfazl Mostaani*, Talal Skaik*, Yi Wang*

MTT-S International Microwave Filter Workshop (IMFW), California, USA, Feb 2024.

Extended paper in submission

Abolfazl Mostaani*, Talal Skaik*, Yi Wang*

IEEE Journal of Microwave

A. Mostaani proposed the method and wrote the manuscript in collaboration with Y. Wang and T. Skaik, who assisted in the matrix optimisation.

* School of Engineering University of Birmingham, Birmingham, U.K.

4.1 Introduction

Multiplexer, one of the most complex passive circuits, is critical part of many telecommunications systems, where multiple radio frequency (RF) signals need to be combined or a single signal needs to be divided into multiple channels, with different frequency ranges. Multiplexers are generally formed of multiple RF filters that can be combined using different configurations. The most common is the manifold structure that uses T-junctions [1]-[4]. Circulator-coupled [5]-[7], hybrid-coupled [8], and star junction multiplexers [9]-[11] are other three available configurations. The advantage of such topologies is their ability to design the channel filters separately then combine them by a signal distribution network. However, the signal distribution elements increase the volume of the multiplexer without adding much to the selectivity of the multiplexers. Another multiplexer configuration based on all-resonator structures is also reported in literature [12]-[17]. It is a more compact topology where all resonators including those for signal distribution contribute to the selectivity of the network. The all-resonator topologies offer more flexibility in resonators' arrangement and can induce signal cancellation at particular frequencies and thus generating transmission zeros (TZ) that enhance the selectivity [15],[17]. However, the all-resonator topologies are hard to synthesize especially for those with a large number of resonators. In fact, all the previously reported resonator-based multiplexers were synthesized by coupling matrix optimization. This usually relies on good initial values of the coupling coefficients to ensure the convergence of the subsequent optimization. This usually needs heavy computations, which could last for hours for complicated topologies. Therefore, this solution is often infeasible for multiplexers with a large number of resonators since the optimization algorithm may not converge. In [15] and [17], an optimization-based method is proposed for the synthesis of all-resonator multiplexers. The methods can take up to 20 to 30 minutes to converge, if a good initial point is provided. In [18], a synthesis method for coupling matrix using direct equations was reported for diplexers with T-junction topologies only. However, the method was not generalized to all-resonator multiplexer topologies.

In this chapter, a new iterative synthesis process is proposed for generating a strong initial coupling matrix for all-resonator multiplexers. This renders fast optimization of the final coupling matrix even for a large number of resonators. The process is derived from the characteristic polynomials of each channel filter together with an estimation of the loading

effect from other channels. The input admittance of each channel is obtained using the polynomials. The equivalent circuit elements of the corresponding channel are extracted from the input admittance in order to obtain the initial elements of the coupling matrix. Finally, the coupling matrix is optimized. The typical process lasts for less than 20 iterations, unless the topology is really complicated, or the channels are very close to each other. The optimization generally requires less than 30 seconds even using a low-end PC. In case of diplexers, the iterative process usually converges within 10 iterations and the optimization lasts less than 5 seconds regardless of the complexity level of the diplexer. Examples are provided in this chapters to verify the method.

4.2 Polynomial synthesis

Figure 4.1 depicts a general architecture of an all-resonator multiplexer, for which the following characterization parameters are defined: channel number k; number of in-band reflection zeros (RZs) of k^{th} channel n_{ik}; number of out-of-band RZs n_{ok}; number of transmission zeros (TZs) n_{zk}; TZs' frequency f_{zk}; return loss level RL_k; central frequency f_{ck}; and passband edges f_{Lk} and f_{Rk}. The channel, whose one of nodes are directly attached to the source port, is called "main branch". All branches of the multiplexer can be connected to any nodes of the other branches as well as the main branch. The generated topology looks like a tree branches. For example, Figure 4.2(a) shows an all-resonator triplexer, whose three channels are distinguished by different colours, together with its S parameters displayed in Figure 4.2(d). Figure 4.2(b) and Figure 4.2(c) display the same triplexer but with two different channel arrangements. Their corresponding S parameters are presented in Figure 4.2(e) and Figure 4.2(f), respectively. Depending on the channel arrangement, TZs may be generated without adopting any additional TZ-generating features such as dangling nodes or cross couplings. It is important to understand how, where and when the TZs are generated in an all-resonator

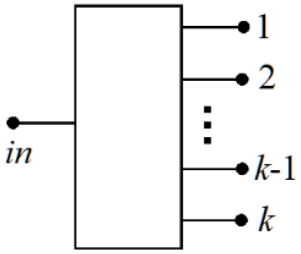

Figure 4.1 An all-resonator multiplexer with k channels.

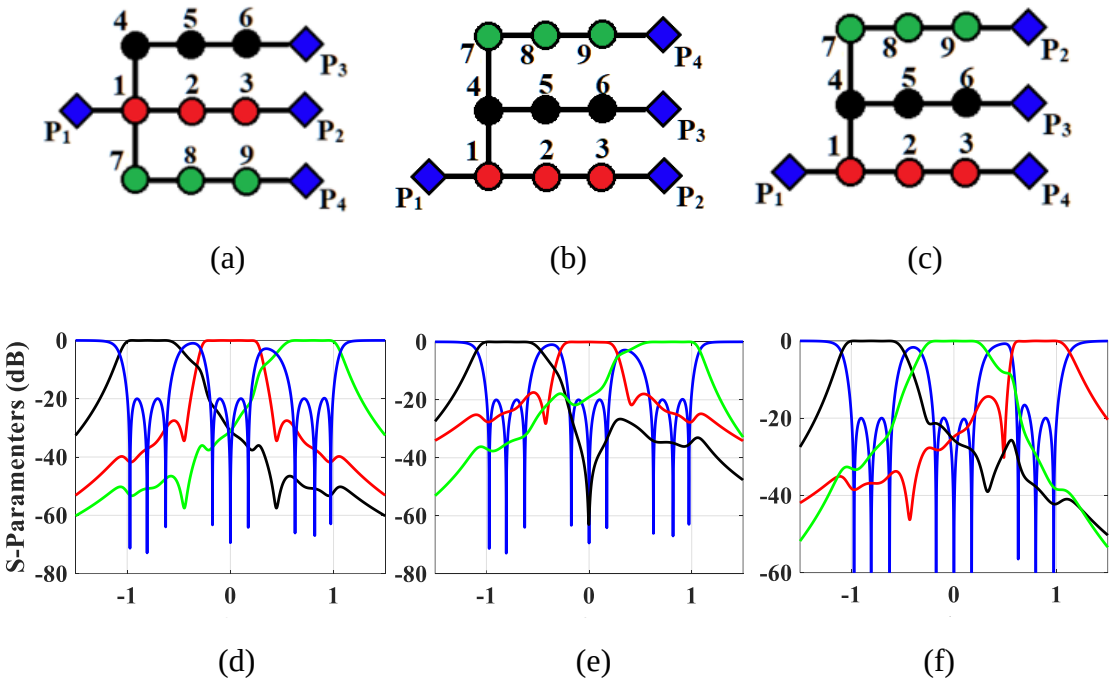

Figure 4.2 An all-resonator triplexer: (a), (b) and (c) represent a same triplexer with different channel arrangements and (d), (e) and (f) are the corresponding S parameters. Colour of nodes corresponds to the channel's colour in the graph.

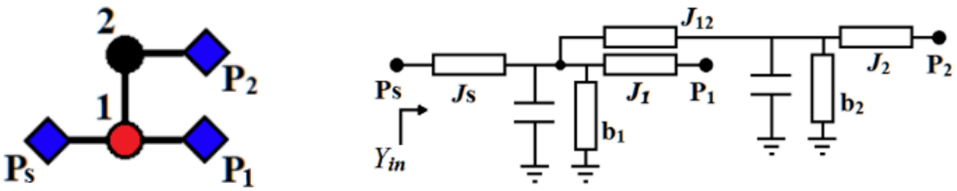

Figure 4.3 A diplexer with a single resonator in each channel: (a) The topology. (b) Equivalent circuit model.

topology, because they must be considered during the synthesis process. We start with looking at a core coupling structure in the all-resonator topology, a diplexer with only two resonating nodes, as shown in Figure 4.3, together with its equivalent circuit model. The *J* and *b* elements represent the *J*-inverters (i.e., cross-coupling values in the coupling matrix) and the susceptance (i.e., self-coupling values in the coupling matrix), respectively. The input admittance Y_{in}, while port 2 is short circuit (SC), is written as:

$$Y_{in1}(s) = Y_{in}|_{\text{port 2 is SC}} = \frac{J_S^2}{s+jb_1+\frac{J_{12}^2}{s+jb_2}+J_1^2} \tag{4.1}$$

Similarly, Y_{in}, while port 1 is SC, can be written as:

$$Y_{in2}(s) = Y_{in}|_{\text{port 1 is SC}} = \frac{J_S^2}{s+jb_2+s+jb_1+J_2^2} \tag{4.2}$$

Considering the relation between S_{21} and the channel's input admittance, Y_{in1}, it is clear that a TZ will be generated at the frequency of $-jb_2$, which is located between the two channels' central frequencies (in this example, the central frequency of each channel is equal to the resonant frequency of each resonating node). From (4.2), it is noted that Y_{in2} generates no TZ. In general, if any nodes of a multiplexer's channel are connected to another channel in parallel, a TZ will be generated at a frequency between the two channels. If the multiplexer is symmetric, the TZ is located almost in the middle between the two channels. For instance, in Figure 4.2(a), there are two TZs between the middle channel (at port 2) and the other two, since the topology is symmetric and channels 1 and 3 are connected to the middle channel in parallel. If the first node of the multiplexer's channel is cascaded to another channel, no TZ will be generated. Knowing the generated TZs, the synthesis process can be started by obtaining the in-band RZs of the multiplexer. To do so, based on the channel filter order and using the Chebyshev filter relation, the in-band RZs of each channel are defined. Then, the corresponding RZs of each channel will be mapped into the correct frequency defined by the channel specifications, i.e., central frequency (f_c) and bandwidth (BW). One channel of the multiplexer is selected to be synthesized. The loading effect of other channels are involved in the synthesis of the selected channel by considering the first node of other channels. According to the synthesis results obtained using MATLAB, an acceptable estimation of the loading effect on corresponding channels is achieved by considering only the first node of other channels. While it is conceivable to include the loading effect of all nodes from other channels, this would disproportionately escalate the complexity and time consumption of the process, offering no significant enhancement to the efficacy of the synthesis. The in-band RZs of the chosen channel are determined using the Chebyshev filter relation. For every node associated with other channels, if the node is cascaded with the selected channel, an out-of-band RZ is appended to the existing set of RZs. Conversely, if the node is in parallel with the selected channel, both a TZ and an out-of-band RZ are added to the available sets of RZs and TZs. The out-of-band RZ is approximated at the central frequency of its respective channel. It is worth noting that the

out-of-band RZs has a real part, as indicated in [19],[20], will be determined in subsequent iterations. The position of the TZ is estimated between the central frequency of the selected channel and the out-of-band RZ. With the frequencies of both RZ and TZ identified, the characteristic polynomials—$F(s)$, $P(s)$, and $E(s)$—for the selected channel can be constructed as follows:

$$F(s) = \prod_{i=1}^{N_k}(s - s_{ik}) \times \prod_{k=1}^{N_k^*-1}(s - s_{ok}) \tag{4.3}$$

where s is the complex frequency variable, related to the frequency variable ω by $s=j\omega$. N_k and S_{ik} are the filter order and the in-band RZs of the selected channel, respectively. N_k^* and S_{ok} are the number of the channels and the out-of-band RZs. $P(s)$ is created from the TZs of the selected channel and can be written as:

$$P(s) = \prod_{nz=1}^{Ntz}(s - s_{nz}) \tag{4.4}$$

where s_{nz} is the TZ frequency and Ntz is the number of TZs. Assuming a lossless network, we can write the unitary condition of the scattering matrix as:

$$E(s) \cdot E^*(-s) = \frac{1}{\varepsilon^2} P(s) \cdot P^*(-s) + F(s) \cdot F^*(-s) \tag{4.5}$$

where ε is given as:

$$\varepsilon = \frac{1}{\sqrt{10^{-RL_k/10}-1}} \cdot \frac{P(s)}{F(s)}\bigg|_{s=s_j} \tag{4.6}$$

in which RL_k is the selected channel's return loss in decibels. s_j refers to the frequency, at which the return loss is imposed to the prescribed RL. Figure 4.4 illustrates the assignment of the frequency s_j, which is marked by a circle for each channel. Utilizing the spectral factorization technique, the polynomial E can be derived from its roots as indicated in (4.5). Subsequently, the synthesis process proceeds by constructing the input admittance of the selected channel through its characteristic polynomials.

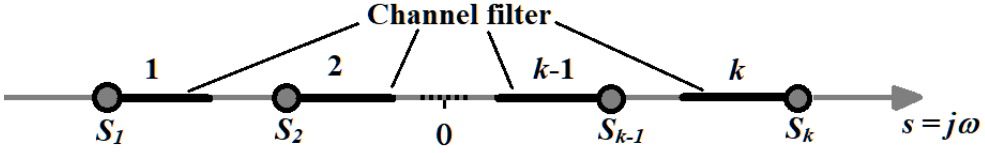

Figure 4.4 Location of frequency s_j, where the return loss RL_k is imposed.

It is assumed that the polynomials *P*, *F*, and *E* are normalized with respect to their highest degree coefficients.

$$Y_{in_k} = \frac{E(s)-F(s)}{E(s)+F(s)} = \frac{N(s)}{D(s)} \tag{4.7}$$

Having Yin_k, the synthesis of the selected channel involves extracting the circuit model elements from (4.7). Ideally, after completing the element extraction from Yin_k, there should be no remaining residue, or any remaining residue should be relatively small. To achieve this objective, the real part value of the out-of-band RZs will undergo optimization until the residue of Yin_k becomes less than *e*, i.e., 10^{-3} or less. This marks the end of the iteration process for the first channel. The same iterative process will be iterated for all other channels. Convergence is typically reached within 10 iterations for simpler topologies. However, for more intricate topologies, the number of iterations required for convergence will vary depending on the complexity level. Finally, the multiplexer's coupling matrix will be created using the circuit element values, i.e., J-inverters represent cross-coupling values and the susceptance represent self-coupling values in the coupling matrix and will be optimized using the gradient-based function *fminunc* in MATLAB without any constraints usually suffices. The typical optimization time is around a minute for complicated topologies, less than 30 s for triplexers and less than 5 s for diplexers. The S parameters can be obtained from the coupling matrix using the following formula:

$$\begin{aligned} A &= Q + sI + jM, \\ S_{11} &= 1 - 2A^{-1}(1,1), \\ S_{k1} &= 2A^{-1}(k,1), \end{aligned} \tag{4.8}$$

where, *Q* is a zero matrix, is which the value of the first and the last elements are set to 1. *I* and *M* are an identity matrix and the coupling matrix of the multiplexer, respectively. The iterative process can be summarized into the following steps:

1- Define a topology for the diplexer or multiplexer. Depict the equivalent circuit model of the multiplexer based on its topology.
2- Based on the filter order for each channel, obtain the in-band RZs of all channels using the Chebyshev filter relation and map them to a new frequency range, according to the

specifications, using (4.9).

$$s_{ik} = \frac{BW_k \times s_i}{2} + f_{ck}, \tag{4.9}$$

where s_{ik}, s_i, BW_k and f_{ck} are the converted in-band RZs for the kth channel, the RZs obtained from the Chebyshev relation, the kth channel bandwidth and central frequency, respectively.

3- Select one channel. Depending on the type of connection between the selected channel and the first node of other channels, the location of TZs and out-of-band RZs are estimated as explained earlier in this section.
4- Create polynomial F using the in-band and out-of-band RZs, obtained from steps 2 and 3, using (4.3).
5- Create polynomial P from the TZs obtained from step 3 and the specifications using (4.4).
6- Obtain polynomial E from (4.5) and use (4.6) to impose the specified RZ_k.
7- Use (4.7) to create the Yin_k and extract the circuit element of the selected channel and the first node of the other channels.
   Check the residue of Yin_k. If this is less than e, go to step 3 and select another channel. Repeat this process until all channels are processed. If the residue is more than e, go to step 3 and change the location of the TZ(s) and the real part of the out-of-band RZ(s).
8- End iteration. Use the elements value from step 8 to build the coupling matrix of the multiplexer.
9- The matrix usually needs a short local optimization mostly on the level of the RL.

To illustrate the synthesis process, an example of a triplexer with two third-order and a fourth-order filter channels is synthesized using the proposed method.

Step 1: The topology of the triplexer is displayed in Figure 4.5(a). The corresponding equivalent circuit model of the triplexer is in Figure 4.5(b). The specification of the triplexer is as follows:

- Low channel: channel filter order (N) = 3, normalized central frequency (ω_c)= -1.75, RL = 20 dB, BW = 0.85.
- Middle channel: N = 4, ω_c = 0, RL = 20 dB, BW = 1.
- High channel: N = 3, ω_c = 1.75, RL = 20 dB, BW = 0.85.

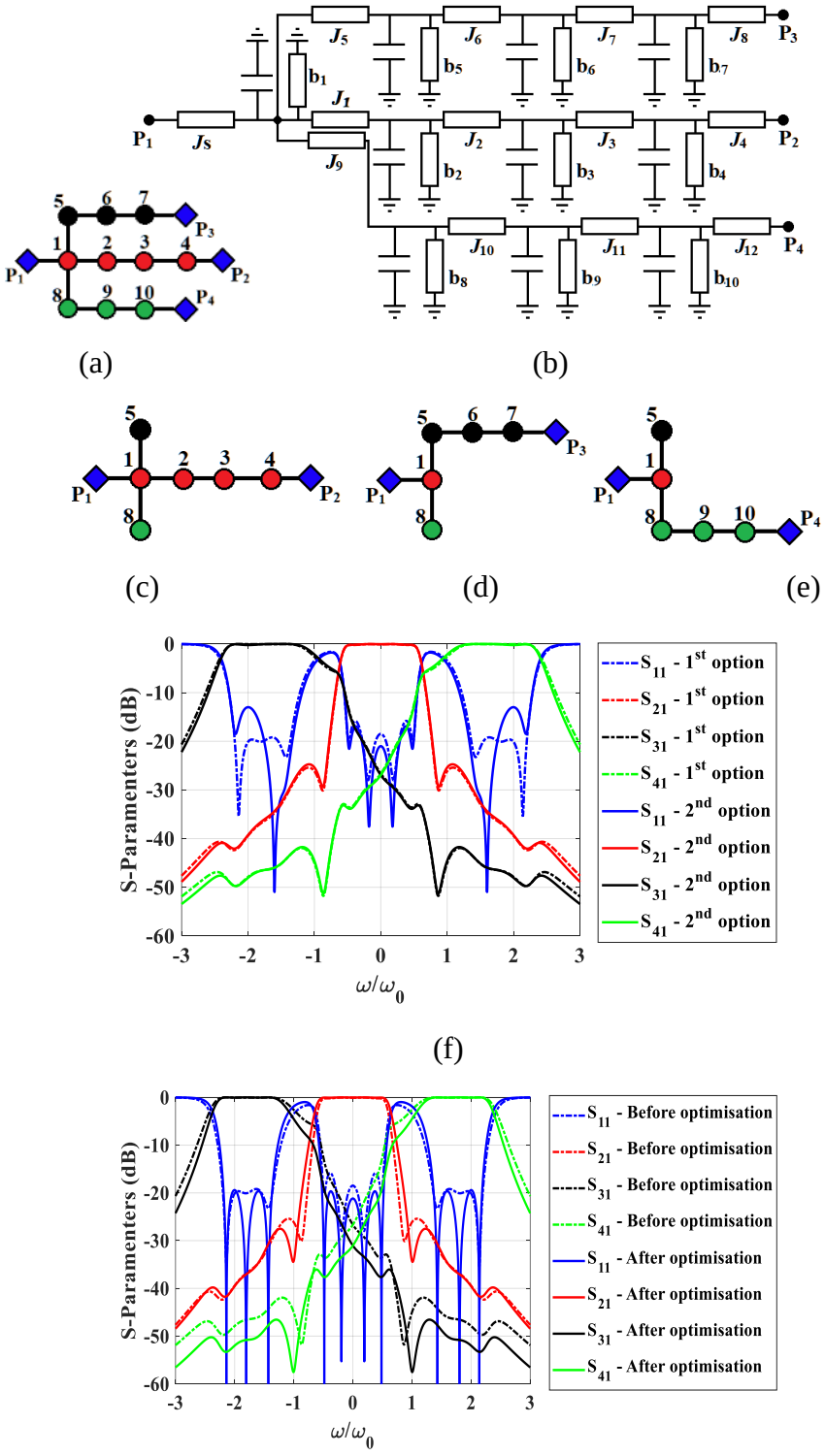

Figure 4.5 A triplexer with different channel filter order. (a) Topology. (b) circuit model. (c), (d) and (e) represent the scenario, in which channels P2, P3 and P4 are selected, respectively. (f) Two possible responses out of the iterative process. (g) S parameters. Colour of nodes corresponds to the channel's colour in the graph.

Step 2: Map the in-band RZs using (9) as below:

- Low channel: s_{iP3} = [-2.1830i, -1.75i, -1.3170i]

- Middle channel: s_{iP2} = [-0.4620i, -0.1913i, 0.1913i, 0.4620i]

- High channel: s_{iP4} = [2.1830i, 1.75i, 1.3170i]

Step 3: Firstly, the middle channel (P_2) is selected and then the second channel (P_3). Since the topology and the channel arrangements are symmetric, there is no need to repeat the process for channel P_4, whose circuit elements are similar to P_3 except for the sign of b_8, b_9 and b_{10}, which are reverse of b_5, b_6 and b_7. As illustrated in Figure 4.5(c), nodes 5 and 8 are connected in parallel to the selected middle channel P_2. So, two TZs and two out-of-band RZs are expected. The TZs are between channels P_2 and P_3 and between P_2 and P_4. The out-of-band RZs are at the central frequency of the other two channels. Next, assuming P_3 is selected, nodes 1 is cascade connected, whilst node 8 is in parallel. So, two out-of-band RZs are expected at the central frequencies of the other two channels. A single TZ is generated between channels P_2 and P_4. The out-of-band RZs have a real part, which are initially set to 0.5 in the iteration. The out-of-band RZs are added to the RZs obtained from Step 2 for each channel as follows:

If the low channel is selected (Figure 4.5(d)):

- s_{P3} = [-2.1830i, -1.75i, -1.3170i, 0.5, 1.75i+0.5]
- TZ_{p3} = [0.8750i]

If the middle channel is selected (Figure 4.5(c)):

- s_{P2} = [-0.4620i, -0.1913i, 0.1913i, 0.4620i, 1.75i+0.5, -1.75i+0.5]
- TZ_{p2} = [-0.8750i, 0.8750i]

If the high channel is selected (Figure 4.5(e)):

- s_{P4} = [-1.75i+0.5, 0.5, 2.1830i, 1.75i, 1.3170i]
- TZ_{p4} = [-0.8750i]

Step 4: The polynomial F is created based on the updated RZs in Step 3. The initial coefficients of F are obtained as follows:

- F_{P3} = [1, -1+3.5000i, 0.4375-4.3750i, 4.4063+12.0313i, -11.0547-2.8437i, 4.4024-1.2578i]
- F_{P2} = [1.0000, -1.0000, 3.5625, -0.2500, 0.8361, -0.0078, 0.0259]

- F_{P4} = [1, -1-3.5000i, 0.4375+4.3750i, 4.4063-12.0313i, -11.0547+2.8437i, 4.4024+1.2578i]

Step 5: Polynomial P is created based on the TZs initialized in Step 3. These are:

- P_{P3} = [1, -0.8750i] for the low channel
- P_{P2} = [1, 0, 0.7656] for the middle channel
- P_{P4} = [1, 0.8750i] for the high channel

Step 6: Polynomial E is obtained using (4.5) as follows:

- E_{P3} = [1, 2.0733+3.5i, 2.0868+6.3075i, -0.0314+14.9610i, -8.8629+9.8544i, -4.2507+1.7803i]
- E_{P2} = [1, 2.1252, 5.3207, 5.0105, 3.4250, 1.4419, 0.3586]
- E_{P4} = [1, 2.0733-3.5i, 2.0868-6.3075i, -0.0314-14.9610i, -8.8629-9.8544i, -4.2507-1.7803i]

Steps 7-10: The input admittance for each case is created using (4.7) and the circuit elements, according to Figure 4.5(b), are extracted. The initial values are as follows:

For the lower channel: J_S = 1.2396, J_5 = 1.0743, J_9 = 1.2790, J_6 = 0.4238, J_7 = 0.4463, J_8 = 0.8195, b_1= 0.0241, b_5= -1.4986, b_8= 0.8750, b_6= -4.6092, b_7= -1.5879.

For the middle channel: J_S = 1.25, J_5 = 0.5301, J_9 =0.5134, J_1 = 1.4879, J_2 = 1.0752, J_3 = 0.5018, J_4 = 0.4704, b_1=0, b_5= -0.8750, b_8= 0.8750, b_2= -0.0039, b_3= -0.0060, b_4= -0.0223.

For the high channel: J_S = 1.2396, J_9 = 1.0743, J_5 = 1.2790, J_{10} = 0.4238, J_{11} = 0.4463, J_{12} = 0.8195, b_1= 0.0241, b_8= 1.4986, b_5= -0.8750, b_9= 4.6092, b_{10}= 1.5879.

The residues from the three channels after extracting all elements are 245.83+178.9i, -0.1980+0.2089i and 245.83-178.9i, respectively. After 10 iterations for all three channels, the residues are reduced to less than 10^{-5}. The values for the RZs and TZs are as follows:

- s_{P3} = [-2.1830i, -1.75i, -1.3170i, 0.6363, 1.75i+0.5113]
- TZ_{p3} = [1.1430i]
- s_{P2} = [-0.4620i, -0.1913i, 0.1913i, 0.4620i, 1.75i+0.5113, -1.75i+0.5113]
- TZ_{p2} = [-1.1430i, 1.1430i]
- s_{P4} = [-1.75i+0.5113, 0. 6363, 2.1830i, 1.75i, 1.3170i]
- TZ_{p4} = [-1.1430i]

The value of generated TZ is shifted from ±0.8750*i* to ±1.143*i* within the iteration process. The synthesized values of circuit elements out of iterative process are:

For lower channel selected: J_S = 1.2973, J_5 = 1.1921, J_9 = 1.1584, J_6 = 0.4958, J_7 = 0.4944, J_8 = 0.7316, b_1= 0.0088, b_5= -1.2805, b_8= 1.1430, b_6= -1.6542, b_7= -1.6995.

For the middle channel selected: J_S = 1.2528, J_5 = 1.0470, J_9 =1.0470, J_1 = 0.7777, J_2 = 0.3497,

J_3 = 0.4543, J_4 = 0.7394, b_1=0, b_5= -1.1430, b_8= 1.1430, b_2= 0, b_3= 0, b_4= 0.

For higher channel selected: J_S = 1.2973, J_9 = 1.1921, J_5 = 1.1584, J_{10} = 0.4958, J_{11} = 0.4944, J_{12} = 0.7316, b_1= 0.0088, b_9= 1.2805, b_5= -1.1430, b_{10}= 1.6542, b_{11}= 1.6995.

The proposed method ends up with two or more possible values for circuit elements. For instance, for J_S, J_5 and J_9 two sets of values of 1.2973, 1.1921, 1.1584, respectively (1st option) and 1.2528, 1.0470, 1.0470 (2nd option) are obtained. In order to choose the best values, each option is used to create a coupling matrix and then the responses, which are compared in Figure 4.5(f). A more desirable response is selected to proceed with. In this example, option 1 is selected, and it was optimized in 2.79 s. The optimized response is compared with the initial coupling matrix in Figure 4.5(g). The coupling matrix elements before and after optimization are presented in Table 4.1.

Table 4.1 Coupling matrix elements

	Before	**After**		**Before**	**After**
m(P_1,1)	1.2973	1.2302	m(9,10)	0.4944	0.4325
m(4,P_2)	0.7394	0.7415	m(8,8)	1.2805	1.3732
m(7,P_3)	0.7316	0.6927	m(9,9)	1.6542	1.6886
m(10,P4)	0.7316	0.6927	m(10,10)	1.6995	1.7450
m(1,5)	1.1921	1.0500	m(5,6)	0.4958	0.4339
m(1,8)	1.1584	1.0500	m(6,7)	0.4944	0.4325
m(1,2)	0. 7777	0.7744	m(5,5)	-1.281	-1.373
m(2,3)	0.3497	0.3598	m(6,6)	-1.654	-1.688
m(3,4)	0.4543	0.4622	m(7,7)	-1.699	-1.745
m(8,9)	0.4958	0.4339			

4.3 Results and discussions

In this section, seven more examples of all-resonator diplexers and multiplexers are synthesized using the proposed method. The reason for providing several examples is to show the capability of the proposed method for synthesis of different topologies, to prove the time efficiency of the method and to show the effect of different channel arrangements in a topology on the multiplexer response. The iterative method is performed on a low-end laptop with i7-2630QM CPU at 2 GHz and 8 GB RAM and the optimization is done on a desktop computer with i5-5600 CPU at 3.5 GHz and 24 GB RAM. All the coupling matrices for the following examples are compared before and after optimization and presented in the Appendix.

Example 1: A diplexer with third-order channel filters. Its topology is depicted in the inset of Figure 4.6. The specification is $N = 3$, $\omega_c = \pm 0.75$, $RL = 20$ dB, BW = 0.5. The initial coupling matrix out of the iterative method is obtained and the corresponding S parameters are displayed in Figure 4.6. As can be seen in Figure 4.6, there is no TZs generated due to the topology. The reason is that by selecting either of the two channels for starting the synthesis process, the first node of the other channel is connected in cascade to the selected channel. Therefore, no TZs will be generated, as explained in Section 4.2. After an optimization of 0.6 s, the return loss is further improved as shown in Figure 4.6. The matrices before and after optimization are compared in the Appendix. The coupling matrix elements obtained out of the proposed synthesis method is fairly close to the one after optimization.

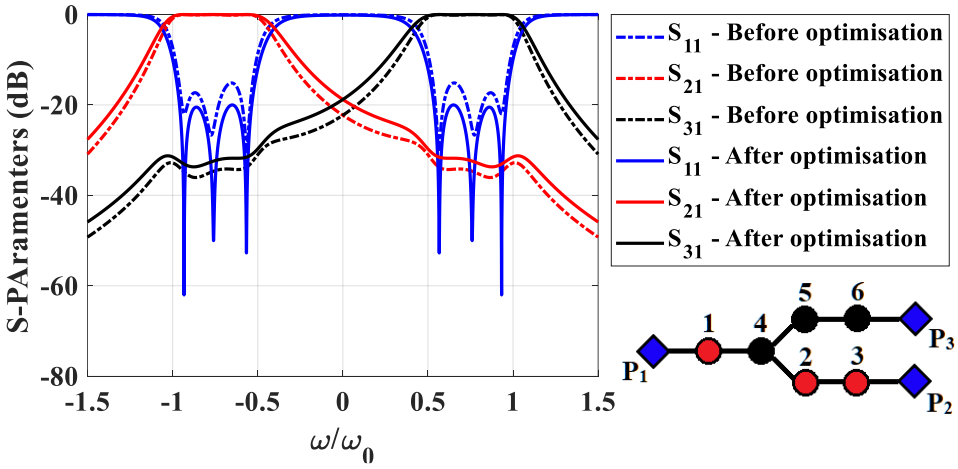

Figure 4.6 Diplexer with two third-order channel filters. The red and black nodes belong to the lower and higher channels, respectively.

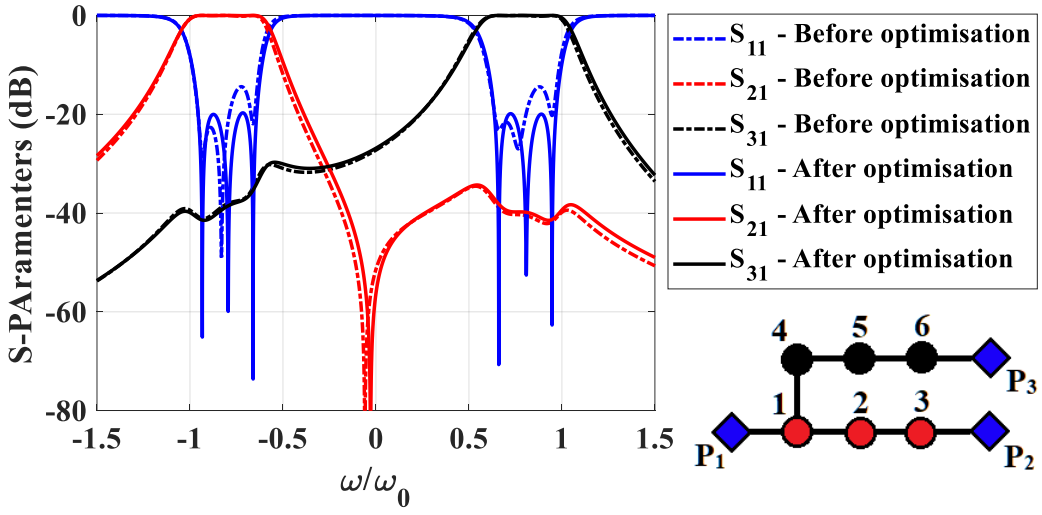

Figure 4.7 Same diplexer as Figure 4.6 with different channel connection. The red and black nodes belong to the lower and higher channels, respectively.

Example 2: This is a diplexer of the same channel filter order as example 1 but using a different topology as displayed in Figure 4.7. In this topology, node 4 of channel P3 is connected in parallel to the channel P2. So, one TZ is expected between the two channels, when the channel P2 is selected for the synthesis. While in the topology in the example 1 (Figure 4.6), the first node of either of the two channels was connected in cascade with the other channel. So, no TZ was expected. The specification is N = 3, ω_c = ±0.8, RL = 20 dB, BW = 0.4. The coupling matrix optimization took 1.1 s. The optimized response is compared with the response from the iteration process in Figure 4.7, in which a TZ around ω = 0 is evident.

Example 3: These are two diplexers with a same topology and different channel filter orders and TZ locations. First diplexer has a second-order channel containing a non-resonating node (NRN) and a dangling node, generating a TZ, and a fourth-order channel. The topology of the diplexer is displayed in Figure 4.8(a). The white node represents the NRN. The specification is as follows:

- Low channel: N = 4, ω_c = -0.8, RL = 20 dB, BW = 0.4.

- High channel: N = 2, ω_c = 0.8, RL = 20 dB, BW = 0.4, TZ @ ω = 0.

The coupling matrix optimization process lasted for 2.76 s. Figure 4.8(a) compares the initial response (after the iteration process) and the optimized one. The TZ on the low channel (red graph) is generated due to the parallel connection of node 5 with channel P2, when it is selected for synthesis. The TZ on the high channel (black curve) is generated by the dangling node.

Second diplexer has a same topology with an extra node added to the high channel as shown in Figure 4.8(b). The third-order channel generates a TZ at the edge of the low channel. The specification only differs from Figure 4.8(a) in that the high channel is a third-order and the TZ is assigned to ω=-0.6. The coupling matrix optimization process lasted for 2.6 s. Figure 4.8(b) shows the comparison between the initial response and the optimized one. These two examples show how a TZ, generated using NRN technique, together with a TZ, generated due to the all-resonator topology, can improve the isolation between the two channels of a diplexer. Moreover, these examples show that there is almost no freedom in changing the location of the TZ, which is generated because of the topology.

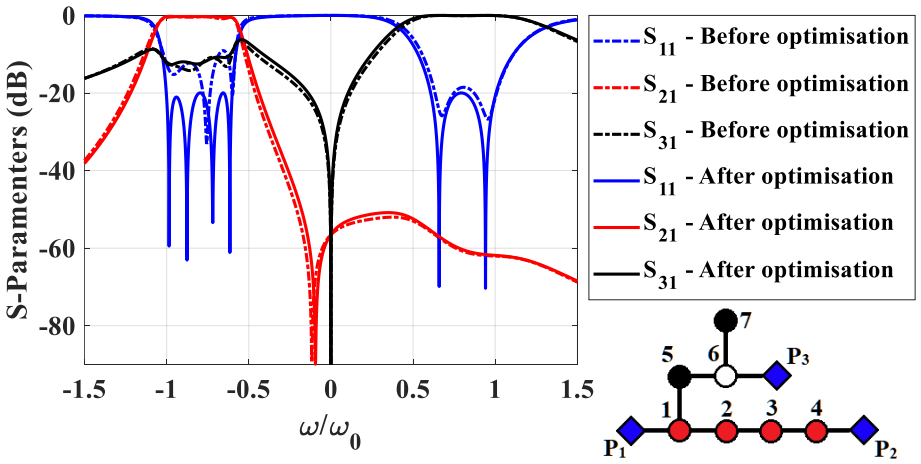

(a)

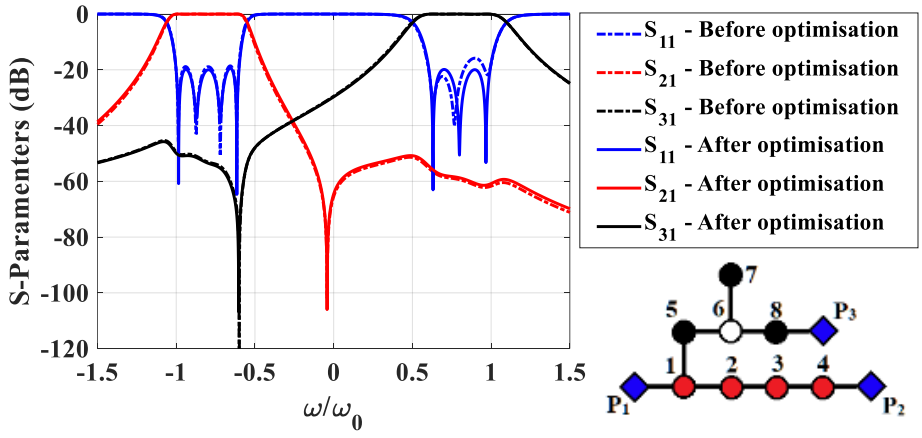

(b)

Figure 4.8 Diplexers with NRN in one channel.

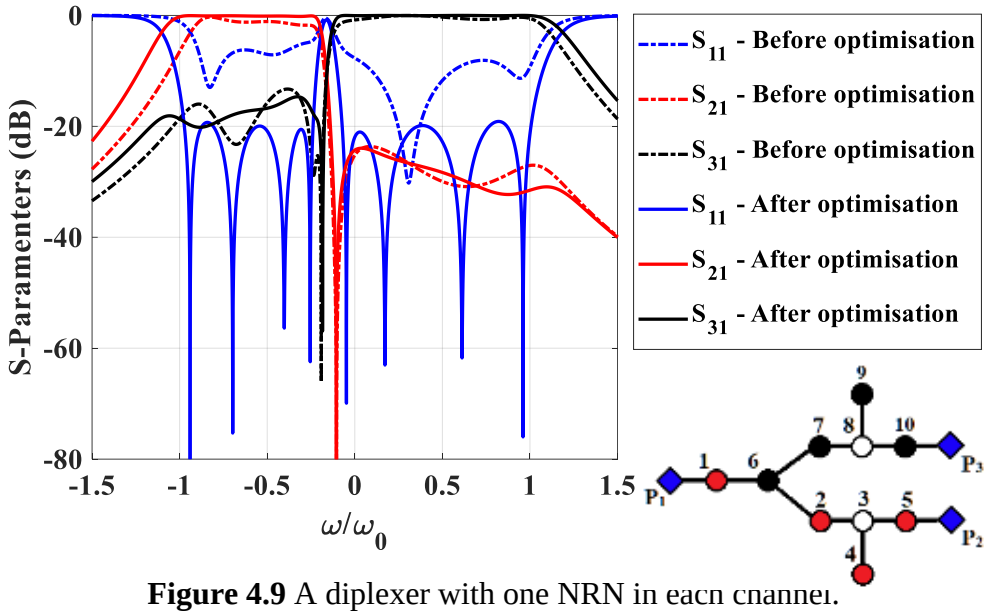

Figure 4.9 A diplexer with one NRN in each channel.

Example 4: Different from the previous examples, this is a contiguous diplexer with two fourth-order channels, each with a dangling node, generating a TZ at the edge of the other channel in order to enhance the isolation. The topology is displayed in Figure 4.9. The specification of the diplexer is:

- Low channel: N = 4, ω_c = -0.63, RL = 20 dB, BW = 0.74. TZ @ ω = -0.1238
- High channel: N = 4, ω_c = 0.46, RL = 20 dB, BW = 1.1, TZ @ ω = -0.2108.

This is a very challenging example due to the channels, which are very close to each other, and the NRNs in each channel. The coupling matrix optimization process lasted for 3.8 s. Figure 4.9 shows the comparison between the initial response and the optimized one. Although the S parameters before the optimization look far from the ideal response, but a very short optimization solved the issue. This is because the initial coupling matrix is a very good starting point and leads to a very quick convergence.

Example 5: A triplexer is synthesized with fourth-order channel filters. The topology of the triplexer is displayed in the inset of Figure 4.10. The specification for the low, middle, and high frequency channels are N = 4, ω_c = -0.7778, 0, 0.7778, RL = 20 dB, BW = 0.4444. The coupling matrix optimization process lasted for 4s. The optimized response is compared with the response before optimization (initial response) in Figure 4.10. Again, the good initial point generated by the proposed method leads to a quick optimization.

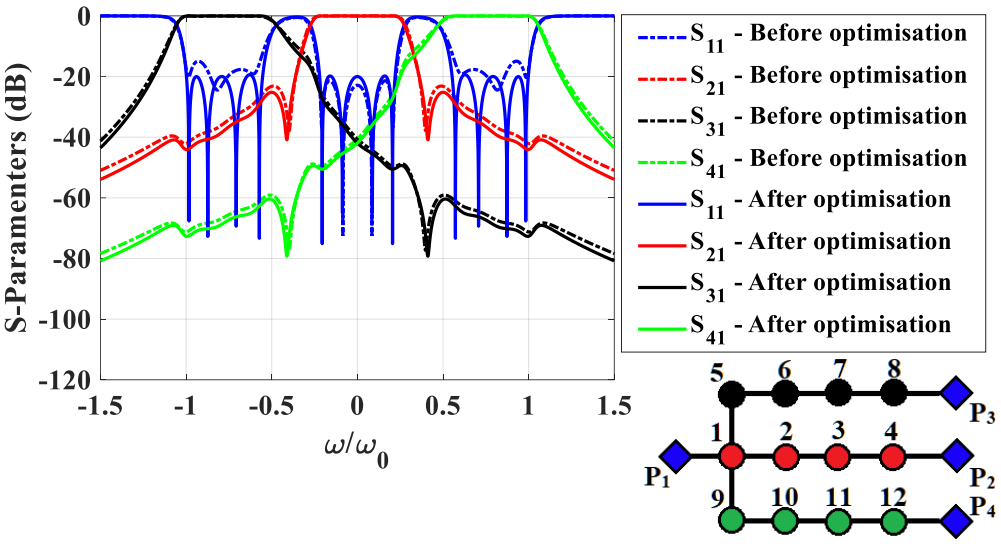

Figure 4.10 A triplexer with fourth-order channel filters. The nodes' colour in the topology represents the corresponding channel in the S parameter graph with the same colour.

Example 6: Two triplexers with third-order channel filters are depicted in Figure 4.11(a) and Figure 4.11(b). They have the same topology. The difference from Example 6 is the channel arrangements. For the first triplexer (Figure 4.11(a)), the channels are arranged such that P_2 is the middle channel, P_3 is the low-frequency channel and P_4 is the high frequency channel. For the second triplexer (Figure 4.11(b)), P_2 is the high-frequency, P_3 is the low-frequency and P_4 is the middle channel. Both triplexers have the same specification: N = 3, ω_c = -0.8, 0, 0.8, respectively for low, middle, and high frequency channel filters, RL = 20 dB, BW = 0.4. The coupling matrices are optimized within 5.58 s and 8.43 s, respectively. The corresponding S parameters are also displayed in Figure 4.11. As can be seen, by just changing the channel organization, the response of the triplexer, especially the location of generated TZs, changes. In general, synthesis of symmetric topologies, such as the one in the example 5, is easier than asymmetric one in this example. This is because the location of TZs and RZs are mirrored about the normalized frequency of 0. This would halve the iterations and optimization time. Moreover, comparing the S parameters between the example 5 and example 6, it seems that the channel isolation is better in the symmetric topology.

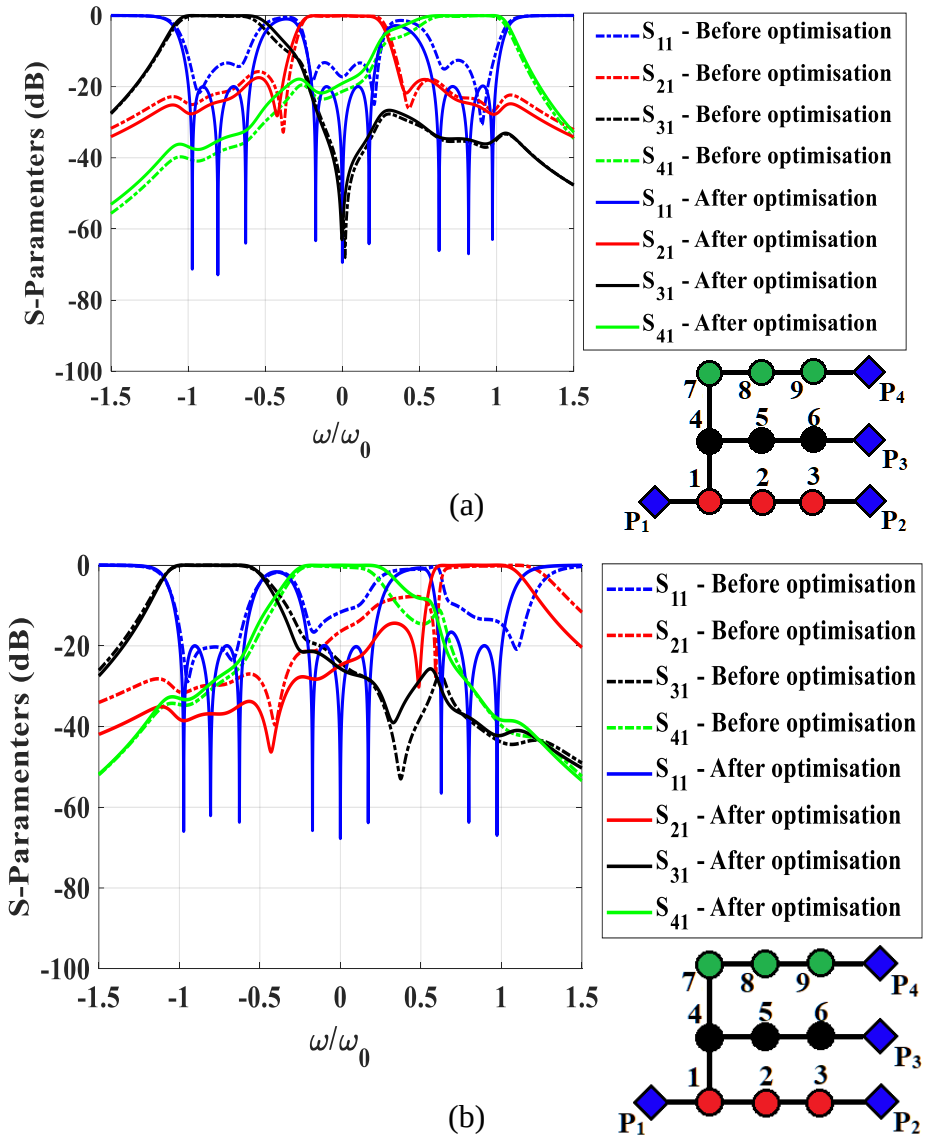

Figure 4.11 A triplexer with third-order channel filters. (a) First channel arrangement. (b) Second channel arrangement.

Example 7: A quadruplexer is synthesized with fourth-order channel filters. The topology is displayed in Figure 4.12(a). The specification for the four channels is N = 4, ω_c = -0.8750, -0.2917, 0.2917, 0.8750, RL = 20 dB, BW = 0.25. The coupling matrix optimization process took 10.6 s. The optimized response is compared with the initial one in Figure 4.12. The same quadruplexer is synthesized within 20-30 min using an optimization technique [17]. Using our method, we can considerably reduce the computation time to seconds.

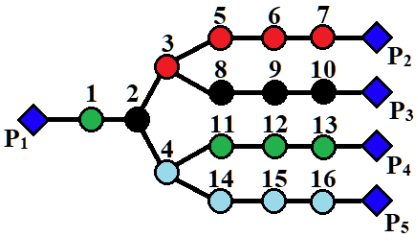

(a)

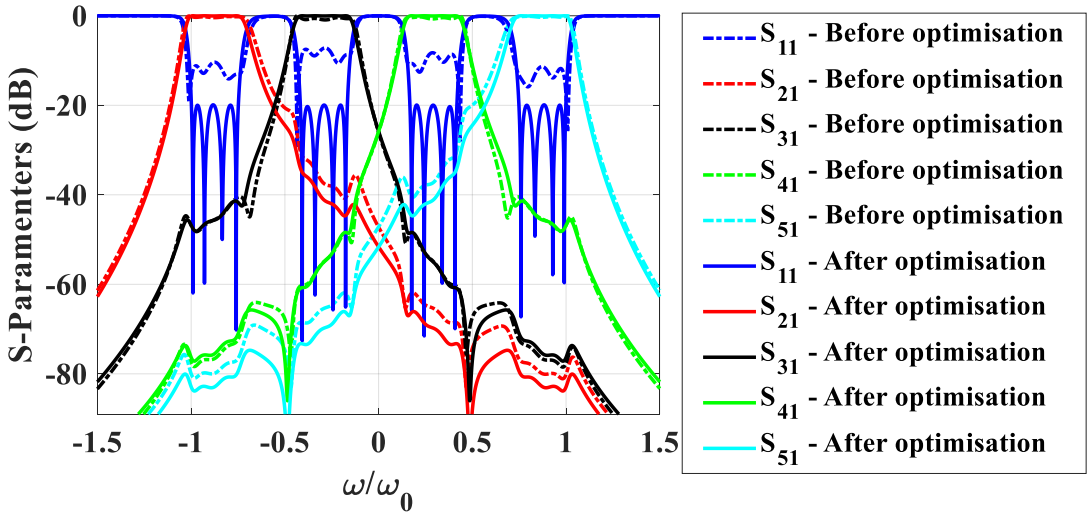

(b)

Figure 4.12 A quadplexer with fourth-order channel filters. (a) Topology. (b) S parameters.

4.4 Conclusion

In this paper, we present a quick synthesis method for all-resonator multiplexers using an iterative technique. The approach is rooted in the characteristic polynomials of each channel, taking into account the loading effect from other channels. The iterative process yields a highly effective initial coupling matrix for the multiplexer, enabling fast local optimization to attain the final coupling matrix. This marks a significant advancement over prior optimization-based methods [15],[17] , offering improved convergence and efficiency in determining the coupling matrix for intricate all-resonator multiplexer topologies. Through the examination of seven examples with varying topologies and complexities, our results demonstrate that the proposed method substantially reduces computational load and time.

4.5 Appendix

The following tables present the elements of the coupling matrices before and after optimization for the presented examples in Section 4.3.

Table 4.2 Coupling matrix elements for example 1

	Before	**After**		**Before**	**After**
m(P_1,1)	0.9072	1.0069	m(2,2)	-1.4065	-1.3906
m(3,P_2)	0.6560	0.7098	m(3,3)	-1.4761	-1.4774
m(6,P_3)	0.6560	0.7098	m(4,5)	0.5323	0.5803
m(1,4)	1.6249	1.6270	m(5,6)	0.3981	0.4493
m(4,2)	0.5323	0.5803	m(5,5)	1.4065	1.3906
m(2,3)	0.3981	0.4493	m(6,6)	1.4761	1.4774

Table 4.3 Coupling matrix elements for example 2

	Before	**After**		**Before**	**After**
m(P_1,1)	0.9309	0.9716	m(2,2)	-2.0030	-1.9973
m(3,P_2)	0.6534	0.6772	m(3,3)	-2.0250	-2.0087
m(6,P_3)	0.6961	0.6958	m(4,5)	0.5838	0.5887
m(1,4)	1.9969	2.0150	m(5,6)	0.4275	0.4321
m(1,2)	0.5565	0.5804	m(5,5)	1.9101	1.9164
m(2,3)	0.3906	0.4046	m(6,6)	1.9797	1.9931
m(1,1)	-0.021	0.0556	m(4,4)	0.0238	0.1096

Table 4.4 Coupling matrix elements for example 3

	Figure 8(a)			**Figure 8(b)**	
	Before	**After**		**Before**	**After**
m(P_1,1)	0.6993	0.7192	m(P_1,1)	0.6461	0.6584
m(4,P_2)	0.4448	0.4588	m(4,P_2)	0.4519	0.4672
m(6,P_3)	0.7303	0.7624	m(8,P_3)	0.4819	0.4753

m(1,5)	0.8937	0.8699	m(1,5)	0.7996	0.8107
m(1,2)	0.2914	0.2728	m(1,2)	0.2535	0.2602
m(2,3)	0.1363	0.1393	m(2,3)	0.1375	0.1396
m(3,4)	0.1736	0.1803	m(3,4)	0.1769	0.1821
m(1,1)	0.1328	0.1322	m(1,1)	0.0140	0.0368
m(2,2)	-0.802	-0.804	m(2,2)	-0.802	-0.801
m(3,3)	-0.809	-0.807	m(3,3)	-0.806	-0.805
m(4,4)	-0.864	-0.807	m(4,4)	-0.806	-0.804
m(5,6)	0.6356	0.6809	m(5,6)	1	1
m(6,7)	1	1	m(6,7)	4.8823	4.8836
m(5,5)	-0.155	-0.131	m(7,8)	0.7389	0.7198
m(6,6)	-1.518	-1.563	m(5,5)	0	0
m(7,7)	0	0	m(6,6)	-17.99	-17.99
			m(7,7)	-0.600	-0.603
			m(8,8)	0.7716	0.7718

Table 4.5 Coupling matrix elements for example 4

	Before	**After**		**Before**	**After**
m(P_1,1)	1.3283	1.4749	m(4,4)	2.8848	2.8869
m(5,P_2)	1.4615	0.9365	m(5,5)	3.5105	3.4488
m(10,P_3)	1.3784	1.1363	m(6,7)	1.0693	1.1245
m(1,6)	1.6691	1.9140	m(7,8)	1	1
m(6,2)	0.7731	0.8495	m(8,9)	0.8624	0.8056
m(2,3)	1	1	m(9,10)	1.1924	1.3677
m(3,4)	1.3016	1.2869	m(6,6)	2.3212	2.5870
m(3,5)	1.2197	1.3610	m(7,7)	2.3980	2.2767
m(1,1)	2.5774	2.5620	m(8,8)	1.5598	1.5805
m(2,2)	3.5851	3.6839	m(9,9)	3.0848	3.0686
m(3,3)	-2.973	-2.947	m(10,10)	2.5204	2.7165

Table 4.6 Coupling matrix elements for example 5

	Before	**After**		**Before**	**After**
m(P_1,1)	1.4125	1.2614	m(9,9)	1.3053	0.3458
m(4,P_2)	0.7610	0.7208	m(10,10)	1.6634	1.6476
m(8,P_3)	0.7676	0.7322	m(11,11)	1.7199	1.7175
m(12,P4)	0.7676	0.7322	m(12,12)	1.7221	1.7336
m(1,5)	1.1483	1.0887	m(5,6)	0.4801	0.4641
m(1,9)	1.1483	1.0887	m(6,7)	0.3704	0.3627
m(1,2)	0.8804	0.7814	m(7,8)	0.4835	0.4593
m(2,3)	0.3572	0.3420	m(5,5)	-1.305	-1.345
m(3,4)	0.4686	0.4399	m(6,6)	-1.663	-1.647
m(9,10)	0.4801	0.4641	m(7,7)	-1.719	-1.717
m(10,11)	0.3704	0.3627	m(8,8)	-1.722	-1.733
m(11,12)	0.4835	0.4593			

Table 4.7 Coupling matrix elements for example 6

	Figure 11(a)		**Figure 11(b)**	
	Before	**After**	**Before**	**After**
m(P_1,1)	0.8161	0.8395	0.8623	0.8293
m(3,P_2)	0.4848	0.4692	0.5628	0.4591
m(6,P_3)	0.4736	0.4858	0.4984	0.4837
m(9,P4)	0.4529	0.4988	0.4847	0.4930
m(1,2)	0.3975	0.3502	0.5000	0.3501
m(2,3)	0.2064	0.1969	0.2590	0.1954
m(1,4)	0.7566	0.6932	0.6735	0.6977
m(4,5)	0.2532	0.2674	0.2548	0.2523
m(5,6)	0.2014	0.2099	0.2153	0.2071
m(4,7)	0.5373	0.5824	0.4628	0.4214
m(7,8)	0.3037	0.3150	0.2153	0.2292
m(8,9)	0.2042	0.2348	0.2104	0.2196
m(1,1)	-0.041	0.0016	-0.102	-0.012

m(2,2)	0	-0.003	0.8312	0.8083
m(3,3)	0	-0.002	0.8702	0.8331
m(4,4)	0.0360	-0.015	-0.192	-0.172
m(5,5)	-0.767	-0.755	-0.763	-0.764
m(6,6)	-0.791	-0.789	-0.787	-0.792
m(7,7)	0.1686	0.1649	0.2139	0.0589
m(8,8)	0.6745	0.6554	0	0.0249
m(9,9)	0.7627	0.7552	0	0.0071

Table 4.8 Coupling matrix elements for example 7

	Before	**After**		**Before**	**After**
m(P_1,1)	0.9779	1.1387	m(14,15)	0.2455	0.2229
m(7,P_2)	0.6009	0.5679	m(15,16)	0.2957	0.2761
m(10,P_3)	0.5577	0.5689	m(1,1)	0.0676	0
m(13,P4)	0.5577	0.5689	m(2,2)	-0.055	0
m(16,P5)	0.6009	0.5679	m(3,3)	1.0385	1.0767
m(1,2)	1.7006	1.7402	m(4,4)	-1.038	-1.076
m(2,3)	0.9089	0.9598	m(5,5)	1.8514	1.9652
m(2,4)	0.8993	0.9597	m(6,6)	2.0656	2.0782
m(3,5)	0.5314	0.4169	m(7,7)	2.0755	2.0887
m(3,8)	0.3437	0.3176	m(8,8)	0.7456	0.7290
m(5,6)	0.2455	0.2229	m(9,9)	0.7063	0.7047
m(6,7)	0.2957	0.2761	m(10,10)	0.7054	0.7036
m(8,9)	0.2131	0.2137	m(11,11)	-0.745	-0.729
m(9,10)	0.2693	0.2753	m(12,12)	-0.706	-0.704
m(4,11)	0.3437	0.3176	m(13,13)	-0.705	-0.703
m(4,14)	0.5314	0.4169	m(14,14)	-1.851	-1.965
m(11,12)	0.2131	0.2137	m(15,15)	-2.065	-2.078
m(12,13)	0.2693	0.2753	m(16,16)	-2.075	-2.088

References

[1] Y. Yang, M. Yu, Q. Wu, X. Yin and J. Yang, "A Fully Integrated Multiplexer Using Unified Extracted Pole Technique," *IEEE Transactions on Microwave Theory and Techniques*, vol. 68, no. 8, pp. 3439-3447, Aug. 2020.

[2] X. -P. Liang, K. A. Zaki and A. E. Atia, "A rigorous three plane mode-matching technique for characterizing waveguide T-junctions, and its application in multiplexer design," *IEEE Transactions on Microwave Theory and Techniques*, vol. 39, no. 12, pp. 2138-2147, Dec. 1991.

[3] Yu Rong, Hui-Wen Yao, K. A. Zaki and T. G. Dolan, "Millimeter-wave Ka-band H-plane diplexers and multiplexers," *IEEE Transactions on Microwave Theory and Techniques*, vol. 47, no. 12, pp. 2325-2330, Dec. 1999.

[4] R. I. Cameron and M. Yu, "Design of manifold-coupled multiplexers," *IEEE Microwave Magazine*, vol. 8, no. 5, pp. 46-59, Oct. 2007.

[5] K. Uenishi, K. Araki and H. Ishii, "Transmitter multiplexing system in UHF mobile radio," *IEEE Transactions on Vehicular Technology*, vol. 18, no. 1, pp. 1-11, May 1969.

[6] R. R. Mansour, V. Dokas, G. Thomson, Wai-Cheung Tang and C. M. Kudsia, "A C-band superconductive input multiplexer for communication satellites," *IEEE Transactions on Microwave Theory and Techniques*, vol. 42, no. 12, pp. 2472-2479, Dec. 1994.

[7] R. R. Mansour, "Design of superconductive multiplexers using single-mode and dual-mode filters," *IEEE Transactions on Microwave Theory and Techniques*, vol. 42, no. 7, pp. 1411-1418, July 1994.

[8] J. Chang, J. Fiedziuszko, S. Berry and D. Harvey, "Microstrip hybrid coupled input multiplexer design for satellite communications," *2014 IEEE MTT-S International Microwave Symposium (IMS2014)*, 2014, pp. 1-3.

[9] G. Macchiarella and S. Tamiazzo, "Synthesis of Star-Junction Multiplexers," *IEEE Transactions on Microwave Theory and Techniques*, vol. 58, no. 12, pp. 3732-3741, Dec. 2010.

[10] P. Zhao and K. -L. Wu, “An Iterative and Analytical Approach to Optimal Synthesis of a Multiplexer With a Star-Junction,” *IEEE Transactions on Microwave Theory and Techniques*, vol. 62, no. 12, pp. 3362-3369, Dec. 2014.

[11] H. Meng, P. Zhao, K. -L. Wu and G. Macchiarella, “Direct Synthesis of Complex Loaded Chebyshev Filters in a Complex Filtering Network,” *IEEE Transactions on Microwave Theory and Techniques*, vol. 64, no. 12, pp. 4455-4462, Dec. 2016.

[12] T. Skaik, M. Lancaster, and F. Huang, “Synthesis of multiple output coupled resonator microwave circuits using coupling matrix optimization,” *IET Journal of Microwaves, Antenna & Propagation*, vol.5, no.9, pp. 1081-1088, June 2011.

[13] D. Tubail, T. Skaik, “Synthesis of Coupled Resonator Based Multiplexers with Generalized Structures Using Coupling Matrix Optimization,” *IET Electronic Letters*, vol.51, no.23, pp. 1891-1893, Nov. 2015.

[14] T. F. Skaik and D. A. Tubail, "Novel multiplexer topologies based on coupled resonator structures," *2015 IEEE 15th Mediterranean Microwave Symposium (MMS)*, Lecce, Italy, 2015, pp. 1-4.

[15] Y. Yu, Y. Wang, C. Guo, Q. S. Cheng and M. Yu, “Resonant Manifold Multiplexers,” *IEEE Transactions on Microwave Theory and Techniques*, vol. 70, no. 2, pp. 1059-1071, Feb. 2022.

[16] X. Shang, Y. Wang, W. Xia and M. J. Lancaster, “Novel Multiplexer Topologies Based on All-Resonator Structures,” *IEEE Transactions on Microwave Theory and Techniques*, vol. 61, no. 11, pp. 3838-3845, Nov. 2013.

[17] Y. Yu, B. Liu, Y. Wang, M. J. Lancaster and Q. S. Cheng, “A General Coupling Matrix Synthesis Method for All-Resonator Diplexers and Multiplexers,” *IEEE Transactions on Microwave Theory and Techniques*, vol. 68, no. 3, pp. 987-999, March 2020.

[18] D. Tubail, T. Skaik “A Direct Approach for Coupling Matrix Synthesis for Coupled Resonator Diplexers,” *Journal of Microwaves, Optoelectronics and Electromagnetic Applications*, Vol. 16, No. 4, pp. 942-953, Dec. 2017.

[19] S. Tamiazzo, G. Macchiarella and F. Seyfert, “Path Filters: A Class of True Inline Topologies With Transmission Zeros,” *IEEE Transactions on Microwave Theory and Techniques*, vol. 70, no. 1, pp. 850-863, Jan. 2022.

[20] Y. Zeng, Y. Yang, Y. Wu, M. Yu, J. Peng and D. Liang, “Exploiting Redundancy in Direct Synthesis for Inline Filters,” *IEEE Transactions on Microwave Theory and Techniques*, vol. 69, no. 10, pp. 4489-4498, Oct. 2021.

CHAPTER 5

DESIGN OF NRN BASED THIRD-ORDER FILTER WITH TWO TZS

Paper published

Abolfazl Mostaani*, Lu Qian*, Rafael Martinez**, Paul F. Wilson***, Moataz M. Attallah**, Yi Wang*, Mark A. Williams***

2021 IEEE MTT-S International Microwave Filter Workshop (IMFW), Perugia, Italy, 2021, pp. 316-318, doi: 10.1109/IMFW49589.2021.9642309.

A. Mostaani synthesised and designed the filter and wrote the manuscript and presented the work at the conference. Y. Wang collaborated in writing the manuscript. L. Qian assisted in the measurements. R. Martinez and M. M. Attallah fabricated the designed filter. P. F. Wilson and M. A. Williams conducted the X-Ray imaging and dimensional measurements.

* School of Engineering University of Birmingham, Birmingham, U.K.

** School of Metallurgy and Materials, University of Birmingham, Birmingham, U.K.

*** Warwick Manufacturing Group, University of Warwick, Coventry, U.K.

In this chapter a narrowband third-order filter at 9 GHz with two transmission zeros is designed using the non-resonating node (NRN) method. The work is published in [1].

5.1 Introduction

Additive manufacturing (AM) is an emerging technology for the fabrication of microwave devices. Thanks to the recent advances in rapid prototyping industry, AM is capable of producing low-weight microwave devices with complex structure. Besides, AM is able to fabricate the structures in a single part. This is an important advantage over the regular fabrication technologies such as CNC machining, where the structures are usually assembled from two or more separately manufactured blocks. As a result, lack of suitable surface contact between the split blocks leads to increase in loss and performance degradation. AM microwave components have demonstrated competitive performance at X-band [2]-[4] in comparison with CNC machining. AM includes different fabricating technologies such as selective laser melting (SLM), fused deposition modelling (FDM), polyjet printing, stereo-lithographic apparatus (SLA), and 3-D screen printing, etc. Each technology has its own limitation in terms of printing resolution, accuracy and achievable surface roughness. The SLM technology, capable of producing a minimum surface roughness of 1.5-2 μm, is an excellent candidate for printing metal waveguide devices [5]. However, printing parameters such as powder size, energy input, scan speed, heat treatment and printing direction all impact on the dimensional accuracy and surface quality of the printed parts and therefore RF/microwave performance [6],[7].

For narrowband filters, one design drive is to reduce the order of filters while maintaining sharp roll-off at the band edges, in order to not only reduce the insertion loss but also save mass and volume. Although cross coupling topologies can address such issues, they are relatively sensitive to fabrication tolerances [8],[9]. On the other hand, inline non-resonating node (NRN) filters are shown to be less sensitive to dimensional tolerance [10]. This is because of the modularity property of the NRN method, in which the location of the transmission zeros (TZs) can be adjusted independently [11].

In this chapter, a third-order X-band filter with two TZs is designed using the NRN method and fabricated using the SLM technology. The functional bandwidth of the filter is 100 MHz with 1.11% FBW. Comparing to the SLM fabricated filters in the literatures, the presented filter is among the narrowest band filters [12]-[15] and challenges the SLM printing capability. The

work will have a focus on examining the dimensional imperfection rendered by the SLM fabrication process.

5.2 Synthesis, design, and fabrication

The third-order bandpass filter, which has a central frequency of 9 GHz and bandwidth of 100 MHz is designed. The filter has two TZs, which are located at normalised frequency of $\omega_1 = -3j$ and $\omega_2 = 3j$. The minimum return loss of the filter within the passband is set to 17 dB. Figure 5.1 shows the topology of the filter together with its equivalent circuit model. The filter synthesis is carried out using the NRN method [10] and the value of circuit elements in Figure 5.1(b) is obtained as $J_1 = 1$, $J_2 = 2.7574$, $J_3 = 0.9458$, $J_4 = 1$, $J_5 = 2.9155$, $J_6 = 1.0573$, $B_1 = 2.770i$, $b_2 = 3i$, $b_3 = 0$, $B_4 = -3.096i$ and $b_5 = -3i$. All the capacitors' value is normalised to 1. Applying the Kirchoff's voltage and current laws on the equivalent circuit, the admittance matrix of the filter can be written as [Y] = [Q] + p[I] + j[M]. The matrix Q is a 7×7 zero matrix, in which Q(1,1) = Q(7,7) = 1. The matrix I is an identity matrix of size 7 and I(1,1) = I(2,2) = I(5,5) = I(7,7) = 0. The parameter p is the complex lowpass frequency variable. The matrix M represents the filter coupling matrix, which is expressed in (5.1).

	S	1	2	3	4	5	L
S	0	1	0	0	0	0	0
1	1	-2.770	2.7574	0.9458	0	0	0
2	0	2.7574	-3	0	0	0	0
3	0	0.9458	0	0	1	0	0
4	0	0	0	1	3.0964	2.9155	1.0573
5	0	0	0	0	2.9155	3	0
L	0	0	0	0	1.0573	0	0

(5.1)

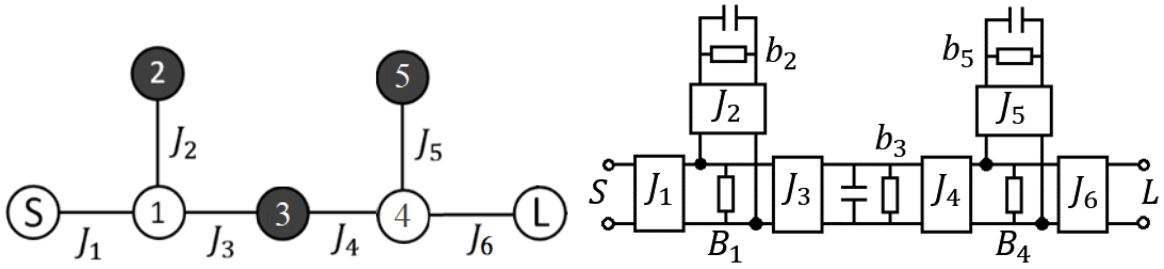

(a) (b)

Figure 5.1 A 3-2 filter. (a) Topology of the filter. The black circles represent the resonators, and the white circles refer to the non-resonating nodes. The *S* and *L* are the source and load, respectively. (b) The equivalent circuit model of the filter.

The design process starts with dividing the filter topology to three subsections, whose corresponding coupling matrices are extracted from (5.1). Figure 5.2 shows the three subsections together with their coupling matrix. Each subsection is designed separately. It must be noted that in each subsection, one or two resonators are replaced with the ports (*S* or *L*). Consequently, one or two internal couplings have to be converted to external couplings. For example, the resonator 3 (see Figure 5.1(a)) is replaced with the port *L* in Figure 5.1(a). As a result, the internal coupling J_3 in Figure 5.1(a) must be converted to the external coupling J_3' in Figure 5.2(a). Such changes must be addressed in the corresponding submatrix elements. The diagonal elements of submatrix show the self-coupling of the corresponding components (either resonators, NRNs or ports) in the filters' topology. The ports don't have a self-coupling in this design. So, the self-coupling of those resonators, which are replaced with the port, must be changed to zero. For example, resonators 1 and 4 (see Figure 5.1(a)) are replaced with ports *S* and *L*, respectively, in Figure 5.2(b). So, the corresponding elements, i.e., the first and the last elements of the diagonal of the submatrix in Figure 5.2(b), are set to zero. Moreover, the corresponding internal couplings J_3 and J_4 in Figure 5.1(a) must be changed to the external coupling J_3' and J_4' in Figure 5.2(b) using the following equation [16]:

$$J_i' = J_i \times \sqrt{FBW \frac{\pi}{2}\left(\frac{\lambda_g}{\lambda}\right)^2} \tag{5.2}$$

where J_i' represents the external coupling of the submatrix, J_i is the internal coupling of the coupling matrix M, λ and λ_g are the free-space and guided wavelength, respectively. The index *i* refers to the index of coupling *J*, i.e., *i*=1, 2, …, 6 (see Figure 5.1(a)). In the previous example,

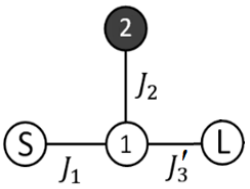

	S	1	2	L
S	0	1	0	0
1	1	-2.770	2.7574	0.1825
2	0	2.7574	-3	0
L	0	0.1825	0	0

(a)

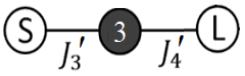

	S	3	L
S	0	0.1825	0
3	0.1825	0	0.1930
L	0	0.1930	0

(b)

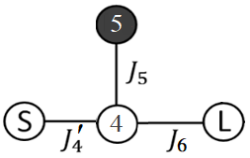

	S	4	5	L
S	0	0.193	0	0
4	0.193	3.096	2.915	1.057
5	0	2.915	3	0
L	0	1.057	0	0

(c)

Figure 5.2 The three subsections of the filter. (a) First subsection including the first resonator and NRN. J3 is changed to J3' using (5.2). (b) Second subsection including the middle resonator. (c) Last subsection.

the value of *i* is set to 3 and 4 to obtain the J_3' and J_4', respectively. Similar process is applied to other subsections, where a resonator is replaced by a port. After obtaining the submatrices, the EM design of each subsection begins in a way that the S parameters deriving from EM simulation must be similar to the S parameters of the submatrix. Finally, all the designed subsections are attached together to create the filter. Figure 5.3(a) shows the filter based on a H-plane configuration for the NRN, using the WR90 waveguide (width: 22.86 mm, height: 10.16 mm). The dominant mode is TE101. Figure 5.4(a) shows the prototype filter, printed using SLM technology. The printing material is an Aluminium alloy, which is made from Al, Cu, Ag, Ti and Mg. The thickness of the structure wall and the iris is set to 2 mm. After the printing process, it is necessary to suck out the unsintered powder. To facilitate this and also to

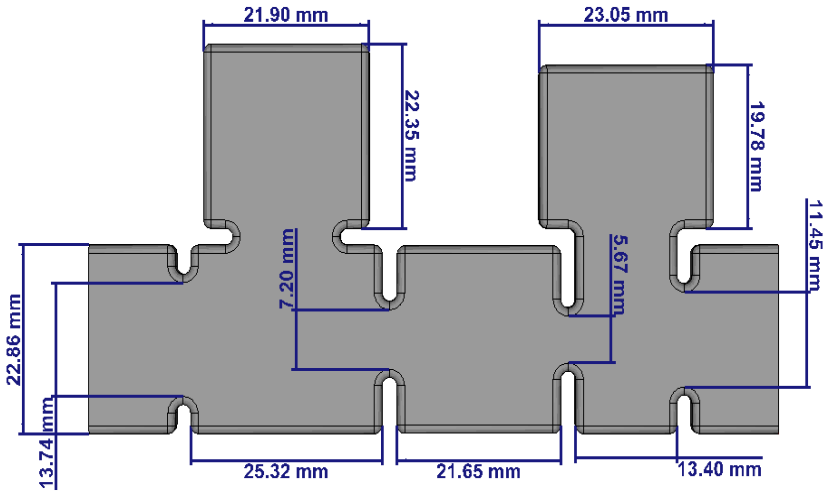
21.90 mm
23.05 mm
22.35 mm
19.78 mm
11.45 mm
7.20 mm
5.67 mm
22.86 mm
13.74 mm
25.32 mm
21.65 mm
13.40 mm

(a)

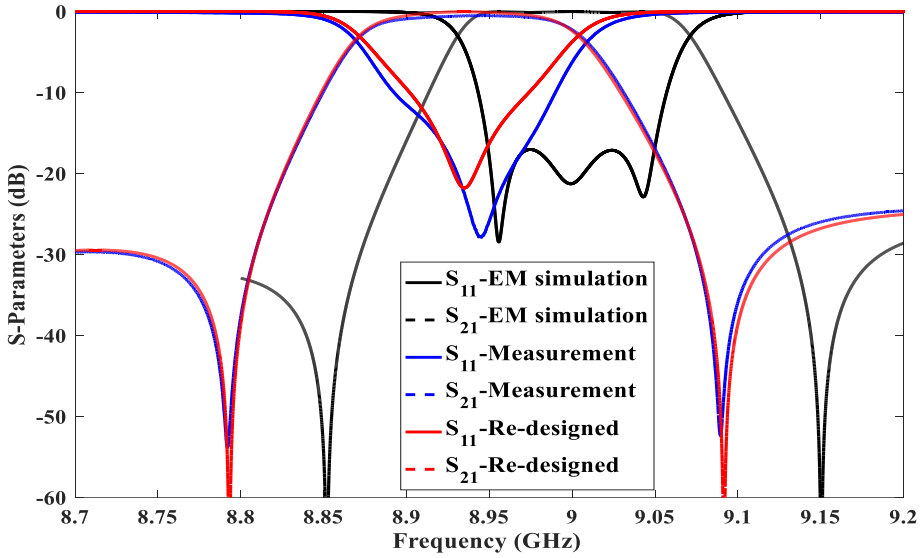
S-Parameters (dB)
Frequency (GHz)
S11-EM simulation
S21-EM simulation
S11-Measurement
S21-Measurement
S11-Re-designed
S21-Re-designed

(b)

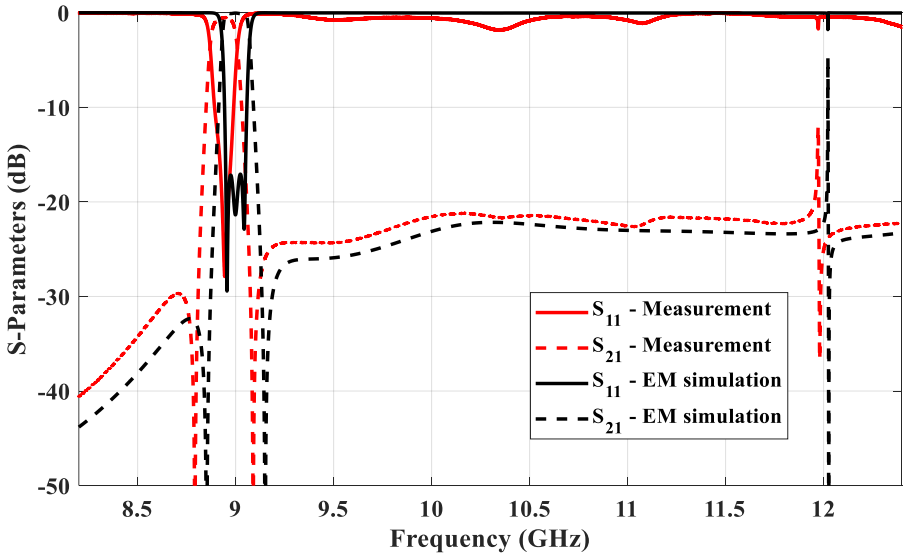
S-Parameters (dB)
Frequency (GHz)
S11 - Measurement
S21 - Measurement
S11 - EM simulation
S21 - EM simulation

(c)

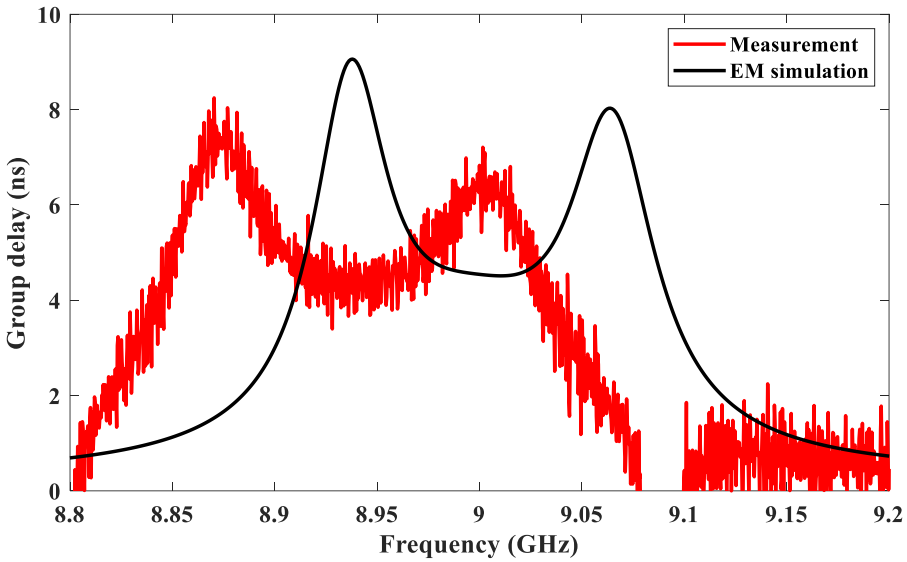

(d)

Figure 5.3 The bandpass filter with two TZs. (a) Simulated filter using CST software. (b) and (c) The measurement results compared with simulations. (d) The group delay measured and compared with simulation.

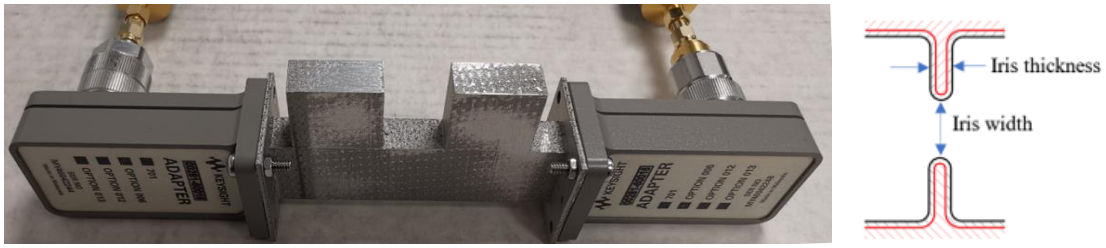

(a) (b)

Figure 5.4 (a) The fabricated structure. (b) The shrinkage effect over an iris section of the filter after fabrication. Black lines: Simulation. Red lines: Fabricated structure. As can be seen, due to the shrinkage, the iris width is increased whilst the thickness is decreased.

reduce the accumulated stress over the structure, corners are rounded with a 1 mm radius. It is also expected the round corners would help with metal coating if required.

5.3 Measurement and discussion

The S parameters of the filter are measured and the results in comparison with the simulation are presented in Figure 5.3(b). The measurement results show a frequency detuning of 60 MHz. This is likely to be due to the printer tolerance as well as the shrinkage after printing. The measure insertion loss within the passband is about 0.52 dB. By comparing the bandwidth and

distance of the TZs from the central frequency between the measured and the simulated, it can be observed that the behaviour of the transmission response is almost identical to the simulation except for a frequency shift. The actual dimensions of the filter are measured using the micro X-Ray CT images post-processing and compared with the design value. The measured cavity hight, cavity width and iris thickness are around 10.22 mm, 22.9 mm and 1.7 mm, respectively. The measured cavities' length and iris' width are 200-300 µm longer and wider than the design. The results show that the cavities' length, irises' thickness and width are more affected during the fabrication. This is likely to be a result of shrinkage, especially for the small and isolated irises. During the printing process, the structure experiences a high-level thermal stress causing structural deformation or shrinkage. Figure 5.4(b) illustrates the possible reason for the smaller iris thickness after fabrication. Such shrinkage seems to be more pronounced around the small iris and can explain the band shift to lower frequency as well as the detuned resonators. The filter is re-designed with 250 µm increase in length of the cavities and 200 µm decrease in the thickness and width of irises in order to consider the shrinkage in the design. The S parameters are obtained and presented in Figure 5.3(b) and Figure 5.3(c). The results show a fair similarity between the re-designed filter and the measurement. The group delay of the filter is measured and compared with the simulation in Figure 5.3(d). The TZs are not appeared on the simulated group delay. This is because of the low resolution, low number of frequency samplings, in the simulation.

In addition to the shrinkage, the effect of printing direction must also be taken into the account. It is important to optimise the printing direction in order to minimise the overhangs as well as the surface roughness. Figure 5.5 shows the printing direction of the device together with the cross-section X-Ray Micro-focus CT scan of the filter. The structure is tilted 45° in order to improve the surface roughness and avoid overhanging in the two dangling resonators. The effect of printing direction on the corners of the structure is visible in Figure 5.5(c). The corners highlighted with red circles are printed along the *x* axis (the laser scanning direction). As a result, the corresponding corners are flatted with large surface roughness. On the other hand,

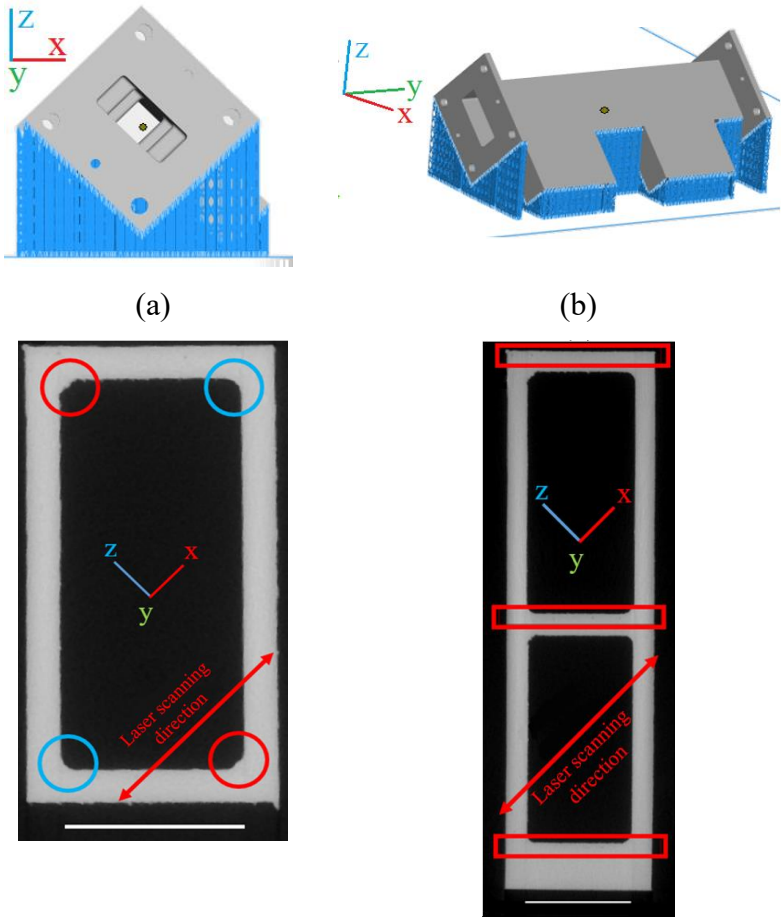

Figure 5.5 (a), (b) Printing direction of the filter. The structure is printed in *z* direction (the staking direction). The blue portions are the supportive structure and removed after fabrication. (c), (d) Cross-section CT scan of the filter. Scale bars equal 10 mm.

the corners highlighted with blue circles, which are printed along the *z* axis, have maintained their round shape. It is also observed that several small, rounded pores are concentrated on specific surfaces (~400 µm below the surface). The red boxes in Figure 5.5(d) indicate regions where pores are observed. Existence of such pores affect the material density.

5.4 Conclusion

In this chapter, a third-order bandpass filter with two TZs is designed using the NRN method and fabricated using the SLM technology. The filter has a centre frequency of 9 GHz with fractional bandwidth of 1.11%, which is relatively challenging for the SLM printing. The results show a 60 MHz frequency shift and resonators detuning. The CT scan of the structure and the dimensional measurements show a structural shrinkage, which can explain the reason of

frequency shifts. Moreover, the images show some pores inside the structure material and some corners, which are flatted due to the printing direction. All of the discussed factors should be considered during the design process in order to minimise the effect of the AM on the performance of microwave devices.

References

[1] A. Mostaani, L. Qian, R. Martinez, P. F. Wilson, M. Attallah, Y, Wang, M. A. Williams, "Investigation of a 3D-Printed Narrowband Filter with Non-Resonating Nodes," *2021 IEEE MTT-S International Microwave Filter Workshop (IMFW)*, 2021, pp. 316-318.

[2] C. Guo, X. Shang, M. J. Lancaster and J. Xu, "A 3-D Printed Lightweight X-Band Waveguide Filter Based on Spherical Resonators," *IEEE Microwave and Wireless Components Letters*, vol. 25, no. 7, pp. 442-444, July 2015.

[3] K. Kotzé and J. Gilmore, "SLM 3D-Printed Horn Antenna for Satellite Communications at X-band," *2019 IEEE-APS Topical Conference on Antennas and Propagation in Wireless Communications (APWC)*, 2019, pp. 148-153.

[4] C. Guo, X. Shang, J. Li, F. Zhang, M. J. Lancaster and J. Xu, "A Lightweight 3-D Printed X-Band Bandpass Filter Based on Spherical Dual-Mode Resonators," *IEEE Microwave and Wireless Components Letters*, vol. 26, no. 8, pp. 568-570, Aug. 2016.

[5] B. Zhang, Y. Guo, H. Zirath and Y. P. Zhang, "Investigation on 3-D-Printing Technologies for Millimeter- Wave and Terahertz Applications," *Proceedings of the IEEE*, vol. 105, no. 4, pp. 723-736, April 2017.

[6] O. A. Peverini, M. Lumia, F. Calignano, D. Manfredi, G. Addamo, M. Lorusso, E. P. Ambrosio, G. Virone, P. Fino, and R. Tascone, "Manufacturing of waveguide components for SatCom through selective laser melting," *2017 11th European Conference on Antennas and Propagation (EUCAP)*, Paris, France, 2017, pp. 563-566.

[7] A. M. Khorasani, I. Gibson, A. H. Ghasemi, and A. Ghaderi, "A comprehensive study on variability of relative density in selective laser melting of Ti-6Al-4V," *Virtual and Physical Prototyping*, vol. 14, no. 4, pp. 349–359, 2019.

[8] J. S. Hong and M. J. Lancaster, *Microstrip Filters for RF/Microwave Applications*. New York, NY, USA: Wiley, 2004.

[9] M. Salek, X. Shang, R. C. Roberts, M. J. Lancaster, F. Boettcher, D. Weber, and T. Starke, "W-Band Waveguide Bandpass Filters Fabricated by Micro Laser Sintering," *IEEE Transactions on Circuits and Systems II: Express Briefs*, vol. 66, no. 1, pp. 61-65, Jan. 2019.

[10] R. J. Cameron, C. M. Kudsia, R. R. Mansour, "Synthesis and Application of Extracted Pole and Trisection Elements," *Microwave Filters for Communication Systems: Fundamentals, Design, and Applications*, Wiley, 2018, pp.323-372.

[11] S. Amari and G. Macchiarella, "Synthesis of inline filters with arbitrarily placed attenuation poles by using nonresonating nodes," *IEEE Transactions on Microwave Theory and Techniques*, vol. 53, no. 10, pp. 3075-3081, Oct. 2005.

[12] C. Tomassoni, O. A. Peverini, G. Venanzoni, G. Addamo, F. Paonessa, and G. Virone, "3D printing of microwave and millimeter-wave filters: Additive manufacturing technologies applied in the development of high-performance filters with novel topologies," *IEEE Microwave Magazine*, vol. 21, no. 6, pp. 24–45, 2020.

[13] J. A. Lorente, M. M. Mendoza, A. Z. Petersson, L. Pambaguian, A. A. Melcon and C. Ernst, "Single part microwave filters made from selective laser melting," *2009 European Microwave Conference (EuMC)*, 2009, pp. 1421-1424.

[14] B. A.-Juboori, J. Zhou, Y. Huang, M. Hussein, A. Alieldin, W. J. Otter, D. Klugmann, and S. Lucyszyn, "Lightweight and Low-Loss 3-D Printed Millimeter-Wave Bandpass Filter Based on Gap-Waveguide," *IEEE Access*, vol. 7, pp. 2624-2632, 2019.

[15] W. J. Otter and S. Lucyszyn, "3-D printing of microwave components for 21st century applications," *2016 IEEE MTT-S International Microwave Workshop Series on Advanced Materials and Processes for RF and THz Applications (IMWS-AMP)*, 2016, pp. 1-3.

[16] X. Shang, W. Xia, and M. J. Lancaster, "The design of waveguide filters based on cross-coupled resonators," *Microwave and Optical Technology Letters*, vol. 56, no. 1, pp. 3–8, 2014.

CHAPTER 6

DESIGN OF NRN BASED FIFTH-ORDER FILTER WITH ONE TRANSMISSION ZERO

Paper published

Abolfazl Mostaani*, Talal Skaik*, Abd El-Moez A. Mohamed**, Moataz M. Attallah**, Paul Booth***, Cesar Miquel-Espana****, Yi Wang*

2023 SBMO/IEEE MTT-S International Microwave and Optoelectronics Conference (IMOC), Castelldefels, Spain, 2023, pp. 58-60, doi: 10.1109/IMOC57131.2023.10379785.

A. Mostaani synthesised and designed the filter and wrote the manuscript. Y. Wang collaborated in writing the manuscript and presented the work at the conference. T. Skaik assisted in the measurements and writing the manuscript. A. E.-M. A. Mohamed and M. M. Attallah fabricated the designed filter. P. Booth and C. M.-Espana shared their technical advice on the design and fabrication process.

* School of Engineering University of Birmingham, Birmingham, U.K.

** School of Metallurgy and Materials, University of Birmingham, Birmingham, U.K.

*** Airbus Defence and Space Ltd Stevenage, U.K.

**** European Space Agency Noordwijk, Netherlands.

This chapter presents a fifth-order bandpass filter for communication satellite feed systems, fabricated using 3D-printing with Titanium alloy Ti-6Al-4V (Ti64). The work is published in [1].

6.1 Introduction

The advent of additive manufacturing (AM) has greatly impacted the microwave engineering industry, particularly in the microwave filters. AM provides a solution to the manufacture of complex and compact waveguide devices with reduced mass and even in a single (monolithic) piece without the need of assembly. In recent years, AM has become increasingly popular for manufacturing microwave filters. However, the high surface roughness is a major drawback in additively manufactured all-metallic parts produced by powder-bed techniques such as selective laser melting (SLM). A monolithically printed part also faces the difficulty with metal-coating of the internal surfaces, especially from those complex enclosed structures. These challenges can lead to high insertion loss (IL) level. Printing accuracy and dimension tolerance are also less known for 3D printed parts. This could cause unpredictable frequency detuning in filters. These issues can be addressed by optimizing the filter structure to cater for printing process and the print orientation [2]-[4]. It is suggested to minimize or eliminate any ceiling surfaces in the filter design as they tend to have poorer surface finish compared to other areas. Various modified resonators and filters are proposed [5]-[7]. It is also crucial to avoid any overhanging elements in the design as they can cause printing failure [2],[8],[9].

The choice of the printing materials not only affect the filter's signal transmission/attenuation but also have a major impact on the filter temperature stability which is a key performance indicator for many high-power filters operating in harsh space environment [7]. Aluminium is widely used for its low density and high conductivity. Invar is used for its low coefficient of thermal expansion (CTE) (1-2 ppm/K versus 21-24 ppm/K for aluminium alloys). Titanium alloy Ti-6Al-4V (or Ti64), not used much in microwave filters, has some interesting material properties that sit between aluminium and Invar. Ti64 is a high strength alloy with excellent corrosion resistance [10]. It has a high strength-to-weight ratio. This allows the manufacture of thin-wall structures with light weight. It has a much lower CTE (around 8.6 ppm/K) than aluminium, which helps maintain its thermal stability over a wide range of temperatures. Ti64 is also one of the most studied materials for additive manufacturing.

In this paper, we investigate the use of Ti64 in printing a filter for satellite feed systems. A modified rectangular resonator is proposed to allow the filter to be printed in a lying-down orientation on the platform without any tilt or internal support. The resonator is used to design a fifth-order filter with one transmission zero (TZ). It is synthesized using the non-resonating node (NRN) method. The filter is fabricated using selective laser melting technology with Ti64, silver coated, and tested. The next sections present the geometry of the resonator, the synthesis and design of the filter and the measured results.

6.2 Concept of the filter

The filter described in this chapter is a fifth-order Chebyshev filter, designed using modified cavity resonators in other minimise the structural support required for the fabrication. Figure 6.1(a) shows the structure of the filter after SLM fabrication and polishing and silver coating process. Looking at Figure 6.1(b), filter is illustrated lying down on the printing platform without any side support structure.

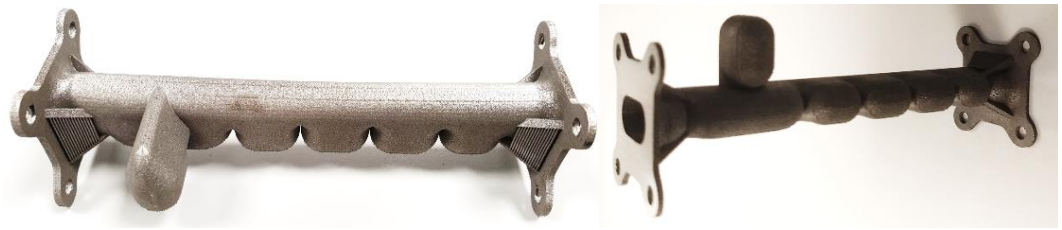

(a)

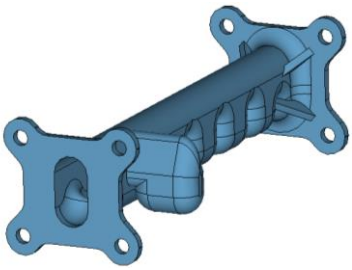

(b)

Figure 6.1 (a) Photographs of the fabricated filters with modified resonator geometry. (b) Illustration of the proposed filter lying down on the printer platform without any side structural support versus a similar filter designed with regular rectangular resonator.

Whilst a similar filter designed using a conventional rectangular resonator must be printed 45° tilted with side wall support during the printing process to avoid an internal rough surface, which ruins the insertion loss. Figure 6.2(a) shows the electric field pattern in a conventional rectangular WR75 resonator with inductive coupling irises attached to the input and output ports. The resonator is designed to resonate at 13.1 GHz with iris widths and thickness of 5.4 mm and 2 mm, respectively. Figure 6.2(b) and Figure 6.2(c) display the proposed modified version also with a dominant TE101 mode and its electric field pattern, respectively.

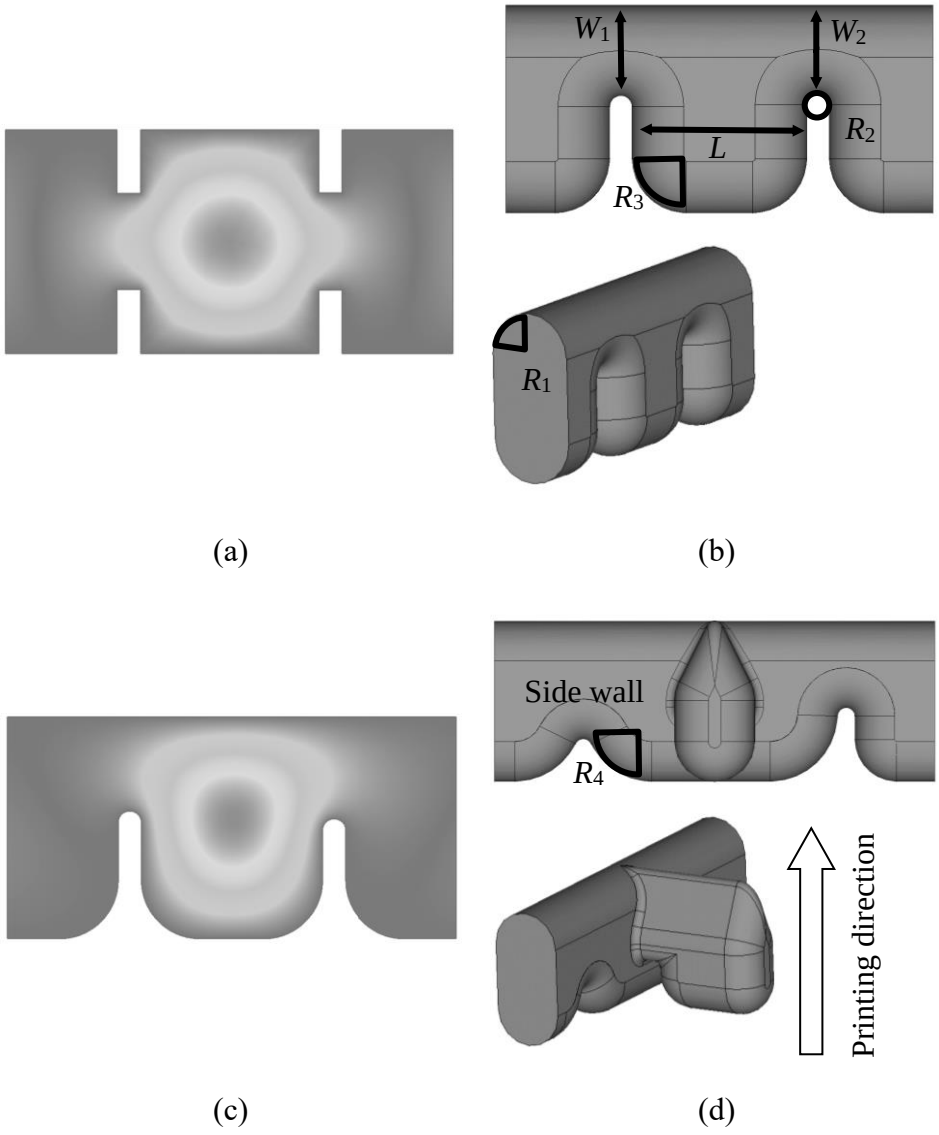

Figure 6.2 (a) E-field pattern in rectangular resonator. (b) and (c) Modified resonator and its E-field pattern. (d) Dangling resonator and the NRN.

The resonator's corners are rounded with radiuses of R_1 = 4.76 mm, R_2 = 1 mm, and R_3 = 5 mm for a smoother surface transition. The rounded corners also facilitate plating and cleaning the printing residue. The coupling irises are shifted to the upper part of the resonator, which reduces the discontinuities along the main waveguide section. This leads to wider irises, which not only reduces the sensitivity to dimensional tolerance but also facilitates the flow of liquid during cleaning, polishing, and coating of the filter. The modified resonator has approximately 50% wider iris and 28% longer length compared to the rectangular resonator. The computed unloaded Q factor (Q_u) of the fundamental mode for the modified resonator is 8540, 16% higher than the rectangular resonator. The dangling resonator attached to an NRN, shown in Figure 6.2(c), and used to generate the TZ, is further modified with a pointed roof of a 60° slope to minimize the ceiling surface, where surface finishing is expected to be worse. R_4 of the NRN is 8 mm. The dangling resonator is attached to the side of the filter. The dangling resonator can also be added to the top of the filter. However, this would increase the height of the part and increases the structure complexity.

6.3 Synthesis, design, and fabrication

The fifth-order filter with a single TZ is synthesized using the NRN method, as outlined in Chapter 2. The specifications of the filter are as follows: its central frequency (f_c) is 13.1 GHz, with a fractional bandwidth (FBW) of 2.4%, and its transmission zero is located at 11.7 GHz. Its return loss (RL) is set to 23 dB. The topology of the filter is depicted in Figure 6.3, and the corresponding coupling matrix is given in (6.1).

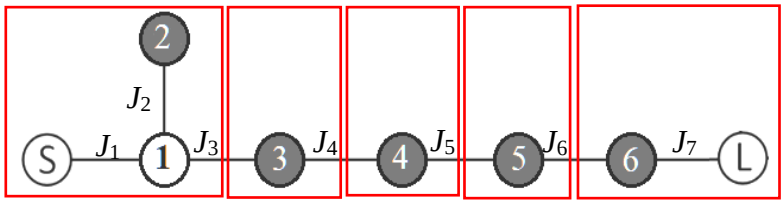

Figure 6.3 The fifth-order filter with one TZ, divided into five sections as boxed with red lines. The resonators are represented by dark circles and the NRNs by white circles.

$$M = \begin{bmatrix} 0 & J_1 & 0 & 0 & 0 & 0 & 0 & 0 \\ J_1 & b_1 & J_2 & J_3 & 0 & 0 & 0 & 0 \\ 0 & J_2 & b_2 & 0 & 0 & 0 & 0 & 0 \\ 0 & J_3 & 0 & b_3 & J_4 & 0 & 0 & 0 \\ 0 & 0 & 0 & J_4 & b_4 & J_5 & 0 & 0 \\ 0 & 0 & 0 & 0 & J_5 & b_5 & J_6 & 0 \\ 0 & 0 & 0 & 0 & 0 & J_6 & b_6 & J_7 \\ 0 & 0 & 0 & 0 & 0 & 0 & J_7 & 0 \end{bmatrix} \tag{6.1}$$

where, J_1=1, J_2=1.78, J_3=0.87, J_4=0.68, J_5=0.66, J_6=0.93, J_7=1.08, b_1=1.54, b_2=2.19, b_3=-0.04, b_4=-0.07, b_5= -0.03, b_6=-0.02. The design of the filter employs the step-tuning technique, where the filter topology is divided into five sections, as depicted in Figure 6.3. Correspondingly, the coupling matrix is divided into five sub-matrices, shown in Figure 6.4. It is noteworthy that each section may have one or two internal couplings that are converted to external couplings. For example, in Figure 6.4(b), J_3 and J_4 in Figure 6.3 are transformed into J_3' and J_4' using (6.2).

$$J_i' = J_i \times \sqrt{FBW \frac{\pi}{2} \left(\frac{\lambda_g}{\lambda}\right)^2} \tag{6.2}$$

where J_i' represents the external coupling of the submatrix, J_i is the internal coupling of the coupling matrix, λ and λ_g are the free-space and guided wavelength, respectively. The diagonal elements of the submatrix, which represent the self-coupling of either the resonators or ports, are also adjusted. For instance, in the case of Figure 6.4(b), the diagonal elements corresponding to *S* and *L* are set to zero. This same process is applied to the other subsections. The design of each subsection is carried out utilizing CST Microwave Studio whereby the physical dimensions are optimized such that the S parameters match those obtained from the corresponding coupling submatrix. Finally, the five subsections are joined together, and a further optimization is carried out. The *S* parameter results of the designed filter and its comparison with the coupling matrix are shown in Figure 6.5. The optimized dimensions of the filter are: L_1=29.3 mm, L_2=16.4 mm, L_3=14.9 mm, L_4=15.9 mm, L_5=15.7 mm, L_6=13.9 mm, W_1=14 mm, W_2=12.2 mm, W_3=10.6 mm, W_4=8.5 mm, W_5=8.5 mm, W_6=9 mm, W_7=11.6 mm. Iris thickness is set to 2 mm.

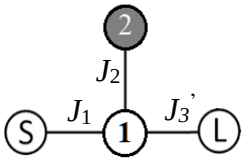

	S	1	2	L
S	0	1	0	0
1	1	1.5422	1.7806	0.2097
2	0	1.7806	2.1935	0
L	0	0.2097	0	0

(a)

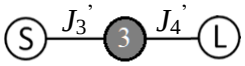

	S	3	L
S	0	0. 2097	0
3	0. 2097	-0.036	0.1645
L	0	0.1645	0

(b)

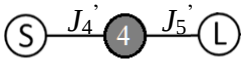

	S	4	L
S	0	0.1645	0
4	0.1645	-0.071	0.1590
L	0	0.1590	0

(c)

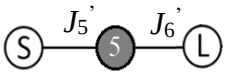

	S	5	L
S	0	0.1590	0
5	0.1590	-0.032	0.2242
L	0	0.2242	0

(d)

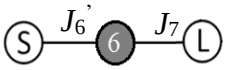

	S	6	L
S	0	0.2242	0
6	0.2242	-0.023	1.0772
L	0	1. 0772	0

(e)

Figure 6.4 The five subsections of the filter. (a) First subsection, comprising the NRN-1 and resonator-2. (b)-(e) represent the rest of the resonators.

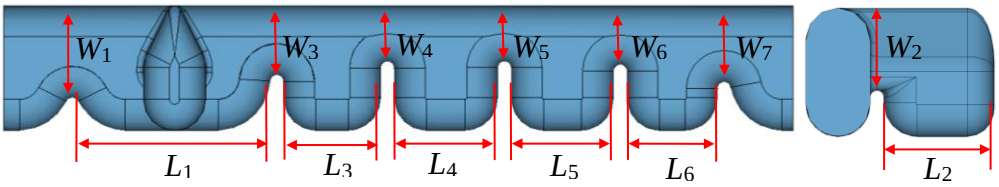

(a)

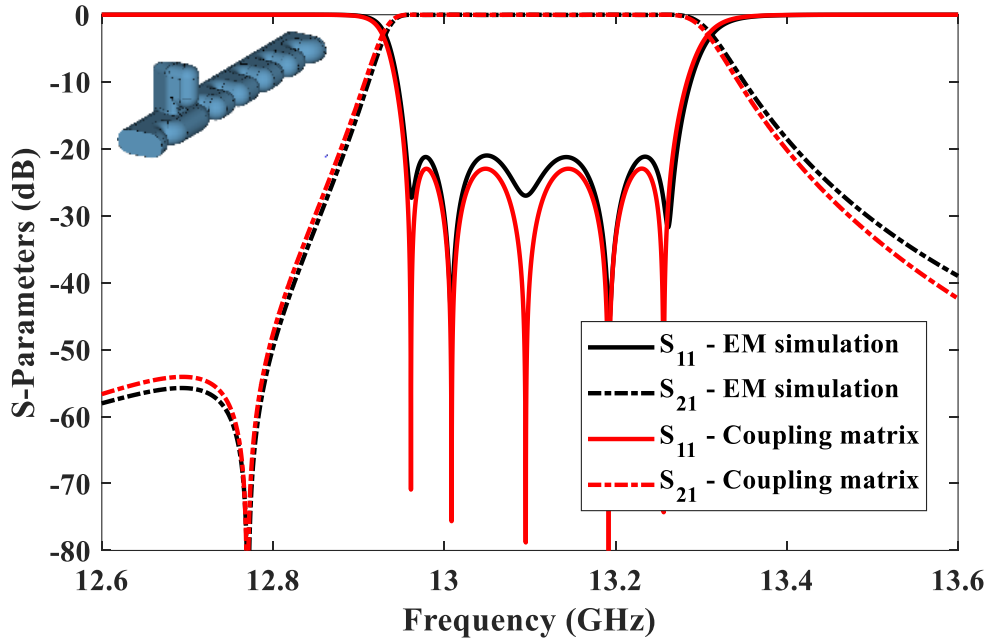

(b)

Figure 6.5 Filter design. (a) Air model with perfect electric conductor walls. (b) Comparison of EM simulations with the responses from the coupling matrix.

6.4 Measurement and discussion

The filter was fabricated from a pre-alloyed Ti64 powder using SLM technique using a Reinshaw 500 printer. The printing orientation and picture of the printed structure are shown in Figure 6.6(a) and Figure 6.6(b), respectively. The tolerance analysis is performed on the designed model. The dimensional offset over resonator length and iris width are set to ±400 µm and ±200 µm, respectively. The results are displayed in Figure 6.6(c), in which the S_{11} graph tends to shift more towards higher frequency ranges. By exploiting Ti64's high strength-to-weight ratio, the filter wall thickness was set to 1mm, achieving a lightweight filter design. The

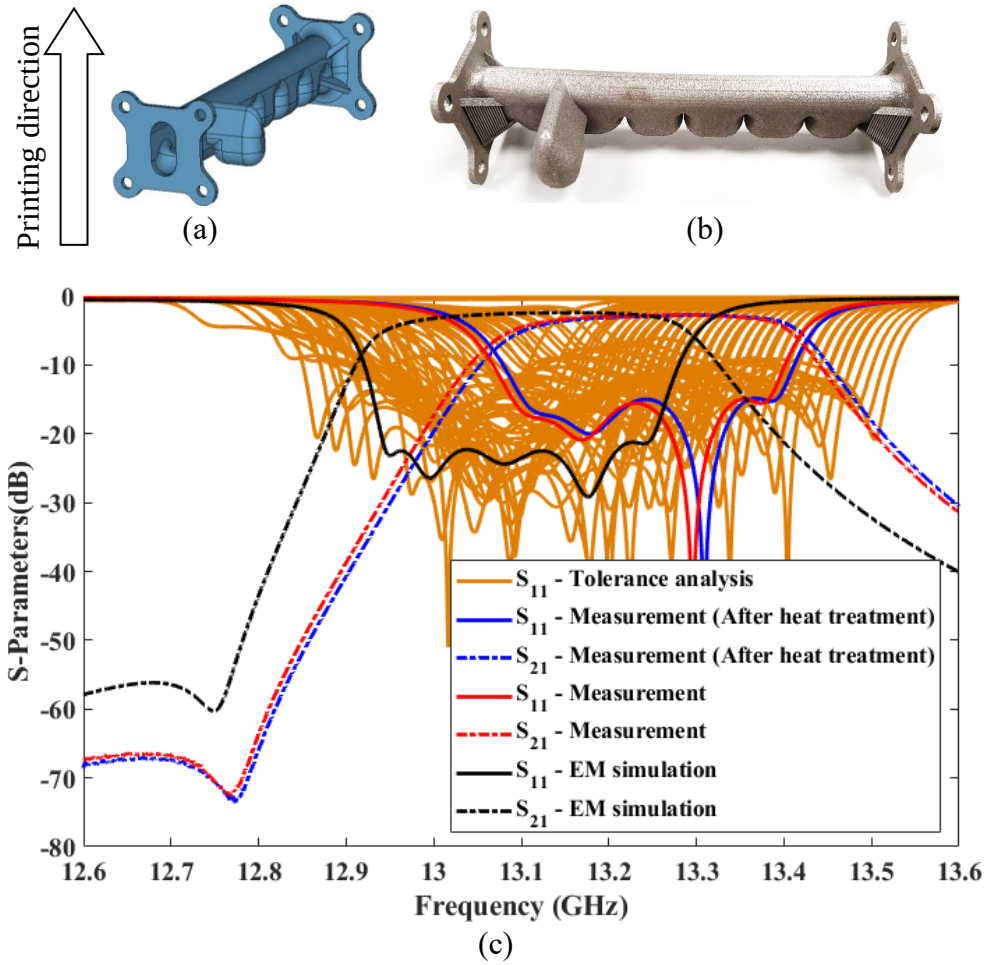

Figure 6.6 3D-printed Ti64 filter and measurements. (a) Printing orientation. (b) Picture of the fabricated filter. (c) Tolerance analysis together with measurement results before and after heat treatment, compared with the EM simulation.

filter weighs 40 g. The filter was printed with a laser power of 200 W, scan speed of 1500 m/s, exposure time of 60 µs and point distance of 90 µm. After the fabrication, the filter was chiselled from the substrate and polished for 6 hours using a Sharmic vibrator filled with silica particles. The filter is cleaned in ultrasonic ethanol bath for 1 hour. Then, the filter was exposed to a thermal treatment to release thermal stresses accumulated during the build. The heat treatment was at vacuum with a heating rate of 10° C/min from room temperature to 600° C, hold for 1 hour and then cool down to room temperature with a cooling rate of 10° C/min. We measured the S parameters of the filter before and after heat treatment. As shown in Figure 6.6(c), after the treatment, the response shifts upward and to the rights very slightly. The average surface roughness of a block printed out of Ti64 is measured as 7 µm. This is used to obtain the alloy's effective conductivity, which is 1.9×10^5 S/m. Using this effective conductivity in the

simulation, a minimum IL of 2.4 dB is obtained as shown in Figure 6.6(c). This is reasonably close to the measured minimum IL of 2.7 dB. The measurements show a frequency shift of 140 MHz towards higher frequency. The location of the TZ, however, is in close agreement with the design. Plating on Ti64 is a more involved process than plating on aluminium or Invar. It is anticipated the dangling resonator is not easily accessible by the plating solution as it is attached to the side of the filter. This is later confirmed by inspecting the dissected filter. We have investigated the effect of the un-plated side resonator. As shown in Figure 6.7(a), three scenarios are simulated and compared: (1) Ti64 as the conductor ('uncoated'); (2) Filter fully coated with silver ('fully coated'); (3) All but the dangling resonator coated ('coated'). It can be observed that the partial coating increases the IL slightly. The impact on the lower band edge is more pronounced, with a 0.5 dB increase. The effective conductivity of the corresponding materials, i.e., 1.9×10^5 S/m for Ti64 and 1.6×10^7 S/m for silver, is used in the three simulations. The effective conductivity of the silver is obtained using the average internal-surface roughness, which is measured as 4.4 μm after dissection.

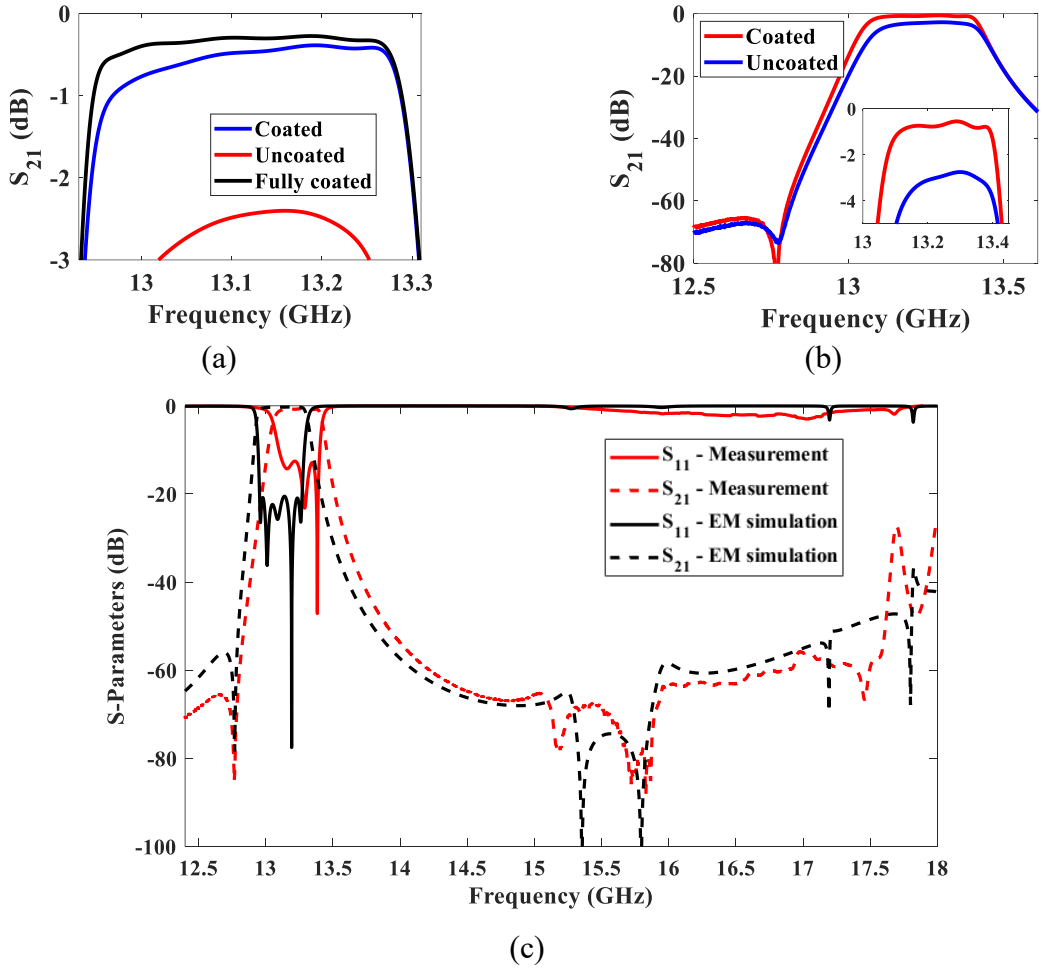

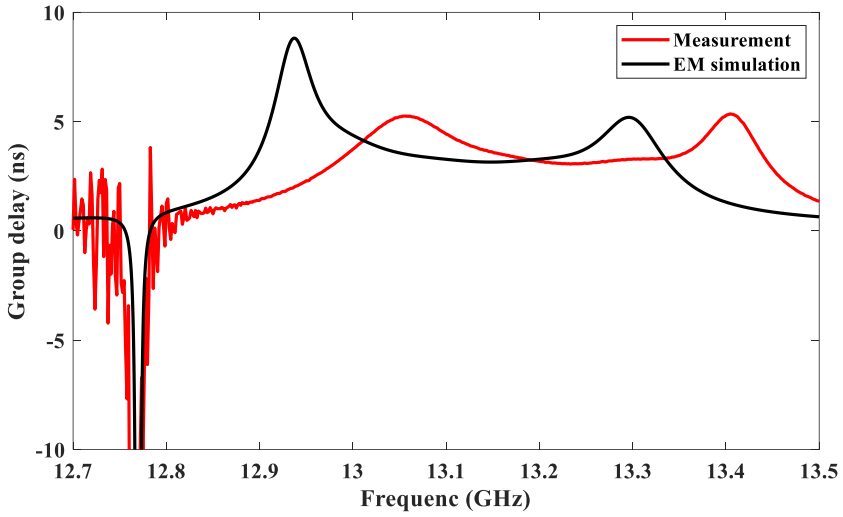

(d)

Figure 6.7 (a) Investigation of the effect of partial silver plating on the Ti64 filter. (b) Measurement results of the silver-coated filter compared with the uncoated version. (c) The measured S parameters over the wide band frequency range compared with simulation. (d) The measured group delay compared with the simulation.

The Ti64 filter is plated with silver and re-measured. In Figure 6.7(b), measurement shows the minimum insertion is significantly reduced to 0.55 dB from 2.7 dB. However, this is still 0.16 dB higher than the predicted IL of a partially coated filter (Figure 6.7(a)). The S parameters of the coated filter are measured over the wide frequency range and compared with the EM simulation in Figure 6.7(c). The measured group delay compared with the simulation is shown in Figure 6.7(d), which clearly shows the frequency shift after fabrication. Attempt to add tuning screws failed due to the difficulty in drilling on the curved Ti64 wall. Instead, we have done simulation-based analyses to identify the cause of the frequency. Because the location of the transmission zero is correct, we assume the dangling resonator's dimensions are as expected. We adjust the in-line resonators to try to match the measured responses. As shown in Figure 6.8, simply reducing the length of L_1, L_3, L_4, L_5 by 0.25 mm and L_6 by 0.2 mm would match the simulation result very well with the measurement. The actual dimension errors are more complex and harder to ascertain from the curved cavities. However, the analyses seem to suggest the main errors lie in the in-line resonator, likely along the length direction. The filter was halved using electrical discharge machining (EDM) to measure surface roughness and to examine the surface finish and quality of the silver coating. One half of the filter, along with

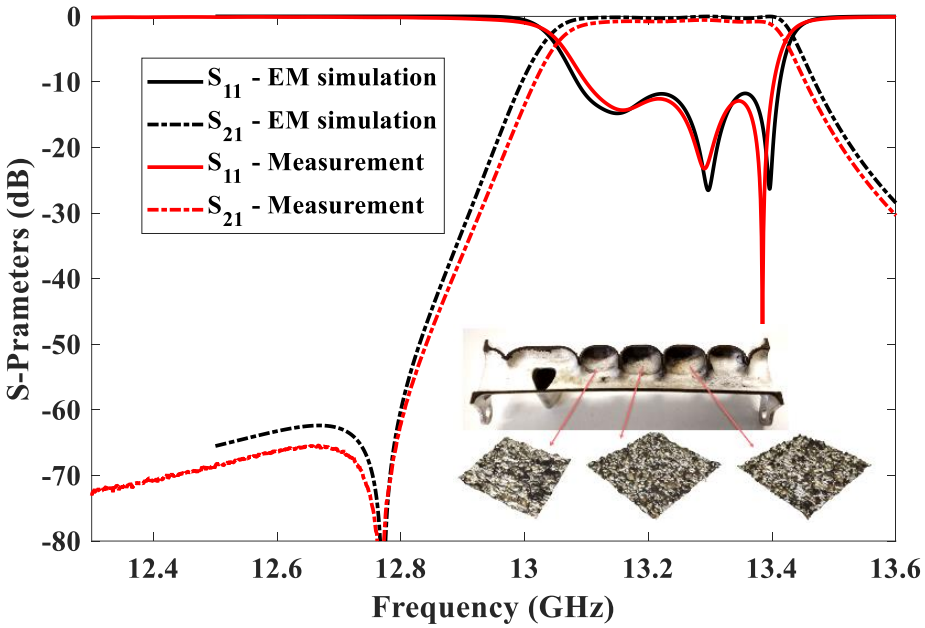

Figure 6.8 Fitting of the measurement response with the simulation by reducing L_1, L_3, L_4, L_5 by 0.25 mm and L_6 by 0.2 mm. The inset: Dissected half of the filter with the surface roughness profile from three cavities.

the surface roughness profiles, captured using Alicona optical system for three resonators, is depicted in the inset image of Figure 6.8. Upon closer inspection of the dissected parts, the silver coating appeared suboptimal in the lower parts of the cavities, resulting in dark spots visible in the inset image of Figure 6.8 due to the Ti64 background being partially uncovered by silver. This could be the cause of the 0.16 dB higher IL than the simulation.

6.5 Conclusion

The chapter investigates the application of Titanium alloy Ti64 in satellite-feed-system filters. A fifth-order filter is designed using modified resonators and iris alignment, offering a continuous ceiling surface and 50% wider iris. The modified resonator provides a 16% higher Q_u factor and 28% longer cavity compared to a rectangular resonator. It enables filters to be printed lied down on the printer platform without any internal support. The filter was fabricated using SLM technology with Ti64, with a thin 1 mm wall thickness with a light weight of 40 g. The filter was coated in silver to improve the IL by 2.15 dB to 0.55 dB, which is still 0.16 dB

higher than the simulation. The S parameters show a 140 MHz frequency shift, and a simulation matched with the measurement indicates that a 0.2-0.25 mm reduction in the length of the inline resonators may be the cause. The filter is halved, and inspections reveal a suboptimal silver coating on the bottom of cavities and the dangling resonator. The low-quality silver coating contributes to the 0.16 dB higher IL compared to the simulation.

References

[1] A. Mostaani, T. Skaik, A. E. -M. A. Mohamed, M. M. Attallah, P. Booth, C. M. -Espana and Y. Wang, "A 3D-Printed Monolithic Inline Filter Fabricated With Titanium Alloy," *2023 SBMO/IEEE MTT-S International Microwave and Optoelectronics Conference (IMOC)*, Castelldefels, Spain, 2023, pp. 58-60.

[2] M. Salek, X. Shang, R. C. Roberts, M. J. Lancaster, F. Boettcher, D. Weber, and T. Starke, "W-Band Waveguide Bandpass Filters Fabricated by Micro Laser Sintering," *IEEE Transactions on Circuits and Systems II: Express Briefs*, vol. 66, no. 1, pp. 61-65, Jan. 2019.

[3] G. Strano, L. Hao, R. M. Everson, K. E. Evans, "Surface roughness analysis, modelling and prediction in selective laser melting," *Journal of Materials Processing Technology*, vol. 213, no. 4, pp. 589-597, 2013.

[4] M. Simonelli, Y.Y. Tse, C. Tuck, "Effect of the build orientation on the mechanical properties and fracture modes of SLM Ti–6Al–4V," *Materials Science and Engineering: A*, vol. 616, pp. 1-11, 2014.

[5] G. Venanzoni, M. Dionigi, C. Tomassoni, D. Eleonori and R. Sorrentino, "3D printing of X band waveguide resonators and filters," *2017 XXXIInd General Assembly and Scientific Symposium of the International Union of Radio Science (URSI GASS)*, Montreal, QC, Canada, 2017, pp. 1-2.

[6] P. Vaitukaitis, K. Nai, J. Rao and J. Hong, "On the Development of Metal 3D Printed Bandpass Filter with Wide Stopband Based on Deformed Elliptical Cavity Resonator with an Additional Plate," *IEEE Access*, vol. 10, pp. 15427-15435, 2022.

[7] L. Qian, Y. Wang, S. Li, A. E.-M. A. Mohamed, M. M. Attallah, T. Skaik, P. Booth, L. Pambaguian, C. M. España, and P. M.-Iglesias, "A Narrowband 3-D Printed Invar

Spherical Dual-Mode Filter With High Thermal Stability for OMUXs." *IEEE Transactions on Microwave Theory and Techniques*,70, no. 4 (2022): 2165-2173.

[8] T. Skaik, M. Salek, P. Hunyor, H. Wang , P. G. Huggard, P. F. Wilson, M. A. Williams, and Y. Wang, "Evaluation of 3D Printed Monolithic G-band Waveguide Components," *IEEE Transactions on Components, Packaging and Manufacturing Technology*, vol. 13, no. 2, pp. 240-248, Feb. 2023.

[9] R. V. Snyder, G. Macchiarella, S. Bastioli and C. Tomassoni, "Emerging Trends in Techniques and Technology as Applied to Filter Design," *IEEE Journal of Microwaves*, vol. 1, no. 1, pp. 317-344, Jan. 2021.

[10] P. Manfred, J. Kumpfert, C. H. Ward, and C. Leyens. "Titanium alloys for aerospace applications." *Advanced engineering materials* 5, no. 6, Jun. 2003, pp. 419-427.

CHAPTER 7

COMPACT SELF-SUPPORTIVE FILTERS SUITABLE FOR ADDITIVE MANUFACTURING

Paper published

Abolfazl Mostaani*, Yi Wang*, Lu Qian*, Abd El-Moez A. Mohamed**, Moataz M. Attallah**, Talal Skaik*

IEEE Transactions on Components, Packaging and Manufacturing Technology, doi: 10.1109/TCPMT.2023.3332678.

A. Mostaani proposed the geometry for the resonators and synthesised and designed the filters and wrote the manuscript in collaboration with Y. Wang. L. Qian and T. Skaik assisted in the measurements. A. E.-M. A. Mohamed and M. M. Attallah fabricated the designed filters.

* School of Engineering University of Birmingham, Birmingham, U.K.

** School of Metallurgy and Materials, University of Birmingham, Birmingham, U.K.

This chapter an irregular-hexagonal resonator geometry is proposed for additively manufactured microwave filters. The work is published in [1].

7.1 Introduction

The emergence of additive manufacturing (AM, also known as 3D-printing) was a turning point in the manufacturing industries due to its unique capability of building complex structures with reduced need of assembly or even in one piece. In microwave engineering, AM offers a promising solution to the increasing demand for more compact, complex, and lighter structures, especially in satellite communicating systems. One widely used device that has benefited most from the new manufacturing technique is the filter. In recent years, there are numerous studies on high performance filters and multiplexers fabricated using various AM technologies such as fused deposition modelling (FDM) [2],[3], polyjet printing [4], stereolithographic apparatus (SLA) [5],[6] and selective laser melting (SLM) [7]-[11].

While 3D printing brings about many innovation opportunities in filter design and manufacture, it is not a technology without challenges. The printability and the printing quality are highly dependent on the relationship between the geometry and printing direction. Figure 7.1 illustrates the formation of the internal surfaces, which often concern microwave parts most, from the layer-by-layer manufacture process using the SLM as an example. The staircase effect makes the 3D printed surfaces much rougher than machined surfaces. The up-skin areas face along the printing direction, whereas the down-skin areas face against the printing direction. The down-skin surfaces form on un-sintered powder in SLM so they have higher surface roughness. These are also referred to as the overhang, described by the angle θ_d. To ensure the integrity of the structure, this angle should normally be kept below 45° [12]. The larger the overhang angle is, the rougher the down-skin surface will be. For microwave filters where surface roughness significantly impacts the insertion loss, θ_d is preferred to be less than 30°. The region marked out as ‘E’ in Figure 7.1, with large overhang angles, should really be avoided. The region B, with a large angle θ_d but in the up-skin area, can be readily formed with good quality but the staircase effect would make the hatch pattern of the laser visible on the surface. One of the main considerations in designing such filters for 3D printing is to avoid or minimize the overhang problems, avoid excessive surface roughness and therefore reduce the risk of structural failure or significant performance degradation [13]-[16].

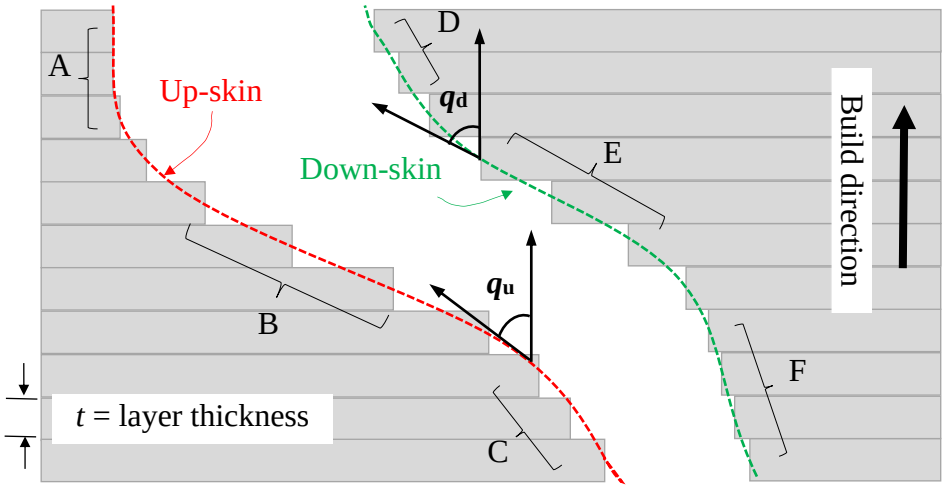

Figure 7.1 An illustration of the surface texture/roughness in relation to build orientation, θ_u and θ_d, for the up-skin and down-skin surfaces.

Figure 7.2 Some typical self-supportive cavity structures used in 3D printing.

This makes self-supportive geometries highly desirable for cavity resonators/filters. Some of these geometries can be found in Figure 7.2. The rounded structures are good choice. But the north- pole area may be modified to avoid any flat ceiling structure. The self-supportive geometries also give the opportunity to design filters to be printed vertically, which saves footprint on the printing platform for more parts to be printed in one go. One caveat is the moderately increased risk in building tall structures when instability of the printer platform during long print could disrupt or fail the parts. So, it is often desirable to design the structures as compact as possible in both scanning (horizontal) and printing (vertical) directions. In [17], a filter based on spherical resonators is printed vertically using SLM technology. The resonators are stacked upon each other. The ceiling of the spheres is removed to create the coupling irises while avoiding overhangs. If the spheres are staggered sideway, the pole ceiling may have to be modified. The triangular resonator [17] is good for printing but not the most suitable for

stacking up. Conventional rectangular resonators must be tilted in printing, e.g., by 45˚. The rhombus shape resonator with $\theta_d < 45^\circ$ offers a good balance in the printability, internal surface finishing and flexibility to create a compact stack and layout. The adjacent resonators can be attached diagonally rather than on top of each other. As with the triangular shape, it has sharp corners which may present some difficulties with surface coating, if required.

In this chapter an irregular-hexagon shaped resonator is proposed and used. This structure reduces the overhangs and enhance the printability and modularity of the filters. The geometry allows closely packed resonators laid out in a low profile and in various topologies to realize transmission zeros in the transfer function. It also enables the filters to be printed in a vertical sitting direction along the direction of the ports, without requiring any internal support structures and without the need of tilting the build as in many rectangular cavity-based filters. The resonator structures and the filters formed of them are highly suitable for 3D printing.

7.2 Resonator geometry

First, we will introduce the self-supportive resonator structure for 3D printing. Figure 7.3(a) shows the primary model of the resonator. The resonator side walls are narrowing towards the ceiling at a slope angle, θ_d against the vertical axis. This angle is adjustable but preferentially set at 30˚ to reduce the risk of overhang-associated excessive surface roughness [19]. The side walls are also narrowing at an angle of θ_u towards the bottom of the resonator. This angle can be more flexibly chosen but set to be equal to θ_d in order to create a symmetric geometry. Similar resonator is presented in [20], in which the resonators not only have sharp corners but also stack on top of each other. In this work, the sharp corners are rounded, and the resonators are staggered to make a very compact layout and to realize transmission zeros using dangling nodes, while still being printed vertically with minimum overhang. Figure 7.3(b) shows the resonator with corners rounded by R_1=1 mm, R_2=5 mm and R_3=5.08 mm. The modified resonator structure is shown in Figure 7.3(c). Its Q_u for the first two modes is compared with two other variations (with different θ_d values) and the rectangular resonator in Table 7.1.

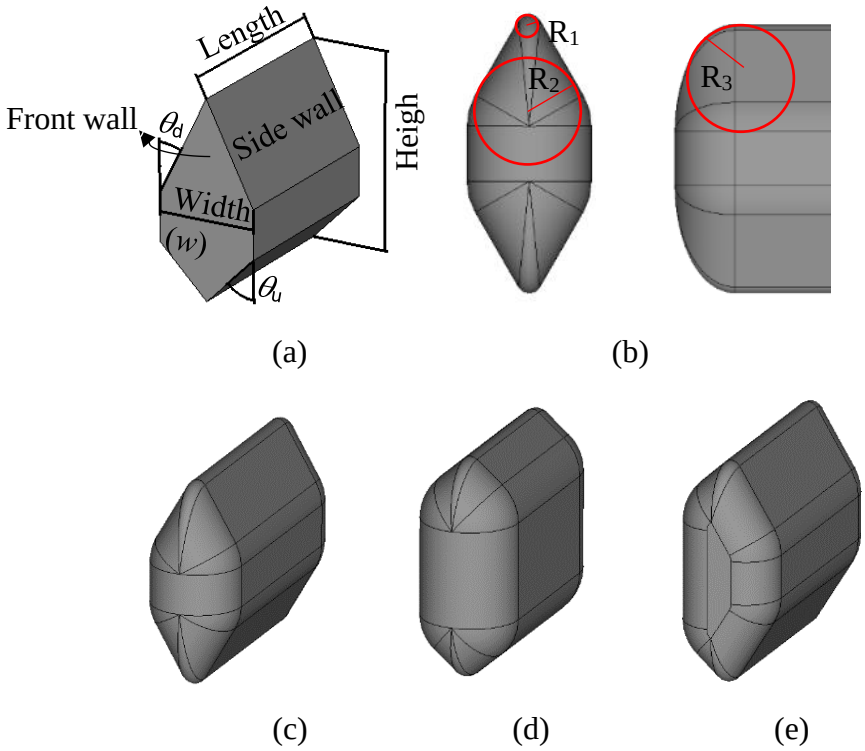

Figure 7.3 (a) Primary and (b) modified model of the proposed resonator. (c), (d), (e): Three types of resonators with varying θ_d of 30˚, 45˚ and mixed 30˚/45˚.

Table 7.1 Resonant frequency and Q_u comparison between the proposed resonators and rectangular resonator

	Resonant frequency (GHz) / Q_u			
θ_d	**30˚**	**45˚**	**30˚/45˚**	**Rec.**
Mode 1	10/7007	10/8562	10/7848	10/7794
Mode 2	13.1/9153	14.9/10865	15/9850	15.1/9749

All resonators are designed to have their fundamental resonant mode at 10 GHz. The Q_u of the proposed resonator with θ_d = 30˚ is 10% lower than the rectangular resonator. The lower Q_u could be caused by the fact that the 60˚ side wall slope (θ_d = 30˚) creates sharper sides in the cavity. This confines the field and increases the current density. This reduces the efficiency of the resonator and lead to a lower Q_u factor compared to cavity resonators with smooth, rounded geometries. The sharp corners in a cavity resonator can also encourage the excitation of higher-order modes in the resonator. The volume and length of the resonator is also 4.8% and 66% bigger than the rectangular version, respectively. The Q_u can be increased by increasing the θ_d to 45˚ (Figure 7.3(d)).

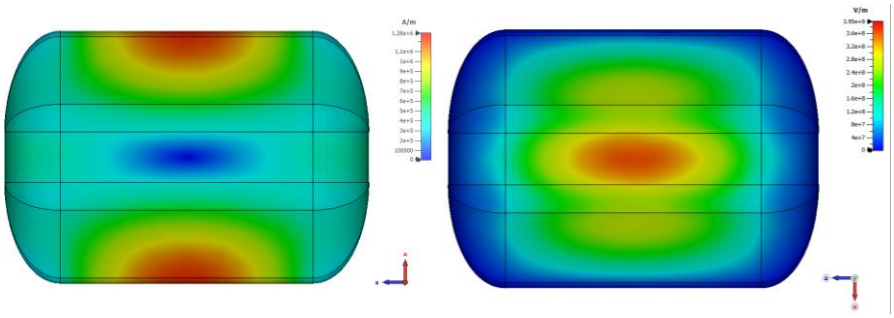

(a) (b)

Figure 7.4 Field patterns of the proposed hexagonal resonator with $\theta_d = \theta_u = 30^\circ$. (a) H-field. (b) E-field.

However, this would reduce the finishing quality of the internal downward surfaces. It would also increase the total height of the filters, which may be unfavourable as the increased printing height also means more powder to fill the printer tank as well as increased risk of instability. A resonator with a mixed θ_d of 30˚ and 45˚ (Figure 7.3(e)) could offer slightly higher Q_u than the rectangular resonator. This geometry may be suitable for inline filters but becomes inconvenient when dangling resonators are used. On balance, we have adopted θ_d as 30˚ for the resonators in the designs. Its electrical and magnetic fields patterns are displayed in Figure 7.4. Figure 7.5(a) and (b) show a single resonator coupled to two ports and is compared with its counterpart rectangular resonator. An elliptic coupling iris is used as shown in Figure 7.5(c). The coupling can be adjusted by changing the major and minor axes of the ellipse. The ports are based on WR90 waveguide. For both source and load irises, d_1 and d_2 are 9.8 mm and 6 mm, respectively. For the hexagonal resonator, l is 28 mm. h and w are equal to the standard WR90 waveguide, i.e., 22.86 mm and 10.16 mm, respectively. For the regular rectangular resonator, h is 16.9 mm. The rest of the dimensions are based on WR90. The source and load irises' length and width are 8.9 mm and 10.16 mm, respectively. The proposed resonator has a higher cut-off frequency, but slightly lower second-order mode frequency compared with the rectangular resonator. The compactness of the hexagonal resonator is evident as shown in Figure 7.5(b). The resonator can be printed vertically, unlike the conventional rectangular resonators, which must be printed with a 45˚ tilt. Cross-coupling extracted pole and non-resonating nodes can all be implemented using the proposed resonator model. In this work, the non-resonating node designs are chosen.

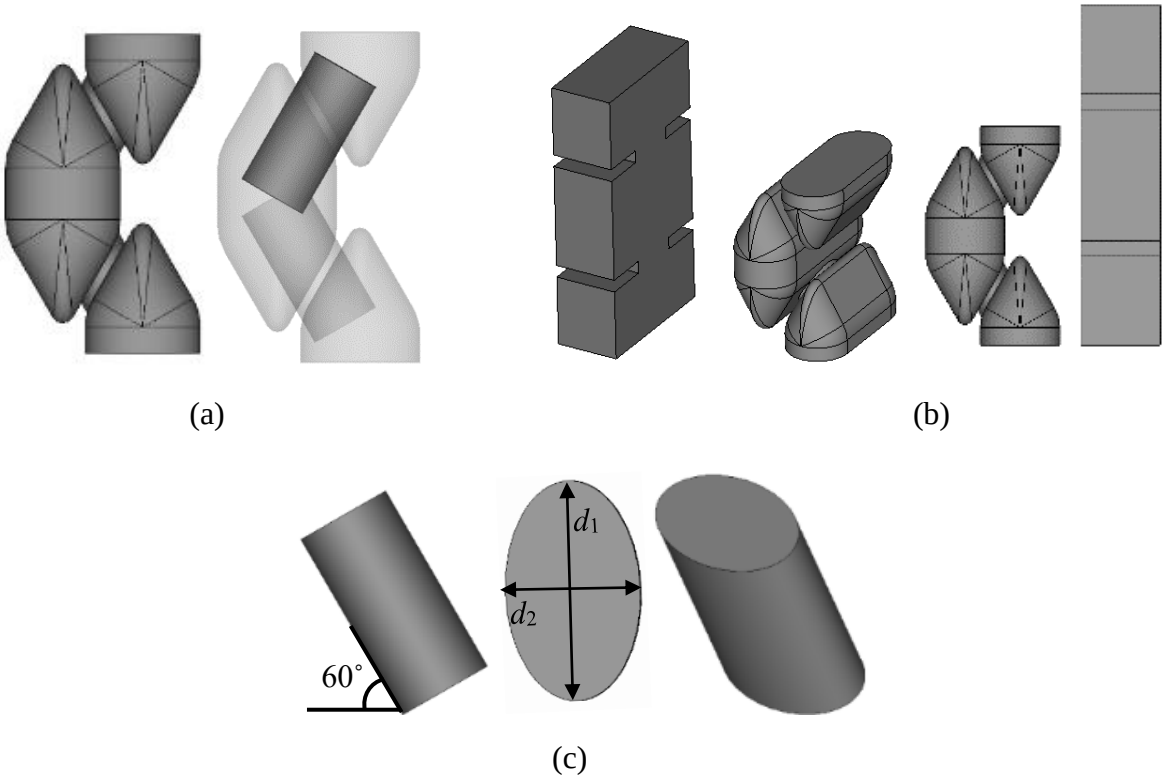

Figure 7.5 A single resonator and the coupling structure. (a) Side view. (b) Comparison with a rectangular resonator that has the same resonance frequency and loaded *Q*. (c) The elliptical iris structure.

7.3 Synthesis, design, and fabrication of filters

Three bandpass filters, narrowband and wideband, are designed and fabricated to demonstrate the capability of the proposed resonators over the rectangular resonators. They are fabricated with aluminium-copper alloy (A20X) using Concept Laser M2 based on selective laser melting (SLM) printing technology. The fabricated filters are polished using vibratory grinding machine to reduce the surface roughness. The measured typical surface roughness and the nominal electrical conductivity of A20X are around 3.5 μm and 1.9×10^7 S/m, respectively. These are used to obtain the effective conductivity, which is around 0.56×10^7 S/m and used in the simulations to obtain insertion loss. The first and second designs are a third-order filter each with two transmission zeros realized using dangling nodes. The filters are different in their bandwidth (1% and 5% FBW) and topology. Both filters are designed using the non-resonating node method [21],[22]. The third design is a third-order Chebyshev filter.

7.3.1 A third-order wideband filter with two transmission zeros

Figure 7.6 shows a third-order filter topology with two transmission zeros (TZs) together with its equivalent circuit model. The specification of the filter is: f_c = 10 GHz, BW = 500 MHz, Return loss (*RL*) = 20 dB, and TZs at 9.25 GHz and 10.75 GHz. The filter is synthesised using the non-resonating node method and the values of circuit elements in Figure 7.6(b) are obtained as $J_1 = 1$, $J_2 = 2.5285$, $J_3 = 1$, $J_4 = 2.8878$, $J_5 = 1.1078$, $J_6 = 1.0685$, $b_1 = 2.0154j$, $b_2 = 3j$, $b_3 = -3.1887j$, $b_4 = -3j$ and $b_5 = -0.3411j$. All the capacitances are normalized to 1. The coupling matrix is acquired from the circuit elements and presented in (7.1).

$$\begin{bmatrix} 0 & 1 & 0 & 0 & 0 & 0 & 0 \\ 1 & 2.0154 & 2.5285 & 1 & 0 & 0 & 0 \\ 0 & 2.5285 & 3 & 0 & 0 & 0 & 0 \\ 0 & 1 & 0 & -3.189 & 2.8878 & 1.1078 & 0 \\ 0 & 0 & 0 & 2.8878 & -3 & 0 & 0 \\ 0 & 0 & 0 & 1.1078 & 0 & -0.341 & 1.0685 \\ 0 & 0 & 0 & 0 & 0 & 1.0685 & 0 \end{bmatrix} \tag{7.1}$$

The filter is designed using the step-tuning technique, in which the filter's topology is divided to three subsections (Figure 7.6(a)), whose corresponding coupling matrices are extracted from the main coupling matrix in (7.1). Figure 7.7 shows the three subsections and their coupling matrix. Each subsection is designed separately by optimization so that its S parameters match those from the corresponding coupling submatrix. It must be noted that, in each subsection, one or two internal couplings must be converted to external couplings.

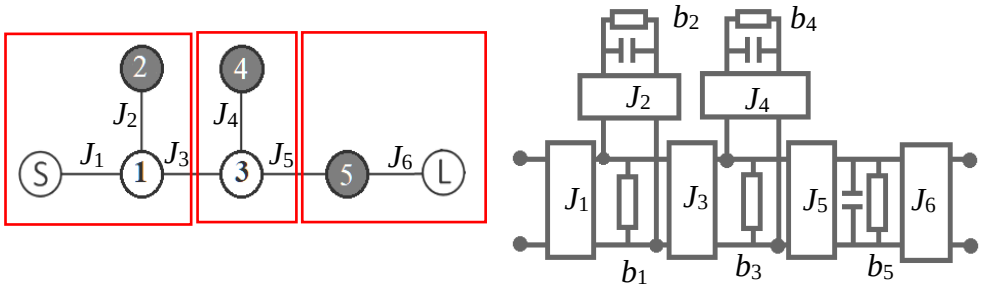

(a) (b)

Figure 7.6 A third-order filter with two transmission zeros. (a) Topology, which is divided into three subsections using three red rectangles. Dark and white circles represent resonators and NRNs, respectively. (b) Equivalent circuit model.

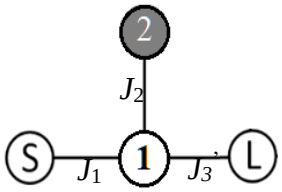

	S	1	2	L
S	0	1	0	0
1	1	2.0154	2.5285	0.3713
2	0	2.5285	3	0
L	0	0.3713	0	0

(a)

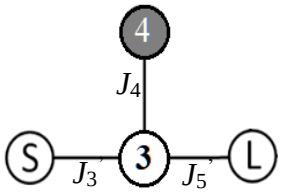

	S	1	2	L
S	0	0.3713	0	0
1	0.3713	-3.189	2.8878	0.411
2	0	2.8878	-3	0
L	0	0.4114	0	0

(b)

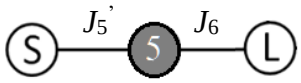

	S	3	L
S	0	0.4114	0
3	0.4114	-0.341	1.0685
L	0	1. 0685	0

(c)

Figure 7.7 A The three subsections of the filter. (a) First subsection including NRN 1 and resonator 2. J_3 is changed to J_3' using (7.2). (b) Second subsection including the NRN 3 and resonator 4. (c) Last subsection.

For example, in the case of Figure 7.7(b), the internal couplings J_3 and J_5 in Figure 7.6(a) are converted to the external coupling J_3' and J_5' using the following equation:

$$J_{\mathrm{i}}' = J_{\mathrm{i}} \times \sqrt{FBW \frac{\pi}{2} \left(\frac{\lambda_{\mathrm{g}}}{\lambda}\right)^2} \tag{7.2}$$

where J_{i}' represents the external coupling of the submatrix, J_{i} is the internal coupling of the coupling matrix, λ and λ_{g} are the free-space and guided wavelength, respectively. The diagonal elements of the submatrix, representing the self-coupling (for resonators, NRNs or ports), are also adjusted. For example, in the case of Figure 7.7(b), the diagonal elements corresponding to *S* and *L* are set to zero. Similar process is applied to other subsections. EM design for each subsection is achieved by dimensioning and optimization to fulfil the S parameters of the submatrix.

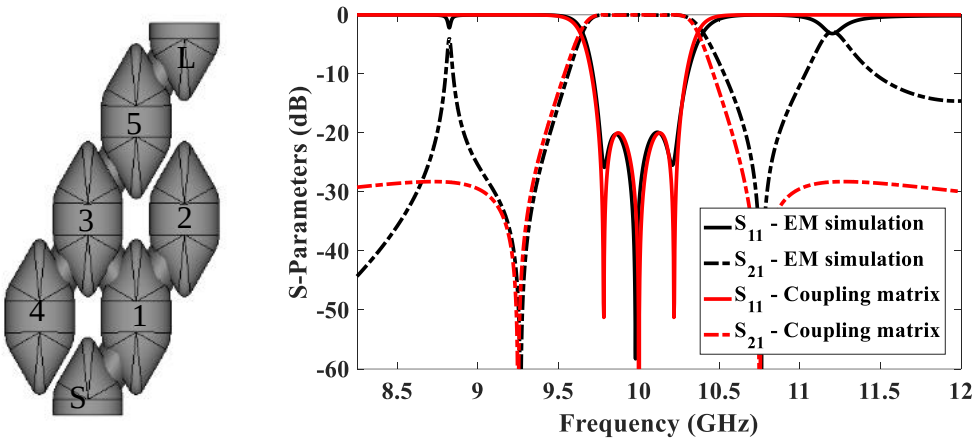

(a) (b)

Figure 7.8 The wideband filter. (a) Layout. (b) EM simulation results compared with the responses from the coupling matrix.

For the dimensioning process, the values of R_1, R_2, R_3 (for resonators) and minor axis (for irises) are fixed as defined in Figure 7.5. The only two parameters that control the resonant frequency and the coupling are l and the major axis, respectively. By controlling the value of l and the major axis, each subsection is designed to match the corresponding coupling matrix frequency response. Finally, all the subsections are joined together and optimized. Figure 7.8 shows the filter based on an E-plane configuration, using WR90 waveguide. The dominant mode is TE101. The designed structure can be seen in Figure 7.8(a). The filter is designed with 5×M2 tuning screws on the side wall (see Figure 7.3(a)) of each resonator and the NRN to fix the frequency detuning. The screws are designed to be inside each cavity by half of the cavity's length. The dimensions of the filter are as follows: d_{S1} (major axis of the elliptical iris between source and resonator 1) = 16.02 mm, d_{12} = 14.35 mm, d_{13} = 14.86 mm, d_{34} = 17.2 mm, d_{35} = 13.39 mm, d_{5L} = 15.17 mm, l_1 (length of resonator 1) = 20.28 mm, l_2 = 19.95 mm, l_3 = 24 mm, l_4 = 24.44 mm, l_5 = 22.39 mm. The minor axis of all elliptical irises is 6 mm and is fixed for the next two designs. The size of the filter is 57.7 mm × 31.4 mm × 24.44 mm and the volume are 1.91×10^4 mm^3. A similar filter designed using rectangular resonators would have a total length and volume of 71.10 mm and 2.41×10^4 mm^3, respectively, which are 23% longer and 26% bulkier. The EM simulation of the filter compared with the coupling matrix response can be seen in Figure 7.8(b). There are two spurious peaks out of band in the simulation. These are found to be strongly associated with the wide bandwidth of the filter. The strong coupling (and therefore large irises) allows resonances to establish at the lower and the upper bands. These are not seen in the narrow band filter to be presented later in Section 7.3.2.

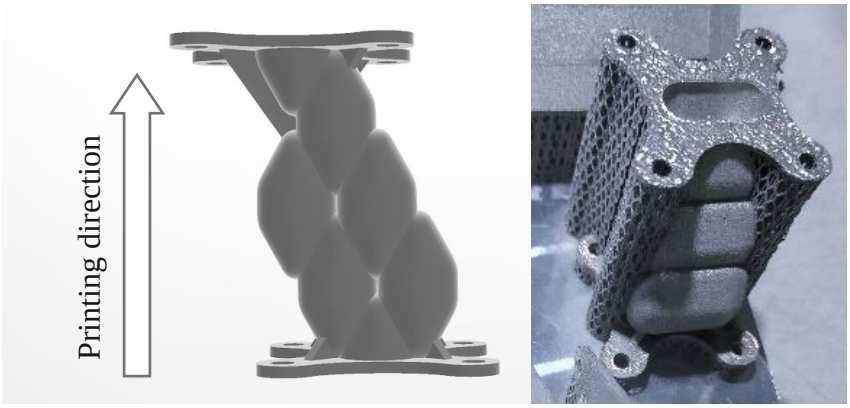

(a) (b)

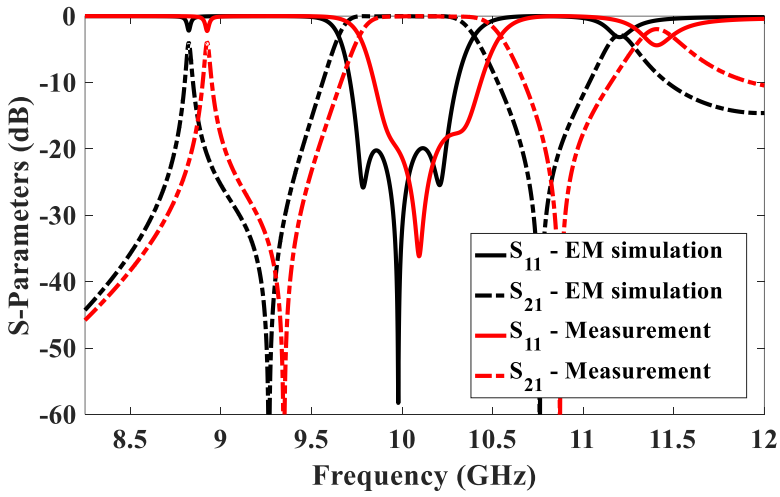

(c)

Figure 7.9 The wideband filter prototype. (a) Printing direction. (b) Fabricated filter on the printing platform. The net shape segments are supportive structures. (c) Measurement results compared with EM simulation.

Figure 7.9(a) shows the printing direction of the wideband filter. This printing direction is adopted in the next two designs. An image of the printed structure on the printer substrate with external supporting structures is presented in Figure 7.9(b). The tuning screw holes are drilled afterward. The thickness of the structure's outer walls and irises are set to 2 mm and 1 mm, respectively. The S parameter of the filter, without tuning screws, is measured and compared with the simulation in Figure 7.9(c). The measurements show about 150 MHz frequency shift towards the higher frequency. Five M2 tuning screws are added as can be seen in Figure 7.10(a).

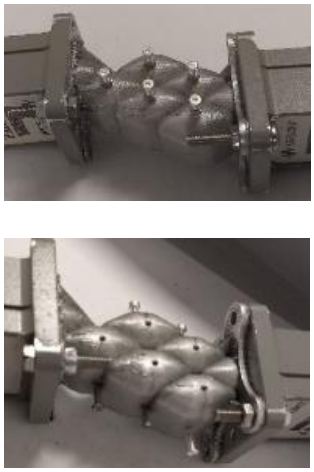

(a)

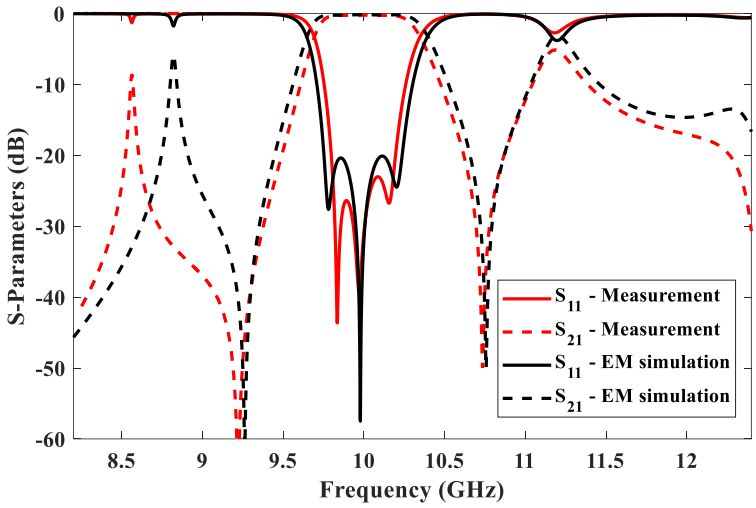

(b)

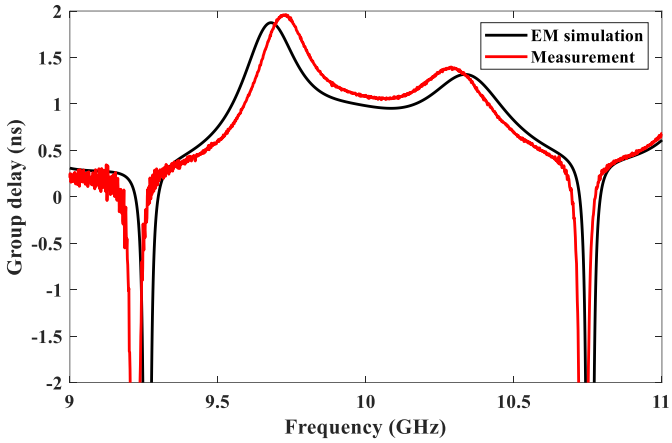

(c)

Figure 7.10 The wideband filter after tuning. (a) (Top) Tuning screws on the front wall. (Bottom) Same filter with tuning screws on the side walls. (b) Tuned results compared with EM simulation. (c) The measured group delay compared with the EM simulation.

The tuning screws could also be implemented on the front walls (marked out in Figure 7.3(a)) of the cavities. The side wall tuning screws are capable of correcting larger frequency shift whereas the front-wall tuning is more suitable for fine tuning. The latter is adopted in this design. The tuned response of the filter is compared with simulation in Figure 7.10(b). The in-band insertion loss is measured 0.21 dB compared to the simulation, which is 0.16 dB. The simulation is performed using the material effective conductivity, which is obtained using the nominal electrical conductivity and the surface roughness of the material. The filter bandwidth is reduced by 87 MHz compared to the simulation. The frequency of the lower out of band peak

is reduced by almost 150 MHz. The achieved return loss is 23 dB. The group delay of the tuned filter is measured and compared with the simulation in Figure 7.10(c).

7.3.2 A third-order narrowband filter with two transmission zeros

The second design is another third-order filter with two TZs, but with a much smaller FBW of 1%. The TZs are at 9.85 GHz and 10.15 GHz. Figure 7.11 shows the filter topology together with its equivalent circuit model. In order to demonstrate the capability of the resonator to implement various topologies the two dangling nodes are located at the first and last resonator rather than next to each other as in the first example. The same synthesis method is used and the value of circuit elements in Figure 7.11(b) are given as $J_1 = 1$, $J_2 = 2.5285$, $J_3 = 0.9700$, $J_4 = 1$, $J_5 = 2.6069$, $J_6 = 1.0310$, $b_1 = 2.329j$, $b_2 = 3j$, $b_3 = 0$, $b_4 = -2.4755j$ and $b_5 = -3j$. The coupling matrix of the filter is

$$\begin{bmatrix} 0 & 1 & 0 & 0 & 0 & 0 & 0 \\ 1 & 2.3290 & 2.5285 & 0.9700 & 0 & 0 & 0 \\ 0 & 2.5285 & 3 & 0 & 0 & 0 & 0 \\ 0 & 0.9700 & 0 & 0 & 1 & 0 & 0 \\ 0 & 0 & 0 & 1 & -2.475 & 2.6069 & 1.0310 \\ 0 & 0 & 0 & 0 & 2.6069 & -3 & 0 \\ 0 & 0 & 0 & 0 & 1.0310 & 0 & 0 \end{bmatrix} \tag{7.3}$$

Figure 7.12(a) shows the filter structure, designed using the step-tuning method as the previous example. Five M3 tuning screws are located on the front wall of and halfway into each cavity.

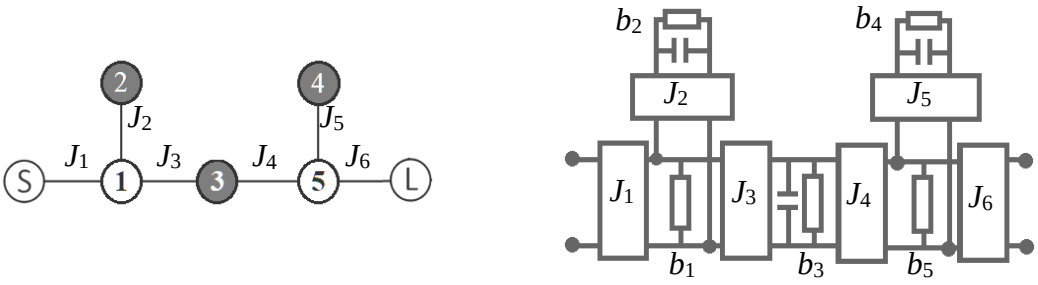

(a) (b)

Figure 7.11 A third-order filter with two transmission zeros. (a) Topology. (b) Equivalent circuit model.

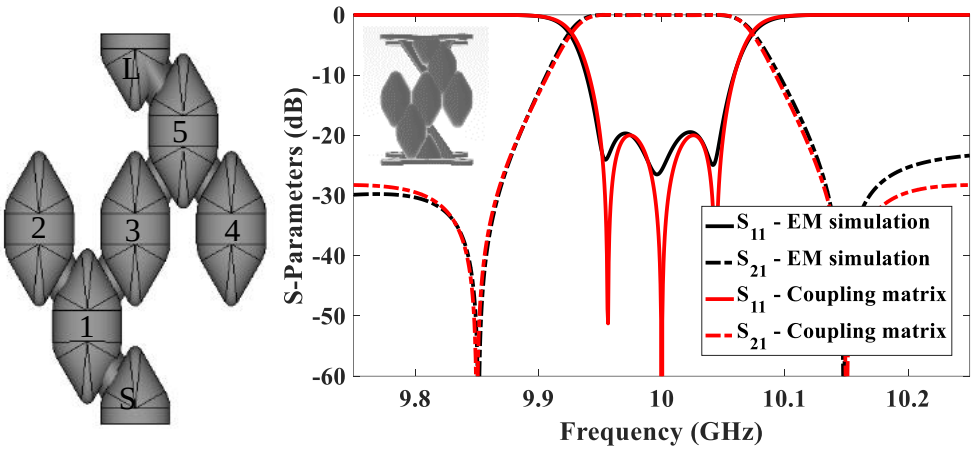

(a) (b)

Figure 7.12 The narrowband filter. (a) Layout. (b) EM simulation results compared with those from the coupling matrix.

The dimensions of the filter are as follows: d_{S1}= 13.87 mm, d_{12} = 12.2 mm, d_{13} = 9.69 mm, d_{35} = 9.05 mm, d_{34} = 12 mm, d_{5L} = 21.71 mm, l_1 = 20.6 mm, l_2 = 24.7 mm, l_3 = 26.17 mm, l_4 = 29.88 mm, l_5 = 26.85 mm. The general dimension of the filter is 57.72 × 38.48 × 29.88 mm^3. The EM simulation results is compared with the coupling matrix in Figure 7.12(b). The filter is fabricated with the same thickness for walls and irises as the previous design. The tuned response and group delay are compared with simulation in Figure 7.13, which shows an excellent agreement. The in-band insertion loss is measured as 0.63 dB, which is almost equal to the simulated loss of 0.65 dB. The fabricated filter is compared with other 3D printed filters reported in the literature in Table 7.2. Different geometries are used in designing filters in different frequency ranges. Each geometry offers different Q_u and printing direction. The spherical resonator filters have the highest Q_u and suitable for narrow-band filtering. The proposed filter made from hexagonal resonators with rounded corners shows a modest level of Q_u. The proposed hexagonal resonator is optimised for better surface finishing after 3D printing by minimising the ceiling surface compared with the spherical and ellipsoid resonators. Except for the rectangular resonator, the hexagonal, spherical, and ellipsoid resonators can offer more freedom in filter cavity arrangement. The resonators can be attached next or diagonal to each other. The proposed hexagonal resonator offers more compactness level compared to the other resonators by minimising the gap between cavities, when they sit next to each other.

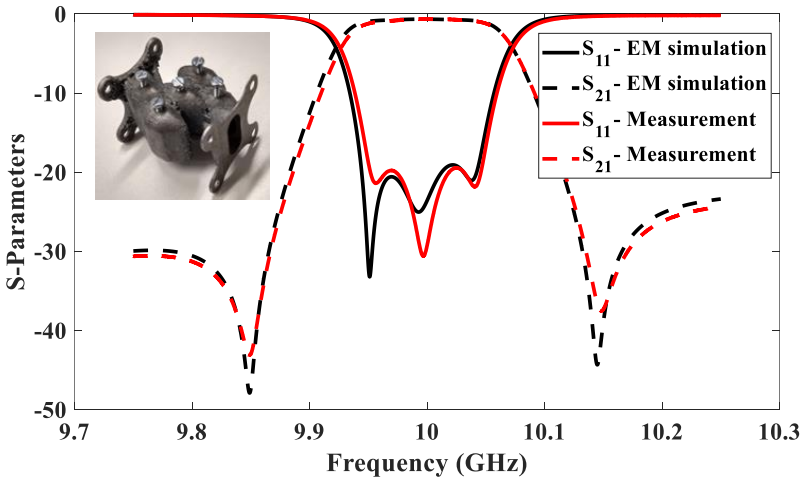
S-Parameters
Frequency (GHz)
S11 - EM simulation
S21 - EM simulation
S11 - Measurement
S21 - Measurement

(a)

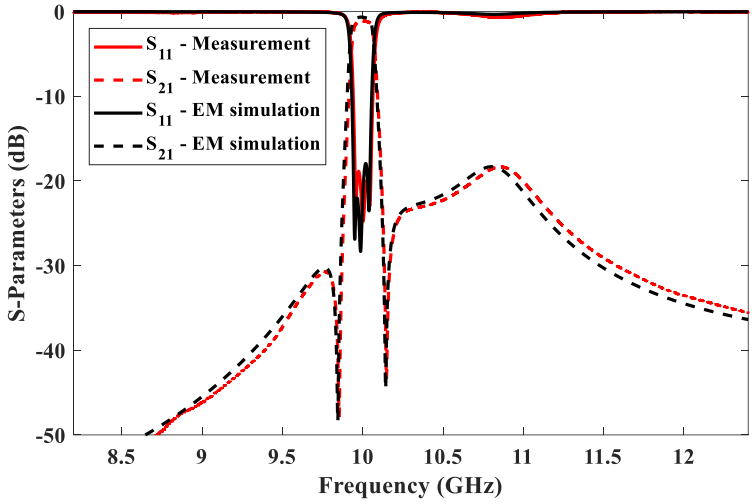
S-Parameters (dB)
Frequency (GHz)
S11 - Measurement
S21 - Measurement
S11 - EM simulation
S21 - EM simulation

(b)

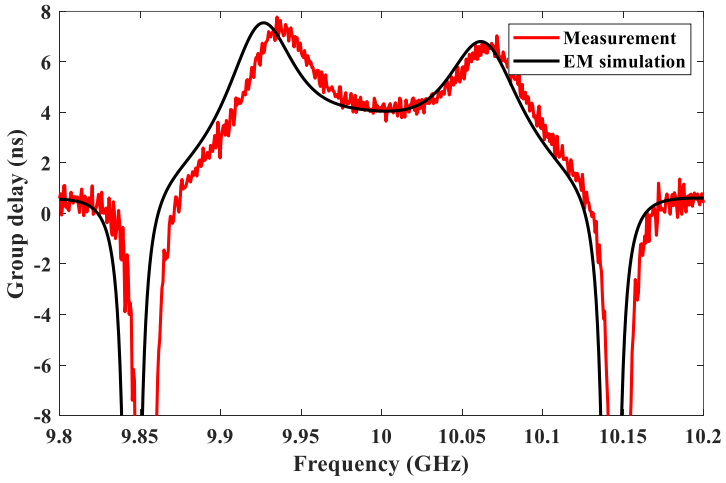
Group delay (ns)
Frequency (GHz)
Measurement
EM simulation

(c)

Figure 7.13 (a), (b) Tuned results of the narrowband filter compared with EM simulation using effective conductivity of the A20X. (c) Group delay of the tuned filter compared with the EM simulation.

Table 7.2 Comparison with previously reported filters

Ref.	Cavity geometry	Printing direction	BW (MHz)	fc (GHz)	IL (dB)	Qu	Cond.	Tech.
T.W.	Hexagonal	Vertical	100	10	0.63	3400	A20X	SLM
[7]	Spherical	Vertical	500	8.2	<0.4	5700	A20X	SLM
[10]	Rectangular	45º tilted	10 GHz	90	1	NA	copper	MLS
[13]	super-ellipsoid	Lying down	250	14.1	<0.2	4600	silver	SLM
[14]	super-ellipsoid	Lying down	250	12.9	<1	4400	silver	SLM
[17]	Spherical	Vertical	54	11.5	1	5800	silver	SLM
[20]	Hexagonal	Vertical	500	13	0.58	1000	PLA	FDM

7.3.3 A third-order wideband filter

The third example is a third-order filter, which is synthesised and designed using the well-known method in [23]. The specification of the filter is similar to the first design but without any TZs. The coupling matrix of the filter is given in (7.4). Figure 7.14(a) shows the topology of the filter.

$$\begin{bmatrix} 0 & 1.0825 & 0 & 0 & 0 \\ 1.0825 & 0 & 1.0303 & 0 & 0 \\ 0 & 1.0303 & 0 & 1.0303 & 0 \\ 0 & 0 & 1.0303 & 0 & 1.0825 \\ 0 & 0 & 0 & 1.0825 & 0 \end{bmatrix} \tag{7.4}$$

The filter is designed as displayed in Figure 7.14(b) with dimensions of l_1 = 24.81 mm, l_2 = 27.9 mm, l_3 = 24.79 mm, d_{S1}=14.3 mm, d_{12} = 9.97 mm, d_{23} = 9.96 mm, d_{3L} = 14.24 mm. The overall size of the filter is 56.24 mm × 17.24 mm × 27.9 mm and the volume are 1.44×10^4 mm^3. There are no tuning screws adopted in the design.

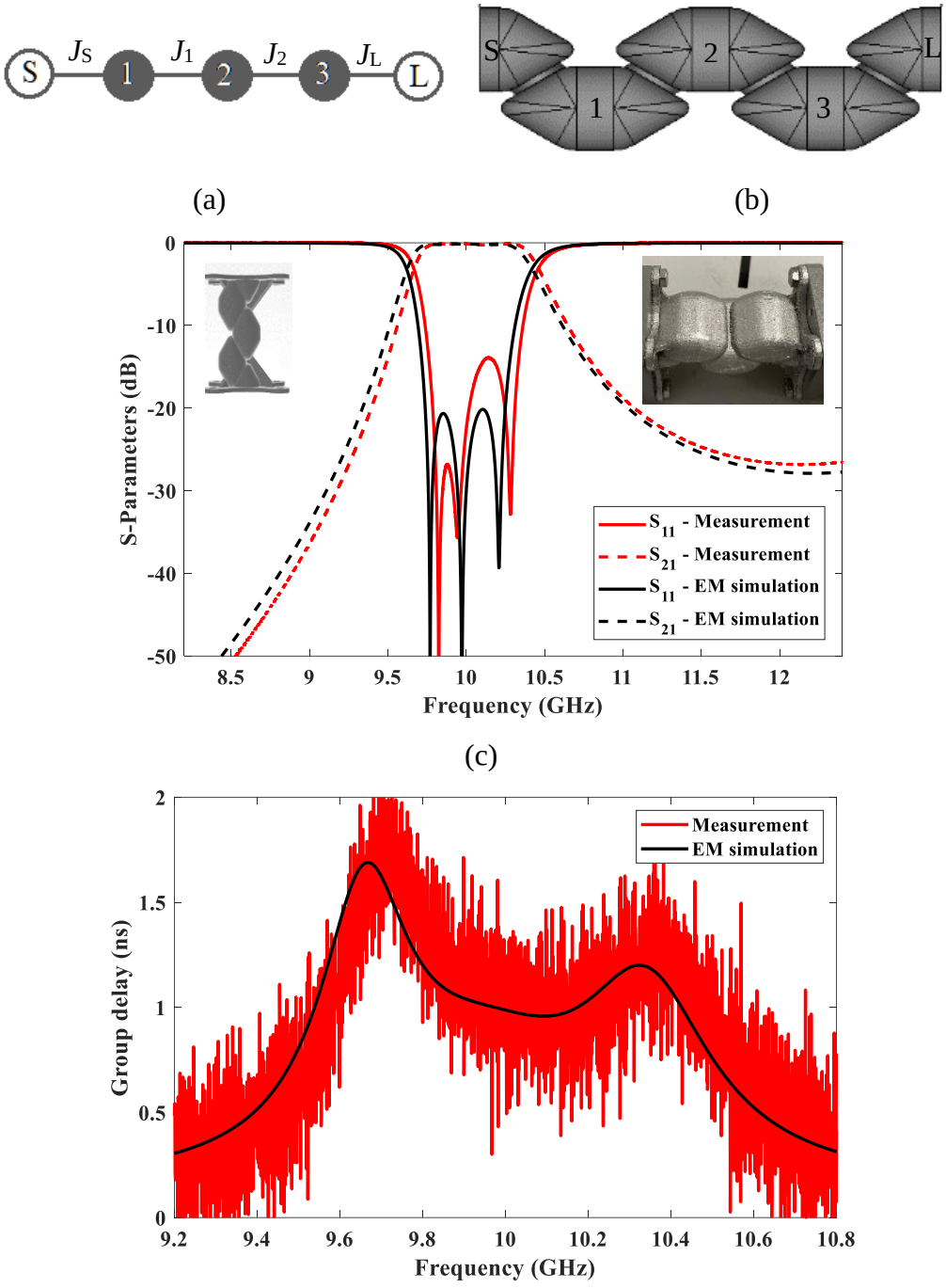

Figure 7.14 (a) Filter topology. (b) Layout. (c) The measured results compared with the EM simulation. (d) The measured group delay compared with the simulation.

A filter with similar specification using rectangular resonators would have a total length and volume of around 78.26 mm and 1.72×10^4 mm^3, respectively, which are 28% longer and 15% bulkier. The S parameter and group delay of the filter are measured and compared with the

simulation in Figure 7.14(c), showing very good agreement without any tuning. The measurements show 52 MHz frequency shift towards the higher frequency. Simulation-based investigation shows that the frequency discrepancy could be because the length of resonators is around 300 μm less than the design. Moreover, there are some defected surfaces observed around the irises. This could also contribute to the frequency shifts. The in-band insertion loss is measured at 0.12 dB, while it is 0.15 dB in the simulation.

7.4 Conclusion

A resonator structure, self-supportive for 3D printing, is presented to allow compact layout of coupled resonator filters with dangling nodes for generating TZs. The resonator provides a compact design compared to the regular rectangular resonators. For a resonator with a resonant frequency of 10 GHz, using the proposed resonator, the height of the structure is reduced by 36% compared with the rectangular resonator. The resonator offers a good modularity for the filter structure. The Q_u of the proposed resonator is 10% less than rectangular resonators. It is shown that the Q_u can be improved by choosing a different θ_d, i.e., $\theta_d = 45^\circ$ or mixed $30^\circ/45^\circ$. Three different filters are designed using the proposed resonator model and fabricated using SLM technology to verify the feasibility and capability of the resonator. The measurements show frequency shift after fabrication. This is corrected by tuning. The side wall tuning is more suitable for the wideband filter, whilst the front wall tuning is effective for the narrow band filter.

References

[1] A. Mostaani, Y. Wang, L. Qian, A. E. -M. A. Mohamed, M. M. Attallah and T. Skaik, "Compact Self-Supportive Filters Suitable for Additive Manufacturing," *IEEE Transactions on Components, Packaging and Manufacturing Technology*.

[2] D. Miek, S. Simmich, F. Kamrath and M. Höft, "Additive Manufacturing of E-Plane Cut Dual-Mode X-Band Waveguide Filters With Mixed Topologies," *IEEE Transactions on Microwave Theory and Techniques*, vol. 68, no. 6, pp. 2097-2107, June 2020.

[3] K. Y. Chan, R. Ramer and R. Sorrentino, "Low-Cost Ku-Band Waveguide Devices Using 3-D Printing and Liquid Metal Filling," *IEEE Transactions on Microwave Theory and Techniques*, vol. 66, no. 9, pp. 3993-4001, Sept. 2018.

[4] I. Piekarz, J. Sorocki, N. Delmonte, L. Silvestri, S. Marconi, G. Alaimo, F. Auricchio, and M. Bozzi, "Wideband Microstrip to 3-D-Printed Air-Filled Waveguide Transition Using a Radiation Probe," *IEEE Microwave and Wireless Components Letters*, vol. 32, no. 10, pp. 1179-1182, Oct. 2022.

[5] A. Fontana, A. Delage, A. Périgaud, P, Richard, D, Carsenat, G, Acikalin, S, Verdeyme, B, Bonnet, L, Carpentier, and N, Delhote , "A Novel Approach Toward the Integration of Fully 3-D Printed Surface-Mounted Microwave Ceramic Filters," *IEEE Transactions on Microwave Theory and Techniques*, vol. 71, no. 9, pp. 3915-3928, Sept. 2023.

[6] K. Zhao and D. Psychogiou, "Monolithic Multiband Coaxial Resonator-Based Bandpass Filter Using Stereolithography Apparatus (SLA) Manufacturing," *IEEE Transactions on Microwave Theory and Techniques*, vol. 70, no. 9, pp. 4156-4166, Sept. 2022.

[7] X. Wen, C. Guo, X. Shang, Y. Yu, M. Shu, Q. Yang, S. Li, M. M. Attallah, H. Liu, and A. Zhang, "SLM Printed Waveguide Dual-Mode Filters With Reduced Sensitivity to Fabrication Imperfections," *IEEE Microwave and Wireless Components Letters*, vol. 31, no. 11, pp. 1195-1198, Nov. 2021.

[8] E. A. Rojas-Nastrucci, J. T. Nussbaum, N. B. Crane and T. M. Weller, "Ka-Band Characterization of Binder Jetting for 3-D Printing of Metallic Rectangular Waveguide Circuits and Antennas," *IEEE Transactions on Microwave Theory and Techniques*, vol. 65, no. 9, pp. 3099-3108, Sept. 2017.

[9] M. Baranowski, L. Balewski, A. Lamecki, M. Mrozowski, and J. Galdeano, "The Design of Cavity Resonators and Microwave Filters Applying Shape Deformation Techniques," *IEEE Transactions on Microwave Theory and Techniques*, vol. 71, no. 7, pp. 3065-3074, July 2023.

[10] M. Salek, X. Shang, R. C. Roberts, M. J. Lancaster, F. Boettcher, D. Weber, and T. Starke, "W-Band Waveguide Bandpass Filters Fabricated by Micro Laser Sintering," *IEEE Transactions on Circuits and Systems II: Express Briefs*, vol. 66, no. 1, pp. 61-65, Jan. 2019.

[11] A. Mostaani, L. Qian, R. Martinez, P. F. Wilson, M. Attallah, Y, Wang, M. A. Williams, "Investigation of a 3D-Printed Narrowband Filter with Non-Resonating Nodes," *2021 IEEE MTT-S International Microwave Filter Workshop (IMFW)*, 2021, pp. 316-318.

[12] W. Ameen, A. A.-Ahmari, and M. K. Mohammed, “Self-supporting overhang structures produced by additive manufacturing through electron beam melting.” *The International Journal of Advanced Manufacturing Technology*, 104, no. 5 (2019): 2215-2232.

[13] P. Booth and E. V. Lluch, “Enhancing the Performance of Waveguide Filters Using Additive Manufacturing,” *Proceedings of the IEEE*, vol. 105, no. 4, pp. 613-619, April 2017.

[14] P. Booth and E. V. Lluch. “Realising advanced waveguide bandpass filters using additive manufacturing.” *IET Microwaves, Antennas & Propagation*, 11, no. 14 (2017): 1943-1948.

[15] M. Simonelli, Y. Y. Tse, and C. Tuck. “Effect of the build orientation on the mechanical properties and fracture modes of SLM Ti–6Al–4V.” *Materials Science and Engineering: A*, 616 (2014): 1-11.

[16] F. Calignano, “Design optimization of supports for overhanging structures in aluminum and titanium alloys by selective laser melting”, *Materials and Design*, vol. 64, pp. 203-213, Dec. 2014.

[17] L. Qian, Y. Wang, S. Li, A. E.-M. A. Mohamed, M. M. Attallah, T. Skaik, P. Booth, L. Pambaguian, C. M. España, and P. M.-Iglesias, “A Narrowband 3-D Printed Invar Spherical Dual-Mode Filter With High Thermal Stability for OMUXs.” *IEEE Transactions on Microwave Theory and Techniques*, 70, no. 4 (2022): 2165-2173.

[18] M. Hameed, G. Xiao, & C. Xiong, “Triple-mode wideband bandpass filter using triangular waveguide cavity.” *2018 IEEE MTT-S International Wireless Symposium (IWS)*, Chengdu, China, 2018, pp. 1-3.

[19] V. Weißmann, P. Drescher, H. Seitz, H. Hansmann, R. Bader, A. Seyfarth, A. Klinder, and A. Jonitz-Heincke. “Effects of build orientation on surface morphology and bone cell activity of additively manufactured Ti6Al4V specimens.” *Materials* 11, no. 6 (2018): 915.

[20] K. Y. Chan, R. Ramer and R. Sorrentino, “Low-Cost Ku-Band Waveguide Devices Using 3-D Printing and Liquid Metal Filling,” *IEEE Transactions on Microwave Theory and Techniques*, vol. 66, no. 9, pp. 3993-4001, Sept. 2018.

[21] R. J. Cameron, C. Kudsia and E. Mansour, “*Microwave filters for communication systems*,” 2nd ed., Hoboken, USA: J. Wiley., 2018, pp. 323–335.

[22] Amari, Smain, and Giuseppe Macchiarella. “Synthesis of inline filters with arbitrarily placed attenuation poles by using nonresonating nodes.” *IEEE Transactions on Microwave Theory and Techniques*, 53, no. 10 (2005): 3075-3081.

[23] J. S. Hong and M. J. Lancaster, *Microstrip Filters for RF/Microwave Applications*. New York, NY, USA: Wiley, 2001.

CHAPTER 8

A MONOLITHIC 3D-PRINTED E-BAND CAVITY FILTER: MANUFACTURE AND SURFACE TREATMENT

Paper in submission

Abolfazl Mostaani*, Talal Skaik*, Lu Qian*, Peter Huggard**, Peter Hunyor**, Xiaobang Shang***, Yi Wang*

IEEE Microwave and Wireless Components Letters

A. Mostaani proposed the geometry for the resonator and synthesised and designed the filter and wrote the manuscript in collaboration with T. Skaik, L. Qian, P. Huggard, P. Hunyor, X. Shang, and Y. Wang. T. Skaik, L. Qian and X. Shang assisted in the measurements of surface roughness and filter S parameters. P. Huggard, P. Hunyor polished the filter and also measured the surface roughens of the device.

* School of Engineering University of Birmingham, Birmingham, U.K.

** UKRI STFC Rutherford Appleton Laboratory, Oxford, U.K.

*** National Physical Laboratory, Teddington, U.K.

8.1 Introduction

Additive manufacturing is a revolutionary fabrication technology for passive microwave components. Thanks to its capability of fabricating complex structures with reduced or no assembly requirement, AM plays an increasingly important role in size, weight, and power (SWAP) reduction, especially for satellite applications. Various microwave devices have been demonstrated using different AM technologies such as fused deposition modeling (FDM) [1],[2], polyjet printing [3], stereolithographic apparatus (SLA) [4],[5] and selective laser melting (SLM) [6],[7].

Taking advantage of AM, microwave engineers are able to make more compact, monolithic and lightweight components, which is hard or impossible to achieve using conventional machining [8]. However, it demands a careful design-for-manufacture approach. For example, it is critical to optimize the component geometries to avoid overhangs in order to reduce the risk of printing failure, or to ensure structure integrity and surface quality of the as-printed parts. Any downward-facing surface with a slope less than 45° should be avoided [9]. Sharp corners or trapped cavity structures may be avoided to facilitate surface post-processing. Surface finish of the printed components using SLM is generally much poorer than CNC machining. This is due to some intrinsic limitations such as the particle size of the metal powder and the laser spot size. Surface roughness can be a significant issue for filters, especially for millimeter-wave (mm-wave) applications [10]. When the skin depth becomes comparable with the surface roughness, the effective conductivity of the surface can be significantly reduced, causing increased insertion loss (IL). One method to improve the surface finish is through post-processing such as polishing and plating. For X and Ku band filters, mechanical polishing [11] and electropolishing [12],[13] have been shown to be effective to some extent. However, both have their limitations. Generally, it is difficult for mechanical polishing to access internal surfaces. While vibratory grinding has been shown to reduce internal surface roughness from around 12 μm to 5-7 μm [14], it is almost impossible to reduce the roughness further due to the size limit of the polishing agents and the reduced impact inside the metal cavities. Electropolishing could be more effective in reducing the surface roughness, but it is more difficult to control and often aggressively erodes fine internal features.

The printing and polishing for millimeter-wave waveguide filters are exponentially more difficult due to their small size (down to 100s or even 10s of microns) and sensitivity to

dimensional offset as a result of printing tolerance. Hence, an accurate 3D printing technology and an effective and controllable plating and polishing process are highly desired to meet the needs from mm-wave devices. From the open literature, we have not seen any effective polishing techniques applied to high mm-wave metal 3D-printed filters.

In this work, we have established an end-to-end manufacture process from metal 3D printing, polishing, to plating, demonstrated in an 3D printed monolithic E-band filter. A modified hexagonal shaped resonator is used to construct the filter to be printed in one piece using a high-precision laser powder bed fusion technique – micro laser sintering (MLS) [10],[15],[16]. This structure reduces the overhangs and enhances the printability of the filters. The geometry allows closely packed resonators to be laid out in a low profile without requiring any internal support structures during printing and without the need of tilting the build as in many rectangular cavity-based filters. This high-precision metal printing technique has been used to produce mm-wave filters before [20]. However, in this work, for the first time we will demonstrate a polishing technique, which is effective in reduce the surface roughness to 1.95 µm without detrimentally eroding the internal coupling structures. This much improved surface quality results in significantly reduced insertion loss of the filter to a record low level.

8.2 Filter design

The filter has a Chebyshev response, a central frequency of 83.5 GHz and bandwidth of 5 GHz. The return loss level within the passband is 23 dB. Figure 8.1(a) and (b) show the topology of the filter together with its equivalent circuit model.

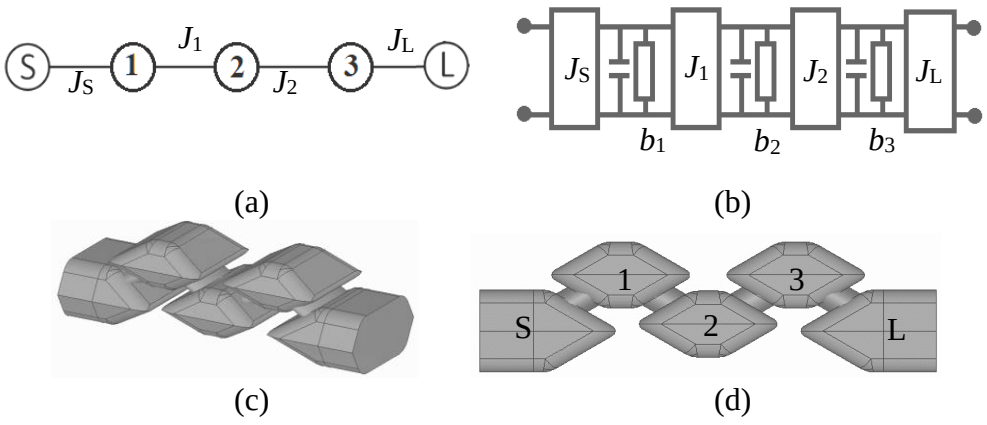

Figure 8.1 (a) Filter topology. (b) Equivalent circuit model of the filter. (c) and (d) Air model of the filter in different views.

(a) (b)

Figure 8.2 (a) Resonator geometry. (b) Elliptical iris geometry.

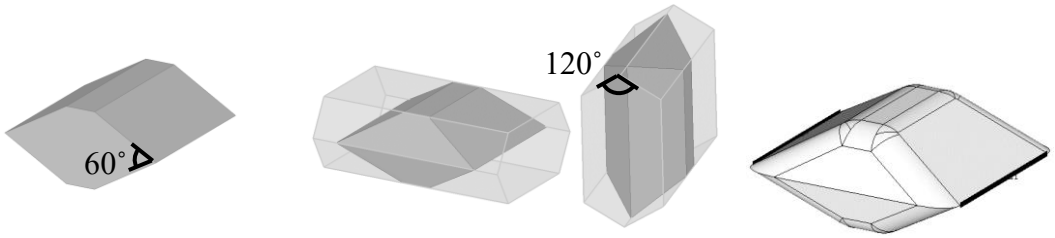

(a) (b) (c)

Figure 8.3 Evolution of the resonator geometry: (a) The primary shape, h = 3.2988 mm and w = 1.5494 mm. (b) After intersection with a hexagonal prism (light grey). (c) After rounding by radius of 0.1 - 0.5 mm.

The circuit element values are obtained as J_S = 1.0825, J_1 = 1.0303, J_2 = 1.0303, J_L = 1.0825, $b_1 = b_2 = b_3 = 0$ using the well-known method in [17]. The filter is designed using the step tuning method, in which the filter topology and the coupling matrix are divided to three subsections. Each subsection is optimized separately so that its S parameters from the EM simulation match the one from the coupling submatrix. The optimized subsections are connected to each other to form the filter structure before a final optimization. Details of this process can be found in [18]-[20]. The designed filter is shown in Figure 8.1(c) and (d). Modified hexagonal resonators and elliptical irises are used. The resonator and the iris geometries are shown in Figure 8.2. w and h are fixed to 1.549 mm and 3.099 mm (standard dimensions of WR12 waveguide), respectively, for all resonators. The steps of creating the modified resonator are shown in Figure 8.3. The 83.5 GHz resonator has a volume of 8.9 mm^3, which is 57% smaller than the rectangular resonator at the same resonance frequency. Its compactness, however, reduces its Q-factor to 2666. This is around 1000 less than the rectangular resonator. A trade-off has been made. The dimensions of the designed filter are: d_{S1} (major axis, d_1 in Figure 8.2(b), of the elliptical iris between source and resonator 1) = d_{3L} = 2.05 mm, $d_{12} = d_{23}$ = 1.63 mm, l_1 (length

of resonator 1) = 2.81 mm, l_2 = 3.25 mm, l_3 = 2.81 mm. The minor axis (d_2 in Figure 8.2(b)) of the elliptical irises is fixed to 0.3 mm.

8.3 Fabrication and measurement

8.3.1 Printing

Figure 8.4(a) shows the initial CAD model of the filter with the standard flanges. The modified hexagonal shaped resonators are self-supportive. This allows the resonators to be built along the direction of the long axis of the resonator. However, for the rectangular waveguide feed, the narrow wall would be a downward facing surface. To avoid this overhang structure, the narrow wall of the feed waveguide has been modified into a pointed roof structure as shown in Figure 8.4(b). To reduce the printing height (and therefore the cost), a portion of the flange was removed. This does reduce the reliability of the flange interconnection but without impacting much on the laboratory verification. It should also be noted that the holes on the flanges have been modified into a waterdrop shape, again to avoid overhang. The outer profile of flanges was changed into a wavy shape to relieve potential thermal stress. Furthermore, the flanges must have sufficient bending stiffness at the joint with the main body of the filter so that they do not collapse during the printing process. Otherwise, additional support struts should be added to the flanges. Figure 8.4(b) shows the final design for fabrication. The overall dimension of the filter is 19 mm × 8.6 mm × 12.5 mm. Two samples of the filter are fabricated by the powder bed based additive manufacturing technology, known as MLS, out of stainless-steel material.

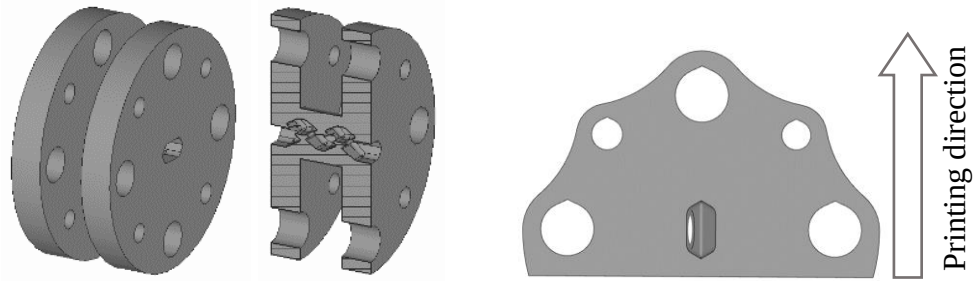

(a) (b)

Figure 8.4 (a) Initial CAD model with full flanges. (b) Modified final model and the printing direction.

MLS offers much higher manufacture accuracy than conventional SLM/SLS. It handles metal powders of a particle size, D_{90}, of 5 µm (this is typically 50 µm for SLM/SLS). The printer uses a laser with 50 W laser average power. During the process the laser spot diameter was focused down to 30 µm and operates in continuous wave mode. The layer thickness is around 7 µm. This printing technique renders a manufacture tolerance of 5-10 µm, while most other metal 3D printers (used to produce microwave components) have a tolerance of around 25-100 µm. The as-printed surface roughness achieved from MLS is also much lower than other metal printing techniques. We have measured this to be around 2-5 µm [10],[15],[21]. Other metal 3D printing usually results in a surface roughness of ~10 µm [6],[22],[23]. It should be born in mind that on the downward facing surfaces, the surface roughness is usually much higher than this, due to the lack of support during printing.

8.3.2 Polishing

Due to the small opening of the monolithic structure, mechanical polishing is not feasible. We have experimented with an electrochemical polishing process – the so-called Hirtisation® [24]. We have not seen any previous application of this process or similar to such small 3D-printed mm-wave parts. For the stainless-steel parts, the medium used was SS-Auxilex. It has been found that this polishing process is less aggressive and more controllable than conventional electrochemical processes. A material removal of about 30 µm was specified. Dimensional metrology shows a removal of about 25±5 µm. The measured surface roughness on the outer surface of the filter, using an Alicona Infinitive Focus SL 3D microscope, before and after the polishing is summarized in Table 8.1. The roughness is halved by Hirtisation. This has been consistently achieved with other MLS printed parts we have experimented too. These values are used to obtain the effective conductivity [25] of the stainless steel and gold, as given in Table 8.1. Using these effective conductivity values, the simulated insertion losses are given in Table 8.1. Later we will show this improved surface roughness also results in much improved RF performance from the measurements. Figure 8.5(a) and (b) compares the microscopic profile of a flange surface after wire cutting and a 3D-printed surface after polishing. Although the latter is still much rougher than the machined surface, the Hirtisation process provides clear smoothing effect on the printed surface.

Table 8.1 Measured surface roughness and insertion loss of the filter before and after Hirtisation® surface treatment.

	Sample-1 (Unpolished)		Sample-2 (Polished)	
	Uncoated	coated	Uncoated	coated
[1]S_a (µm)	4.35	2.90	1.95	2.00
[2]σ_{eff} (S/m)	3.6×10^5	1.03×10^7	4.4×10^5	1.04×10^7
Sim. min IL (dB)	1.37	0.274	1.24	0.27
Meas. min IL (dB)	1.5	0.43	1.14	0.14

[1]S_a represents the surface roughness evaluated with filtering, which removes the waviness effect. [2]σ_{eff} is the effective conductivity taking into account the measured surface roughness.

8.3.3 Plating

Stainless-steel has a poor electrical conductivity and therefore has to be coated with high-conductivity metals, such as gold in this case, especially on the internal surface. This is not straightforward for a monolithically built structure with cavities not in a line-of-sight configuration. See Figure 8.4(a). A proprietary electroless plating process was used. This was discussed in [8],[10] and will not be repeated here. Sample-1 is gold coated without polishing, whereas Sample-2 is polished before gold coating, in order to investigate the effect of the polishing process. After gold coating, the surface roughness was measured again, as given in Table 8.1.

8.3.4 Measurements

The insets of Figure 8.5(c) shows Sample-1 (unpolished) filter before and after gold coating. Measurements were carried out using a Keysight PNA-X N5247B Vector Network Analyzer with a pair of VDI WR12 (60-90 GHz) frequency extension modules. Before the measurements, through-reflect-line (TRL) calibrations were performed. The corresponding measured responses are compared with the EM simulation. The measured insertion loss of the uncoated filter is 1.5 dB, which is 0.13 dB more than the estimated insertion loss from the simulation taking into account the measured surface roughness. After gold coating, the insertion loss is reduced to 0.43 dB. The frequency shift is measured around 1.2 GHz and 400 MHz before and after coating, respectively. Based on the simulations, it is estimated that the frequency shift

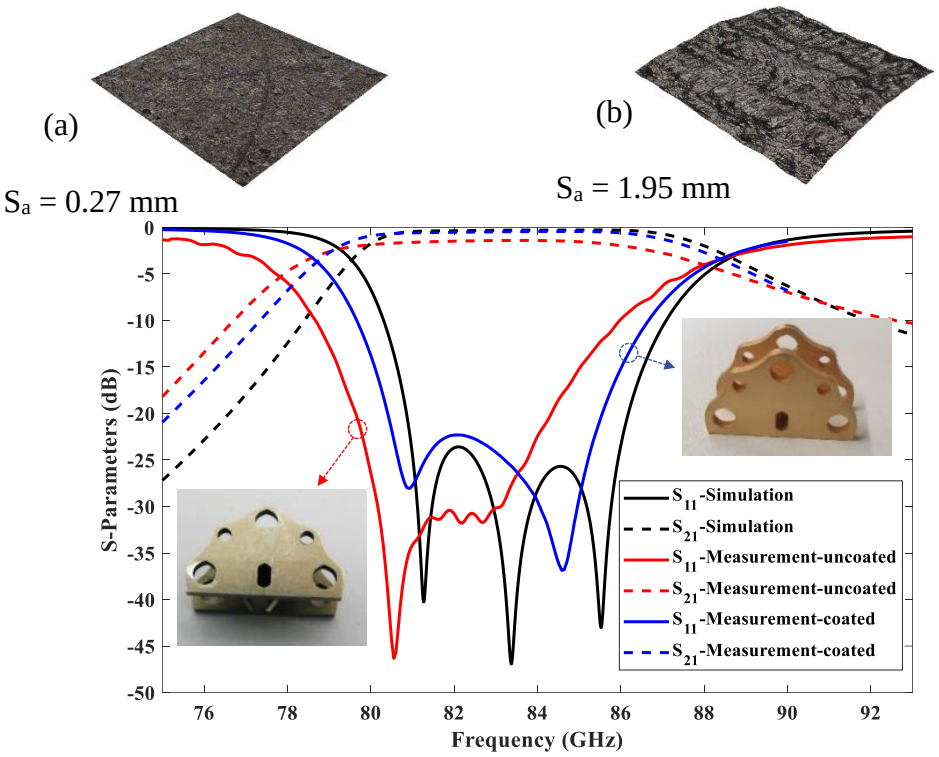

(c)

Figure 8.5 (a) A flat flange surface after electrical discharge machining (EDM) and polishing, S_a = 0.27 mm; (b) A curved 3D-printed surface after polishing, S_a = 1.95 mm; (c) Sample-1 (insets, unpolished): S parameters comparison before and after gold coating.

could be a result of 4 µm thick coating deposited inside the cavities. There is a noticeable degradation in the S_{11} performance due to the manufacturing tolerance. Unfortunately, it is not yet feasible to tune such small cavity structures. Figure 8.6(a) compares the responses of two uncoated stainless-steel filters before and after polishing. Polishing reduces the insertion loss by 0.36 dB to 1.14 dB. The insertion loss is 0.1 dB lower than the simulation result. Figure 8.6(b) and (c) compares the S parameters of the two gold-coated samples – Sample-1 (unpolished) and Sample-2 (polished). After polishing, the measured insertion loss is further reduced by 0.29 dB to 0.14 dB. This is 0.13 dB lower than the simulation result. The better-than-expected ILs in both polished cases seem to suggest the achieved surface roughness may be even lower than 1.97/2.00 µm. The measured insertion losses for both samples are compared with the simulations in Table 8.1. Polishing causes a shift of the central frequency by 800 MHz as a result of material removal. Simulation shows that an increase in cavity dimensions by ~20 µm and size of irises by ~30 µm would cause a similar level of frequency shift. This is consistent

with the specified 30 µm material removal from the Hirtisation process. This indicates a good control of the polishing process parameters. After gold coating, the frequency shift has been improved to 1.6 GHz as the deposited gold compensates for the removed material during the polishing process. Table 8.2 provides a comparison of measured insertion loss of filters that are fabricated using different types of manufacturing technique. The group delay of the polished and coated filter is measured and compared with the simulation in Figure 8.6(d).

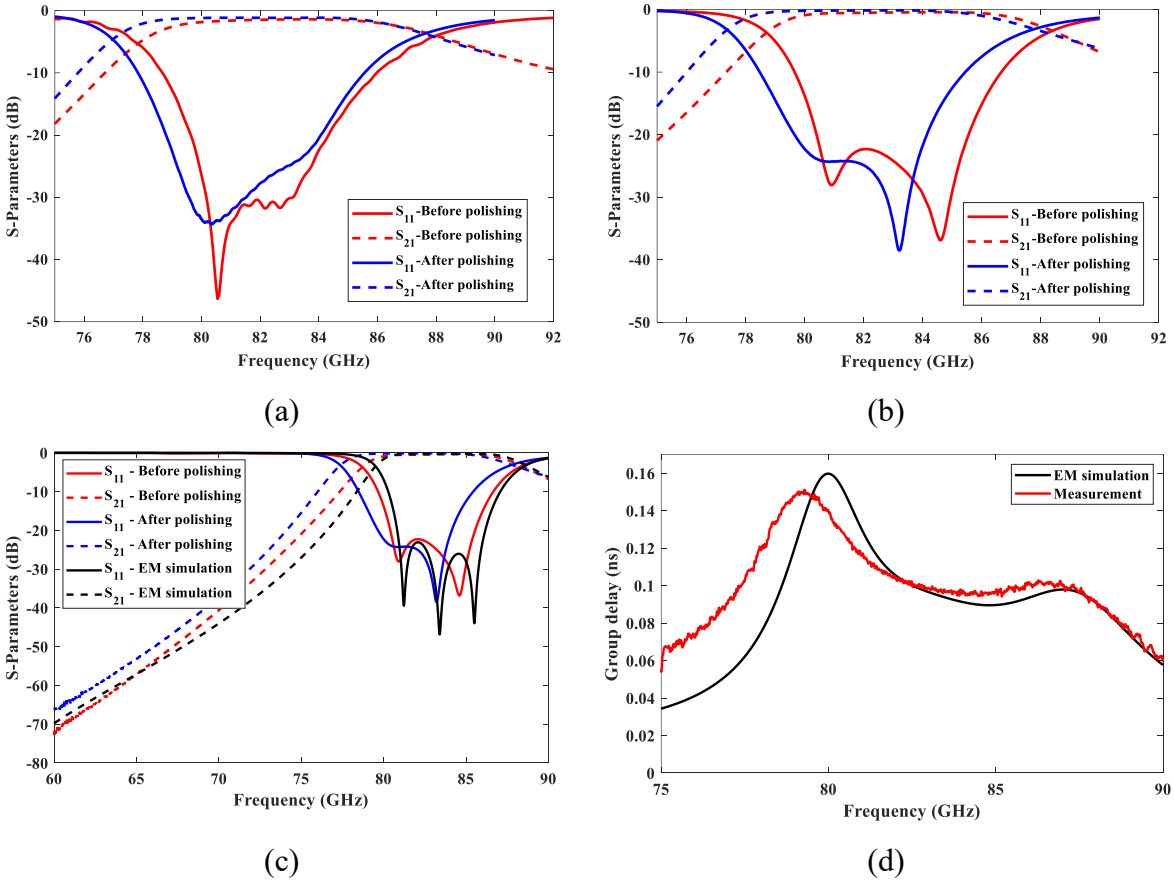

Figure 8.6 S parameters comparison between the two samples (a) before gold coating and (b) after gold coating. (c) The same graph of Figure (b) but in the whole frequency band. (d) Measured group delay of the polished and coated filter compared to simulation.

Table 8.2 Comparison with other waveguide bandpass filters

Ref.	fc (GHz)	FBW (%)	IL (dB)	Manufacturing technique
[21]	88.34	12.1	1.94	MLS
[21]	89.1	11.1	1	MLS
[26]	87.5	11.5	0.3-0.5	SLA
[27]	75.5	5.3	8	SLM
[28]	92.6	4.53	0.5	CNC
[29]	92.5	20	0.6	CNC
T.W.	83.5	6	0.14	MLS

8.4 Conclusion

In this paper, a metal 3D printed E-band bandpass filter is used to demonstrate the effectiveness of the surface treatment using the Hirtisation® polishing process. The filter is designed using the modified hexagonal resonator. Two samples are fabricated using MLS-based high-precision metal 3D printing technology out of stainless steel. Sample-1 is gold coated after printing, while sample-2 is electrochemically polished using Hirtisation process and then gold coated. The effects of polishing and coating have been investigated by comparison of the measured S parameters. It shows the gold coating improves the insertion loss by about 1 dB whereas the polishing step further reduces the insertion loss by about 0.3 dB. This results in an impressively low insertion loss of only 0.14 dB for sample-2. Surface characterization shows that the Hirtisation process halves the surface roughness of the as-printed stainless-steel parts. From the measured frequency shifts, it can be inferred (estimated by simulation) that the gold coating thickness is about 4 mm whereas the material removal by polishing is about 20 µm. These are both in reasonable agreement with the expectation. It should be noted that the material removal rate in the Hirtisation process can be adjustable. A larger removal rate (e.g., 100 µm) can usually be better controlled so that even lower surface roughness may be achieved. This work shows the effectiveness of the polishing process. Together with the coating process, this could be a viable surface treatment technique that is highly anticipated for metal 3D printed mm-wave waveguide devices.

References

[1] D. Miek, S. Simmich, F. Kamrath and M. Höft, “Additive Manufacturing of E-Plane Cut Dual-Mode X-Band Waveguide Filters With Mixed Topologies,” *IEEE Transactions on Microwave Theory and Techniques*, vol. 68, no. 6, pp. 2097-2107, June 2020.

[2] K. Y. Chan, R. Ramer and R. Sorrentino, “Low-Cost Ku-Band Waveguide Devices Using 3-D Printing and Liquid Metal Filling,” *IEEE Transactions on Microwave Theory and Techniques*, vol. 66, no. 9, pp. 3993-4001, Sept. 2018.

[3] I. Piekarz, J. Sorocki, N. Delmonte, L. Silvestri, S. Marconi, G. Alaimo, F. Auricchio, and M. Bozzi, “Wideband Microstrip to 3-D-Printed Air-Filled Waveguide Transition Using a Radiation Probe,” *IEEE Microwave and Wireless Components Letters*, vol. 32, no. 10, pp. 1179-1182, Oct. 2022.

[4] C. Guo, J. Li, Y. Yu, F. Zhang, Y. Zhu, Q. Yang, W. Zhu, S. Zhu, X. Shang, Y. Gao, Y. Wang, G.-L. Huang, Q. S. Cheng, and A. Zhang, “A 3-D Printed E-Plane Waveguide Magic-T Using Air-Filled Coax-to-Waveguide Transitions,” *IEEE Transactions on Microwave Theory and Techniques*, vo. 67, no. 12, pp. 4984 – 4994, Dec. 2019.

[5] K. Zhao and D. Psychogiou, “Monolithic Multiband Coaxial Resonator-Based Bandpass Filter Using Stereolithography Apparatus (SLA) Manufacturing,” *IEEE Transactions on Microwave Theory and Techniques*, vol. 70, no. 9, pp. 4156-4166, Sept. 2022.

[6] X. Wen, C. Guo, X. Shang, Y. Yu, M. Shu, Q. Yang, S. Li, M. M. Attallah, H. Liu, and A. Zhang, “SLM Printed Waveguide Dual-Mode Filters With Reduced Sensitivity to Fabrication Imperfections,” *IEEE Microwave and Wireless Components Letters*, vol. 31, no. 11, pp. 1195-1198, Nov. 2021.

[7] C. Guo, Y. Yu, S. Li, X. Wen, A. Zhang, Y. Wang, and M. Attallah, “Monolithic 3D Printed Waveguide Filters with Wide Spurious-free Stopbands using Dimpled Spherical Resonators”, *IET Microwaves, Antennas & Propagation*, vol. 15, no. 12, pp. 1657 – 1670, 2021.

[8] T. Skaik, D. Wang, P. Hunyor, H. Wang, P. G. Huggard, T. Starke, Q. Zhang, Y. Wang, "A 3D Printed V-Band Twisted Monolithic Waveguide Bandpass Filter," 2023 *53rd European Microwave Conference (EuMC)*, Berlin, Germany, 2023, pp. 231-234.

[9] W. Ameen, A. A.-Ahmari, and M. K. Mohammed. "Self-supporting overhang structures produced by additive manufacturing through electron beam melting." *The International Journal of Advanced Manufacturing Technology*, 104, no. 5 (2019): 2215-2232.

[10] T. Skaik, M. Salek, P. Hunyor, H. Wang , P. G. Huggard, P. F. Wilson, M. A. Williams, and Y. Wang, "Evaluation of 3-D Printed Monolithic G-Band Waveguide Components," *IEEE Transactions on Components, Packaging and Manufacturing Technology*, vol. 13, no. 2, pp. 240-248, Feb. 2023.

[11] L. Qian, Y. Wang, S. Li, A. E.-M. A. Mohamed, M. M. Attallah, T. Skaik, P. Booth, L. Pambaguian, C. M. España, and P. M.-Iglesias, "A Narrowband 3-D Printed Invar Spherical Dual-Mode Filter With High Thermal Stability for OMUXs." *IEEE Transactions on Microwave Theory and Techniques*,70, no. 4 (2022): 2165-2173.

[12] P. Vaitukaitis, K. Nai, J. Rao, M. S. Bakr and J. Hong, "Technological Investigation of Metal 3-D Printed Microwave Cavity Filters Based on Different Topologies and Materials," *IEEE Transactions on Components, Packaging and Manufacturing Technology*, vol. 12, no. 12, pp. 2027-2037, Dec. 2022.

[13] U. Ali, H. Fayazfar, F. Ahmed, and E. Toyserkani, "Internal surface roughness enhancement of parts made by laser powder-bed fusion additive manufacturing," *Vacuum*, vol. 177, Jul. 2020, Art. no. 109314.

[14] Y. Kaynak, O. Kitay, "The effect of post-processing operations on surface characteristics of 316L stainless steel produced by selective laser melting," *Additive Manufacturing*, vol. 26, pp. 84-93, 2019.

[15] Y. Yu, Y. Wang, T. Skaik, T. Starke, X. Shang, M. J. Lancaster, P. Hunyor, P. G. Huggard, H. Wang, M. Harris, M. Beardsley, and Q. S. Cheng, "D-Band Waveguide Diplexer Fabricated Using Micro Laser Sintering," *IEEE Transactions on Components, Packaging and Manufacturing Technology*, vol. 12, no. 9, pp. 1446-1457, Sept. 2022.

[16] T. Skaik, Y. Wang, M. Salek, P. Hunyor, H. Wang, P. G. Huggard, T. Starke, M. Attallah, and R. Martinez, "A 3-D Printed 300 GHz Waveguide Cavity Filter by Micro Laser Sintering," *IEEE Transactions on Terahertz Science and Technology*, vol. 12, no. 3, pp. 274-281, May 2022.

[17] R. J. Cameron, C. Kudsia and E. Mansour, "*Microwave filters for communication systems*," 2nd ed., Hoboken, USA: J. Wiley., 2018, pp. 323–335.

[18] A. Mostaani, L. Qian, R. Martinez, P. F. Wilson, M. Attallah, Y, Wang, M. A. Williams, "Investigation of a 3D-Printed Narrowband Filter with Non-Resonating Nodes," *2021 IEEE MTT-S International Microwave Filter Workshop (IMFW)*, 2021, pp. 316-318.

[19] X. Shang, W. Xia, and M. J. Lancaster, "The design of waveguide filters based on cross-coupled resonators," *Microwave and Optical Technology Letters*, vol. 56, no. 1, pp. 3–8, 2014.

[20] A. Mostaani, Y. Wang, L. Qian, A. E.-M. A. Mohamed, M. M. Attallah, and T. Skaik, "Compact Self-Supportive Filters Suitable for Additive Manufacturing," *IEEE Transactions on Components, Packaging and Manufacturing Technology*, vol. 13, no. 12, pp. 1966-1972, Dec. 2023.

[21] M. Salek, X. Shang, R. C. Roberts, M. J. Lancaster, F. Boettcher, D. Weber, and T. Starke, "W-Band Waveguide Bandpass Filters Fabricated by Micro Laser Sintering," *IEEE Transactions on Circuits and Systems II: Express Briefs*, vol. 66, no. 1, pp. 61-65, Jan. 2019.

[22] O. A. Peverini, G. Addamo, M. Lumia, G. Virone, F. Calignano, M. Lorusso, and D. Manfredi, "Additive manufacturing of Ku/K-band waveguide filters: A comparative analysis among selective-laser melting and stereo-lithography," *IET Microwaves, Antennas & Propagation*, vol. 11, no. 14, pp. 1936–1942, Nov. 2017.

[23] M. Almeshehe, N. Murad, M. Rahim, O. Ayop, N. Samsuri, M. A. Aziz, M. Osman, "Surface roughness impact on the performance of the 3D metal printed waveguide coupler at millimeterwave band," *Engineering Science and Technology, an International Journal*, vol. 35, 2022, Art. no. 101129.

[24] E. Beevers, D. Neumayer, B. Bonvoisin, A. Brandão, S. Hansal, M. Doppler, T. Rohr, B. V. Hooreweder, “Effect of Hirtisation treatment on surface quality and mechanical properties of AlSi10Mg samples produced by laser powder bed fusion,” *Materials Today Communications*, Vol. 38, 2024, pp. 108042.

[25] E. Hammerstad and O. Jensen, “Accurate Models for Microstrip Computer-Aided Design,” *1980 IEEE MTT-S International Microwave Symposium Digest*, Washington, DC, USA, 1980, pp. 407-409.

[26] X. Shang, P. Penchev, C. Guo, M. J. Lancaster, S. Dimov, Y. Dong, M. Favre, M. Billod, and E. d. Rijk, “W-band waveguide filters fabricated by laser micromachining and 3-D printing,” *IEEE Transactions on Microwave Theory and Techniques*, vol. 64, no. 8, pp. 2572–2580, Aug. 2016

[27] B. Zhang and H. Zirath, “3D printed iris bandpass filters for millimetre-wave applications,” *Electronics Letters*, vol. 51, no. 22, pp. 1791–1793, Oct. 2015.

[28] X. Liao, L. Wan, Y. Zhang, and Y. Yin, “W-band low-loss bandpass filter using rectangular resonant cavities,” *IET Microwaves, Antennas & Propagation*, vol. 8, no. 15, pp. 1440–1444, Sep. 2014.

[29] J. Xu, J.-Q. Ding, Y. Zhao, and J.-X. Ge, “W-band broadband waveguide filter based on H-plane offset coupling,” *Journal of Infrared, Millimetre, and Terahertz Waves*, vol. 40, no. 4, pp. 412–418, Apr. 2019.

CHAPTER 9

CONCLUSION AND FUTURE WORK

9.1 Conclusion

This thesis focused on proposing novel synthesis methods of filters and multiplexers, modified design techniques, and fabrication of microwave filters using different materials. **Chapter 2** describes different methods for synthesis a coupling matrix of Chebyshev filters. These include the synthesis using *g*-values, the (N+2) × (N+2) coupling matrix, the extracted pole, the unified extracted pole, and the non-resonating node synthesis method. The step-tuning design technique of filters is also briefly explained. In **Chapter 3** a new synthesis method is proposed for filters with multiple-dangling nodes, which generates more transmission zeros than the number of in-band poles (filter order number). The work shows the effect of out-of-band complex reflection zeros with non-zero real part, which is generated due to the multiple-dangling nodes. This deteriorates the out-of-band signal rejection. A mixed E/H-plane dangling-node structure is used to improve the rejection. A sample filter is designed, and the fabrication is enabled by 3D-printing technology. **Chapter 4** presents a new synthesis method for diplexers and multiplexers with all-resonator topology. The method generates a more accurate and robust initial coupling matrix for multiplexers by considering the loading effect of different channels. The method reduces the synthesis time of such topologies to seconds. **Chapter 5** presents a third-order X-band filter designed using the non-resonating node method and fabricated using selective laser melting technology. The X-Ray imaging of the filter shows the effect of shrinkage due to the fabrication process. Without any tuning, the filter S parameters show a promising result. However, a frequency deviation and resonator detuning are evident. **Chapter 6** investigates the pros and cons of using a titanium alloy Ti64 in fabrication of a fifth-order X-band filter. Taking advantage of Ti64 properties, the filter is designed with 1 mm wall thickness leading to a very light weight filter. In this chapter a modified rounded rectangular resonator is used to build the filter. The modified structure allows the filter to be printed without any tilted printing direction and no internal support. The coupling irises are moved to one side of the filter to ease the polishing and silver coating. A frequency shift and resonator detuning are visible on the measured S parameters. **Chapter 7** proposes an irregular-hexagonal cavity resonator for compactifying filter structure. The resonator offers high printability, flexible designs and allows the filters to be printed vertically without any tilt against the printer platform. The compact size and the vertical printing direction led to having more room for other components on the printer platform. However, the proposed resonator has a lower Q factor compared to a rectangular resonator. Three filters are designed using the irregular-hexagonal

resonator and fabricated using selective laser melting technology. Very good agreement is achieved for all three filters. **Chapter 8** presents an E-band filter designed using a modified hexagonal resonator to improve the printability and compactify the filter structure. Two samples of the filter are printed using micro laser sintering technology and then gold coated. The coating improves the insertion loss by ~1 dB. The second sample is electrochemically polished using Hirtisation process before gold coating. This polishing technique reduces the surface roughness to 1.95 μm without detrimentally eroding the internal coupling structures and significantly reduces insertion loss of the filter to a record low level of 0.14 dB. However, due to the amount of material removed during the polishing, the frequency deviation is bigger compared to the un-polished sample.

9.2 Future Work

Some possible future work based on what is presented in this thesis are given below.

i. *Improving the synthesis method of multiple-dangling node filters*

In the proposed method in **Chapter 3**, the out-of-band signal rejection is highly sensitive to the real part of the out-of-band reflection zeros leading to deterioration in the signal rejection level. A further study is worthwhile to reduce the sensitivity on the real-part of the out-of-band reflection zeros.

ii. *Improving the synthesis method of all-resonator multiplexers*

As mentioned in **Chapter 4**, the proposed method generates a robust initial coupling matrix that can reduce the matrix optimisation time to seconds. However, the iterative process of the method is not fully automated and has the capacity to be improved. Moreover, the method still requires a final quick optimisation. The theory behind the method can be further developed to remove the need for optimisation.

iii. *Developing a software for the synthesis of all-resonator multiplexers*

In **Chapter 4**, the proposed method is validated with several examples with different topologies and specifications. The method can be used as a semi-automated software tool to synthesise the all-resonator multiplexers.

iv. *Improving the proposed modified resonator geometries*

The modified resonators discussed in **Chapter 6**, **Chapter 7**, and **Chapter 8** have lower *Q* factor compared to a rectangular resonator. This can be improved by further structural modification without losing the printability offered by the proposed geometries.

v. *Tuning the E-band filter*

The measurement results of the E-band filter in **Chapter 8** shows a frequency deviation and resonator detuning comparted with the simulations. According to the simulations, it is possible to compensate the resonator detuning of the filter by adopting three 0.5 mm diameter tuning needles. However, tuning at such high frequencies is not straightforward. A systematic study on the tuning of such filters should be worthwhile.